USING ALKALI-ACTIVATED SLAG FERROCEMENT TO STRENGTHEN CORRODED REINFORCED CONCRETE COLUMNS

FANG SHUAI

PhD

The Hong Kong Polytechnic University

2018

The Hong Kong Polytechnic University

Department of Civil and Environmental Engineering

USING ALKALI-ACTIVATED SLAG FERROCEMENT TO STRENGTHEN CORRODED REINFORCED CONCRETE COLUMNS

FANG SHUAI

A thesis submitted in partial fulfillment of the requirements for the degree of Doctor of Philosophy

September 2017

CERTIFICATE OF ORIGINALITY

I hereby declare that this thesis is my own work and that, to the best of my knowledge and belief, it reproduces no material previously published or written, nor material that has been accepted for the award of any other degree or diploma, except where due acknowledgement has been made in the text.

___________________________________(Signed)

__________FANG Shuai______________(Name of student)

ABSTRACT

Chloride-induced corrosion of reinforcement has endangered the safety of reinforced concrete structures. Corrosion weakens cross-sectional area of reinforcements and bonding between concrete and reinforcements. It generates cracks in concrete cover, which accelerates invasion of chloride and causes further corrosion. Corrosion of reinforcement decreases loading capacity and ductility and shortens service life of structural members. It is, therefore, necessary to strengthen corroded reinforced concrete members to ensure structural safety and to extend service life.

It is the objective of this study to develop effective strengthening schemes for corroded concrete columns using alkali-activated slag (“AAS”) ferrocement. To optimize the mix proportion of AAS, complete factorial experiments and analysis of variance were implemented to investigate effect of alkali content and modulus of activator on flexural strength, compressive strength, drying shrinkage, setting time, and resistance to chloride penetration of AAS mortar. Accelerated corrosion test was conducted on steel bars embedded in AAS mortar to examine protection of AAS and corrosion inhibitors on reinforcements. Tensile strength of AAS ferrocement and its confinement on plain concrete columns were examined and modeled. Seventeen full-scale column specimens were prepared and fourteen of them suffered from artificial accelerated corrosion. Twelve corroded specimens were subsequently strengthened using proposed strengthening schemes. The specimens were tested under axial compression, small eccentricity and large eccentricity to assess effectiveness of strengthening schemes, respectively.

Experimental results have shown that rising alkali contents or moduli can increase compressive strength, drying shrinkage, and shorten setting time of AAS. With increasing moduli, there is a steady improvement in compressive strength but a reduction in flexural strength. $NaNO_2$ at 3% of slag mass can reduce the mass loss of reinforcements by 28% and exert nominal influence on the mechanical performance of AAS. An optimal AAS composition was achieved with Na_2O content of 3%, modulus of

0.9 and $NaNO_2$ dosage of 3%. Cracking load of AAS ferrocement is closely related to tensile strength of both mortar and stainless steel wire meshes ("SSWM"). With increasing layers of SSWM, peak load of confined square columns improves by 6% to 25%. Corroded columns suffer severe losses in loading capacity up to 46% as compared with control specimens. AAS ferrocement with two layers of SSWM is proved to be an effective strengthening scheme for columns with degree of corrosion of 8.9%. This scheme rehabilitates loading capacity of corroded specimens to a level comparable to or higher than that of control specimens. AAS ferrocement with four layers of SSWM demonstrates its efficiency in strengthening columns with degree of corrosion of 18.3%. It achieves enhancement of 63% and 94% in peak strength and ductility as compared with corroded specimen.

Analytical models are proposed to predict tensile strength of AAS ferrocement and loading capacity of specimens strengthened by ferrocement jackets. Prediction is in good agreement with experimental results.

LIST OF PUBLICATIONS

Fang, S., Lam, S.S.E., Wong, W.Y. (2015). “Repair corroded reinforced concrete columns using alkali-activated slag ferrocement.” *Proceedings of the 11th International Symposium on Ferrocement and 3rd ICTRC International Conference on Textile Reinforced Concrete*, Institute of Building Materials Research – RWTH Aachen University, Aachen, Germany, 7-10 June 2015, 531-538.

Fang, S., Lam, S.S.E., Wong, W.Y. (2017). “Using alkali-activated slag ferrocement to strengthen corroded reinforced concrete columns.” *Materials and Structures*, 50: 35-47.

Fang, S., Lam, S.S.E., Li, B., Yu, K., Chu, H.W. “Optimization of alkali activated slag mortar for strengthening corroded concrete structures.” *Under preparation*.

ACKNOWLEDGEMENTS

Doctoral study, especially writing this thesis is a long and arduous ways for me. I spent numerous days and nights in laboratories and library before I reach destination. When I complete this thesis, I feel unprecedentedly relaxed. The completion of this thesis cannot be achieved without support and assistance of many people.

First, I express my deep appreciation to my supervisor Dr. Eddie Siu-Shu Lam. Seven years ago, I came to Hong Kong to act as his research assistant, which broadened my horizon in field of research. Afterwards I pursued a Ph.D. study under his guide. The doctoral study has challenged me not only on research ability but also communication skills and endurance to achieve the best. I have devoted all my efforts to adapting myself to these challenges and resulting in fruitful outcome presented in this thesis. During this period, Dr. Lam gave me many suggestions on my research and consumed considerable time in revision of my thesis. I feel very thankful to his guidance.

I sincerely thank my wife and parents for their support and patience in my pursuit to the Ph.D. degree. They have accompanied me and kept full confidence in me during the whole study. Their encouragement has supported me through difficult times.

I feel so lucky to have friends who have fought together with me during these five years. I am deeply grateful to Ms. Wong Wing Ying for her essential assistance to my research. The structural experiments in this thesis cannot achieve success without her help. I would also like to acknowledge Dr. Zhan Baojian and Dr. Yu Kequan for their suggestions on development of AAS. I thank Dr. Yang Zhidong and Dr. Li Bo for their advices in writing thesis. In addition, technical support from technicians of Structural Engineering Research Laboratory and Concrete Technology Laboratory is appreciated.

TABLE OF CONTENTS

List of figures

List of tables

CHAPTER 1

INTRODUCTION

1.1 Background

Concrete has become the most popular building material due to excellent strength, low cost, and ease of moulding. It has broad prospects in industrial and civil engineering construction. Concrete production in China was summed up to 1.55 $\times 10^9$ m^3 in 2014 (China Cement Research Institute 2015). Concrete, however, is prone to crack under tension owing to relatively low tensile strength (Park and Paulay 1975). Reinforcements are introduced to improve the performance under tension. Reinforced concrete has been regarded to possess good durability and stable mechanical properties. With aging and lack of maintenance, reinforced concrete structures may prematurely reach the ends of their lives owing to chloride-induced corrosion of reinforcements. This phenomenon is especially severe for structures in coastal regions on account of a high content of chloride in air. As a result of corrosion by chloride salt, ore terminals of Beilun Port in the city of Ningbo, China, suffered from serious reinforcement corrosion in its superstructure only after ten years' service (Fan and Wu 1997). According to the inspection report conducted by Buildings Department of the Hong Kong SAR Government, about 26% of buildings in Hong Kong at age of 50 or above were found to exhibit different extents of defects which needed to be repaired (Buildings Department 2010). In addition, some coastal cities use sea water to cool down the industrial equipment and to flush toilets. Leakage of sea water from pipes may cause ingress of chloride ions into concrete and pitting corrosion of reinforcements (Figure 1.1).

Corrosion of reinforcement has led to serious structural problems, such as reduction of cross-section area of reinforcements and deteriorative bonding between concrete and reinforcements. Due to large increase in the volume of rust, tensile stress is introduced and results in cracks and spalling of concrete cover (Figure 1.2). It weakens the effective cross section of concrete, exposes reinforcements to aggressive environment and accelerates the corrosion further. Particularly, spalling of concrete can pose a threat to pedestrians. For instance, a pedestrian was injured by spalling concrete blocks falling off from a corroded bridge in New York (Broomfield 2007). Compared to strong wind and earthquake, corrosion of reinforcements tends to be neglected owing to its slow rate of deterioration. For post-tensioned prestressed structure, it is difficult to perceive the corrosion of prestressed tendons because they are enclosed in ducts. Corrosion will give rise to stress relaxation of steel tendons and impair loading capacity of structures (Woodward and Williams 1988). When corrosion exceeds the threshold level, failure may occur suddenly without extensive plastic deformation. This has resulted in numerous collapses of reinforced concrete elements, especially cantilevered balconies and canopies. In 2014, corrosion-induced fracture of reinforcements caused sudden collapse of a canopy in Shenzhen Luohu Talent Market, killed three and injured twelve passers-by (Figure 1.3). In Hong Kong, spalling of concrete and collapses of balconies and canopies have been reported and resulted in casualties in recent years (Apple Daily 2015, 2016, 2017). These accidents have drawn the attention of society to safety of corroded buildings.

Since corrosion of reinforcements reduces loading capacity and shortens the service life of reinforced concrete members, resource has been allocated on strengthening and reconstructing corroded structures. More than 20 billion US dollars were acquired to strengthen corroded highway structures in Unite States (Strategic High Research Program 1989). In China, corrosion brought an economic loss of 100 billion RMB yearly (Ke 2003). Hans (2010) pointed out that annual financial loss caused by corrosion reached 2.2 trillion US dollars, which was over 3% of the world's gross domestic product. It is necessary to develop effective and economic strengthening methods that can immune the reinforcement from corrosion (i.e. suppressing the activity of chloride ions) and extend service life of reinforced concrete structures.

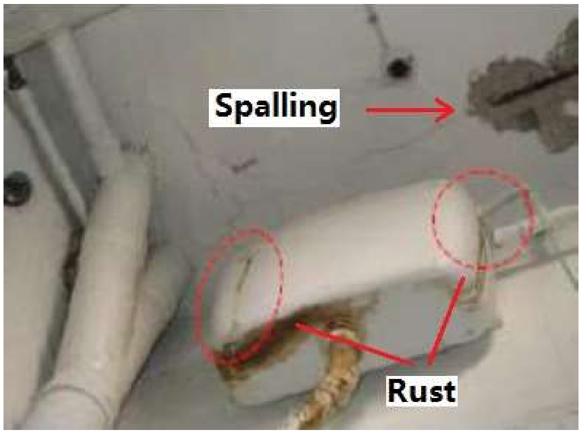

Figure 1.1 Corrosion of drainage pipe in a toilet (Wong 2014)

Figure 1.2 Spalling of concrete cover in a bridge pier (Riversong 2015)

Figure 1.3 Collapse of canopy in Shenzhen Luohu Talent Market (Liu 2014)

Traditional repair methods, simply replacing corroded reinforcements by new ones or strengthening corroded members using fibre reinforced polymer ("FRP"), cannot ensure long-term durability (Batis et al. 2003). New corrosion at the boundary of repaired area may appear shortly after the repair due to the presence of chloride ions inside concrete. Moreover, FRP performs poorly under fire because epoxy resin used to bond FRP softens rapidly at elevated temperature. Han et al. (2006) indicated that mechanical contribution of FRP jackets has to be ignored under fire because of rapid loss in strength at moderate temperature. Researchers and engineers are devoting various methods to prevent and alleviate the corrosion of reinforcements, such as epoxy coated reinforcement, electro-chemical desalting, and cathodic protection. It is worth noticing that the above mentioned repair techniques have encountered various difficulties in practice. Epoxy coating can be easily damaged during construction and result in further corrosion (Yeomans 1994). Electro-chemical desalting requires complex operation and may lead to hydrogen embrittlement of reinforcements. Some scholars have indicated that electro-chemical desalting can weaken the bond strength between concrete and reinforcement, and induce alkali aggregate reaction (Buenfeld and Broomfield 2000; Lu et al. 2002; Zhu et al. 2002). In addition, high cost of power supply and regular maintenance of cathodic protection system impedes its application.

As an alternative, this study proposes to use cementitious materials mixed with anti-corrosion agent to strengthen corroded concrete structures. This can be achieved by wrapping steel reinforcements using high performance ferrocement containing corrosion inhibitors. Corrosion inhibitors have the advantages of uniform distribution and not easy to leach out due to compactness of ferrocement, which ensures durability. Chloride inhibitor inside the ferrocement migrates and surrounds the reinforcements to keep them passivated. Compact micro-structure of ferrocement may restrain the permeation of chloride ions. In addition, ferrocement brings additional load carrying capacity due to its confinement effect on core concrete.

Compared to Ordinary Portland cement ("OPC"), AAS exhibits earlier and higher strength, denser structure and better durability in aggressive environment. When activated by liquid sodium silicate, AAS can achieve 28-day compressive strength at 80 MPa or above (Altan and Erdoğan 2012; Bilim and Ati 2012; Fernández-Jiménez et al. 1999). Moreover, AAS provides strong resistance to chemical attack and high temperature because of dense microstructure and low calcium silicon ratio in hydration products which ensures its chemical stability in corrosive media or at elevated temperatures (Shi and Qian 2000). Shi et al. (1992) immersed AAS in different corrosive solutions at 40℃ for 42 days and deleterious influence on the compressive strength of AAS was not observed. Roy et al. (2000) showed that AAS could reduce the diffusion rate of chloride at least by a factor of two. Research results have also indicated that fire resistance of AAS is better than that of cement paste (Zheng et al. 2009). Additionally, slag is regard as an environmental friendly material as the energy consumption of its production is only 10% to that of OPC (Shi and Qian 2000). Summarizing the above, good mechanical properties and excellent durability of AAS make it suitable as the base material of ferrocement for strengthening corroded structures.

1.2 Objectives and research significance

Although AAS possesses excellent structural performance, durability, and environmental benefit, its enormous potential as a repair material has not been developed. Little attempt has been made to extend its use to structural rehabilitating. This study, hence, aims to explore the feasibility of application of AAS ferrocement mixed with corrosion inhibitors in strengthening corroded concrete structures. To this end, the material behavior of AAS was studied and mix proportion of AAS was optimized using a full factorial experiment. Anti-corrosion performance of $NaNO_2$ and a commercial corrosion inhibitor was examined. Tensile properties of AAS ferrocement with different layers of SSWM were tested. Full-scale column specimens were prepared and subjected to axial compression, small and large eccentricity, respectively. Confinement of AAS ferrocement on reinforced concrete columns was analyzed.

This study reveals the effect of alkali content and modulus of activator on flexural strength, compressive strength, setting time, drying shrinkage and resistance to chloride penetration of AAS mortar. Different from other studies, a new repair system comprising AAS ferrocement and corrosion inhibitors is presented to strengthen corroded concrete columns. Efficiency of the proposed strengthening system is verified by an experimental program. Empirical equations to determine tensile strength of AAS ferrocement and loading capacity of columns strengthened by AAS ferrocement are provided.

1.3 Layout of the thesis

This thesis comprises eight chapters as shown in Figure 1.4:

Chapter 1 introduces the research background and states the purposes and significance of this study. Experimental methods and main research outcomes are described.

Chapter 2 reviews the research status in the field of chloride-induced corrosion, adverse effect of corrosion on reinforced concrete structures, strengthening method, and material properties of AAS ferrocement, and highlights limitations and gaps in earlier literature.

Chapter 3 evaluates the effect of alkali content and modulus of sodium silicate on flexural and compressive strength, initial and final setting time, chloride ion permeability and drying shrinkage of AAS.

Chapter 4 analyzes the significance of alkali content and modulus of sodium silicate and their interaction to the performance of AAS. Relationships between performance of AAS and significant factors are established. Based on a comprehensive assessment, the best mix proportion of AAS is optimized for strengthening corroded reinforced concrete structures. Effectiveness of AAS containing corrosion inhibitors on protection of reinforcements is evaluated.

Chapter 5 investigates the performance of fibers reinforced AAS and AAS ferrocement under flexural tests. AAS ferrocement with SSWM is optimized to confine concrete columns. Confinement action of AAS ferrocement on square plain concrete columns is experimentally evaluated. Direct tensile strength of AAS ferrocement is examined to quantitatively analyze the confinement action.

Chapter 6 explores the use of AAS ferrocement to strengthen corroded reinforced concrete columns with different degrees of corrosion. Effectiveness of proposed strengthening method is evaluated by axial compression tests on control, corroded and strengthened columns. A model is proposed to predict the loading capacity of columns strengthened by AAS ferrocement under axial compression.

Chapter 7 evaluates the performance of strengthened columns under small and large eccentricity, respectively. A model is proposed to predict the loading capacity of specimens strengthened by AAS ferrocement under eccentricity.

Chapter 8 concludes main achievements and gives recommendations for further research.

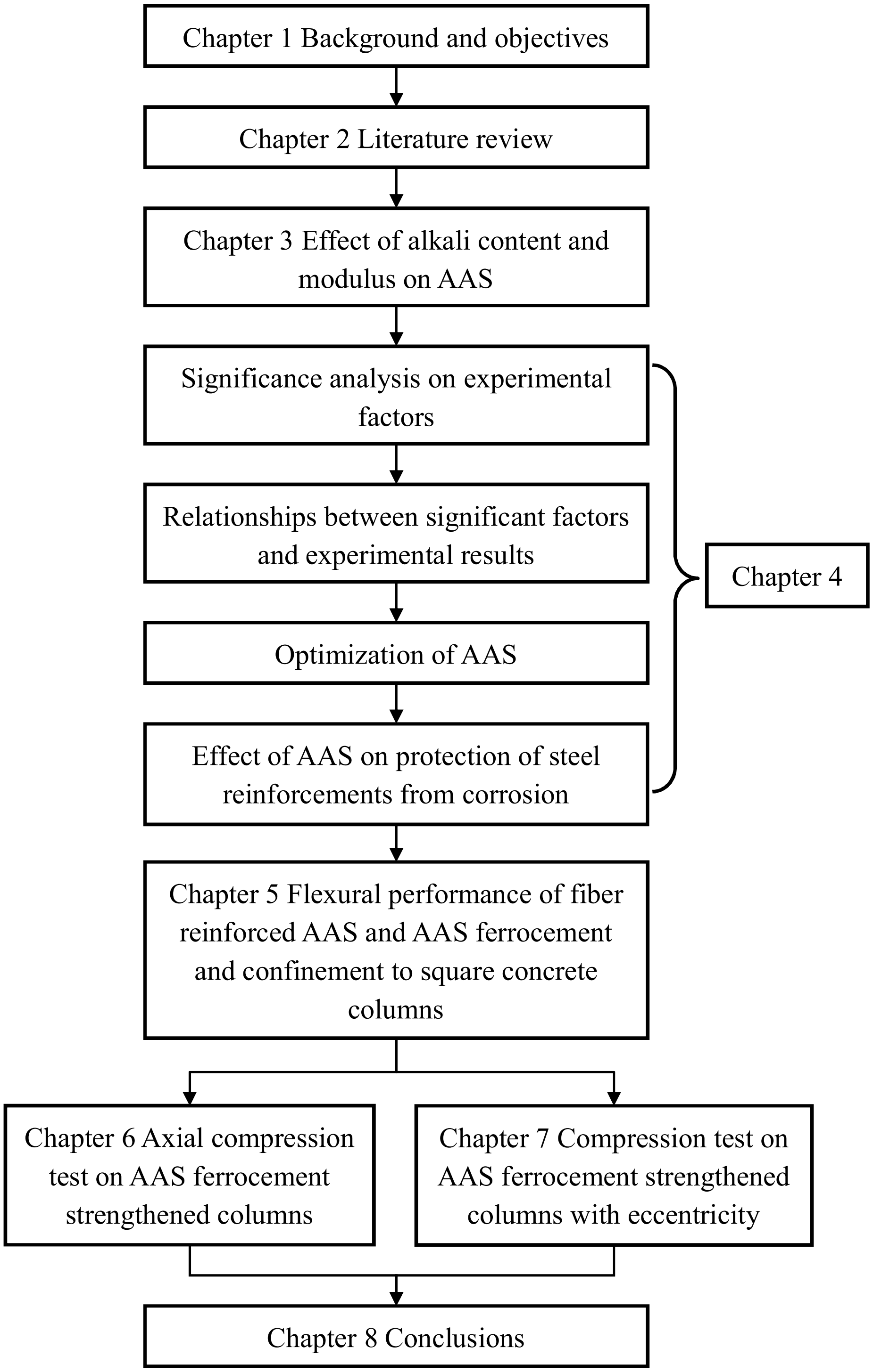

Figure 1.4 Organization of this thesis

CHAPTER 2

LITERATURE REVIEW

2.1 Introduction

Phenomenon of corrosion in concrete structures has been discovered since a century ago. As early as 1917, most marine constructions in Unite States were found to suffer from corrosion of reinforcements above waterline. This was ascribed to the chlorides accumulated in pore solution of concrete by capillarity, which has been widely agreed nowadays (Wig and Ferguson 1917). Corrosion of reinforcements has become a primary cause of degradation of concrete structures in corrosive environments (Roberge 1999). It threatens safety and durability of concrete structures and has resulted in severe economic losses and casualties. In recent years, abundant studies have been conducted to research electrochemical mechanisms and structural performance of corroded concrete structures and to explore various materials and techniques for strengthening the corroded structures. AAS, with advantages of excellent mechanical behavior and durability and low cost, has tremendous potential in the field of strengthening. In this chapter, a literature review is conducted on four aspects: a. mechanism of chloride-induced corrosion in reinforcements, b. adverse effect of corroded reinforcement on reinforced concrete structures, c. techniques for protecting reinforcements and strengthening corroded structures, and d. performance of AAS.

2.2 Mechanism of chloride-induced corrosion in reinforcements

2.2.1 Process of pitting corrosion in reinforcements

Naturally, high alkalinity (pH value > 12.5) of pore solution in concrete can promote the formation of a passivated film adherent on surface of reinforcement (Hansson 1984). This film, though extremely thin (less than 10 nm), can reduce the corrosion rate of steel to a negligible level (Montemor et al. 1998). The passive film has a double-layer structure in which the inner layer consists of ferroferric oxide while the outer one consists of gamma-hydrated ferric oxide (Castro et al. 1996). Passivation slowly proceeds until dense and nonporous oxide films are formed on iron matrix (Equations (2.1) - (2.3)).

$$FeOOH + H_2O = Fe(OH)_3 \tag{2.1}$$

$$2Fe(OH)_3 = Fe_2O_3 + 3H_2O \tag{2.2}$$

$$Fe(OH)_2 + Fe_2O_3 = Fe_3O_4 + H_2O \tag{2.3}$$

When reinforced concrete is exposed to chloride-contaminated environment, chloride ions migrate to the interface between iron matrix and passive films due to high diffusivity. Under the catalytic action of chloride ions, gamma-hydrated ferric oxides in passive films are converted to soluble ferric ions, which exposes underlying iron matrix to external environment. Local breakdown of the protective oxide films initiates pitting corrosion on reinforcements. It is different from acid-induced corrosion which homogeneously occurs on surface of reinforcements. Pitting corrosion is essentially an electrochemical process in which small pitting areas act as anodes in contact with the rest namely large passive surface as cathodes. Current flows through iron and arrives at cathodes, which accelerates consumption of anodes. Figure 2.1 shows pitting corrosion in chloride-contained solution where dissolution and hydrolyzation of iron occur at anode and deoxygenation occurs at cathode (Equations (2.4) - (2.6)). Under sufficient supply of oxygen, ferrous ions diffusing from bottom of acidic pit can be oxidized to ferric hydroxide and hydrated ferric oxide as corrosion products (Equations (2.7) - (2.8)). Corrosive cells exist not only between pitting corrosion and passivated iron, but actively corroded reinforcements and passivated ones which connect to each other. This phenomenon is very common in longitudinal reinforcements-stirrups systems in reinforced concrete. It was reported that stirrups corroded more seriously than main reinforcements due to relatively thin cover of stirrups. Corroded stirrups may suddenly fracture without yielding under tension when their degree of corrosion exceeds 10% (Zhang et al. 2006).

Anode: $$2Fe = 2Fe^{2+} + 4e^{-} \tag{2.4}$$

Cathode: $$O_2 + 2H_2O + 4e^{-} = 4OH^{-} \tag{2.5}$$

Total: $$2Fe + O_2 + 2H_2O = 2Fe(OH)_2 \tag{2.6}$$

$$2Fe(OH)_2 + O_2 = 2Fe(OH)_3 \tag{2.7}$$

$$2Fe(OH)_3 = Fe_2O_3 + 3H_2O \tag{2.8}$$

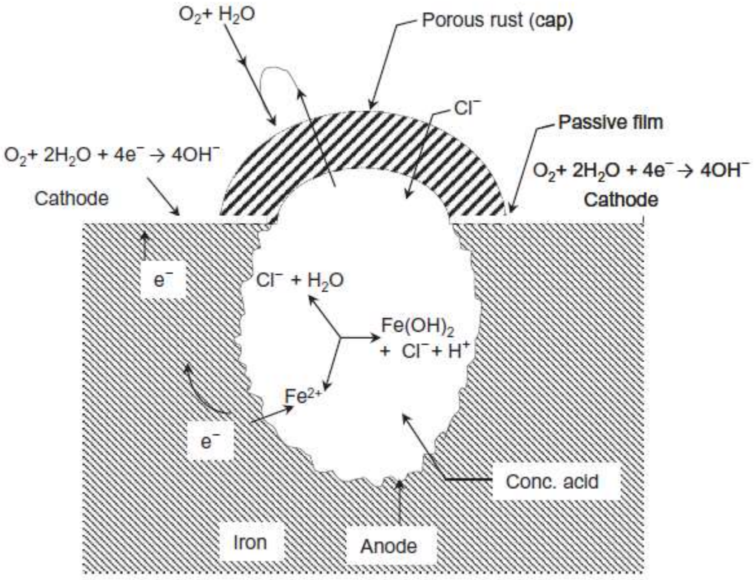

Figure 2.1 Schematic illustration of chloride-induced pitting corrosion (Popov 2015)

2.2.2 Chloride threshold for corrosion

Corrosion of reinforcements consists of two parts, an initiation stage and a propagation stage (Figure 2.2). In the initial stage, chloride ions penetrate into concrete and accumulate on surface of reinforcements but concentration of chloride ions is insufficient to arouse corrosion. When chloride content reaches a threshold value, corrosion is activated and enters the propagation stage. The critical chloride content is mostly presented as a mass fraction of binder or concrete. According to numerous experimental results, chloride threshold varies from 0.5 to 1.5% by mass of binder (Alonso et al. 2002; Locke and Siman 1980; Manera et al. 2008; Pettersson 1992; Sandberg 1998; Schiessl and Breit 1996; Thomas 1996). BS EN 206 (2013) restricts chloride content of reinforced concrete to 0.4% by mass of binder. The chloride threshold is also usually expressed as ratio of Cl^- to OH^-, which reflects inhibitive effect of alkalinity of concrete on corrosion of reinforcements (Alonso et al. 2000; Castellote et al. 2002; Li and Sagüés 2001). High concentration of hydroxide ions in pore solution contributes to stable passivated ferrous hydroxide on surface of reinforcements. This expression, however, neglects interfacial condition between reinforcements and concrete and effect of low-alkali mineral admixtures on binding chloride and densification of concrete (Glass and Buenfeld 1997b). According to Page and Havdahl (1985), Cl^-/OH^- cannot represent chloride threshold of concrete containing silica fume. Although replacement of cement by silica fume reduces alkalinity of concrete, denser microstructure resulted from secondary hydration of silica fume improves the resistance to invasion of chloride.

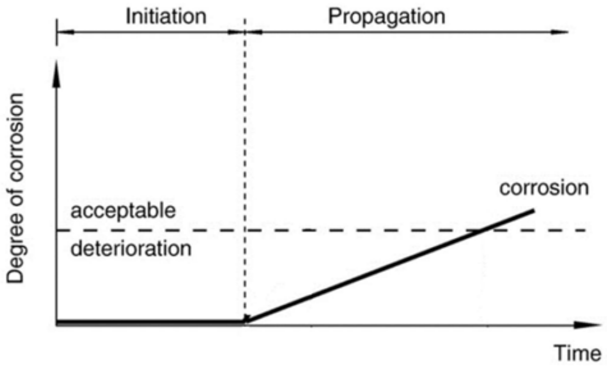

Figure 2.2 Two stages of corrosion in reinforcements (Tuutti 1982)

Critical chloride content in reinforced concrete depends on series of influencing parameters. Besides the above-mentioned alkalinity of concrete, interface between concrete and reinforcements, binder and admixture, thickness of concrete cover, moisture and oxygen content in concrete, and environmental temperature can also affect the chloride threshold.

Concrete-reinforcement interfacial characteristics are reported to dominate the initiation of corrosion (Glass and Buenfeld 1997a). A dense layer of calcium hydroxide exists between concrete and reinforcements. It acts as a physical barrier to chloride invasion as well as a chemical pH buffer to resist acidification. The closer lime-rich hydration product is to the interfacial zone, the more effectively it hinders chloride penetration

(Page et al. 1981). The precipitated calcium hydroxide neutralizes acid ions released by pitting corrosion and maintains pH value above 12.6 (Sykes and Balkwill 1988). Steel bars embedded in concrete showed a chloride threshold three times higher than bare ones when exposed to external chloride (Lambert et al. 1991; Page et al. 1991). In addition to hydration products of cement, initial defects in concrete, such as voids and cracks, will increase the susceptibility of reinforcements to corrosion (Mohammed and Hamada 2001).

Binder is another important factor affecting initiation of corrosion. Its hydration products bind free chlorides, change pH value, and improve density and electrical resistance of concrete. Taluminate and tetra calcium aluminoferrite in cement can react with chlorides and generate Friedel’s salt with long-term stability and dense structure. This chemical binding reduces chloride ions available for corrosion without any negative effect on strength of concrete (Justnes 1997). Moreover, chlorides can be further reduced by physical absorption of calcium silicate hydrate (“C-S-H”) gel. Another hydration product of cement, calcium hydroxide, increases alkalinity of concrete and passivates reinforcements. It is necessary to keep appropriate cement dosage in concrete from the perspective on anticorrosion. Hong Kong concrete code (2013) specifies the minimum cement content at 300 kg/m^3 for concrete exposed to chloride-rich environment.

Mineral admixtures, for instance fly ash, ground granulated blast furnace slag (GGBFS) and silica fume, have partially replaced cement to reduce hydration heat and enhance strength of concrete. The second hydration reaction between admixtures and C-S-H gel forms more gels and refines pores in concrete, which results in both more absorption to internal chlorides and stronger resistance to external penetration (Kayyali and Haque 1995). Similar to cement, fly ash and GGBFS contain abundant activated alumina conducive to form Friedel’s salt (Arya et al. 1990; Dhir and Jones 1999). The pozzolanic reaction, however, consumes calcium hydroxide and reduces pH value of pore solution, which is adverse to passivate reinforcements. Slightly lower chloride thresholds were observed in concrete with mineral admixtures (Kawamura et al. 1988;

Page and Vennesland 1983).

As shown in Equation (2.5), both water and oxygen content are indispensable elements for formation of OH^- and production of rust. Limitation of moisture in concrete and isolation of reinforcements from air are effective methods to inhibit corrosion. According to Böhni (2005), relative humidity ranging from 90 to 95% or drying-wetting cycles are favorite environments for corrosion. Corrosion relates to temperatures as well. Increasing temperatures from 20 to 70℃ diminish chloride threshold by five times. High temperature is deemed to increase corrosion rate by accelerating chloride permeation and corrosion reactions (Hussain et al. 1995). In addition, thick and compact concrete cover can extend diffusion path of chloride and hinder migration of chloride to surface of reinforcements.

2.2.3 Methods for corroding reinforcements

Reinforcements can be naturally corroded by exposure to marine or chloride-rich environments (Mietz and Isecke 1996). Some researchers took corroded reinforcements from aging concrete structures as test specimens (Palsson and Mirza 2002; Zhang et al. 1995). Natural corrosion method can reflect real characteristics of corroded specimens while consumes long time. It takes from several years to decades to obtain significant variation caused by corrosion in natural environments. In addition, removal of corroded reinforcements from existing deteriorated structures is not viable as this may affect structural integrity and safety. Artificially accelerated corrosion has been, hence, increasingly employed to achieve objective corrosion within a reasonable period. Artificial climate environment proves to be effective in accelerating corrosion by way of high temperature and humidity, repeated drying-wetting cycles with salt spray (Li 2001). Corrosion process and characteristics of reinforcements in artificial climate room were similar to that under natural condition (Yuan et al. 2007). This method, however, requires equipment for controlling temperature and humidity, and large environmental chambers to accommodate specimens. Compared to artificial climate environment, galvanostatic accelerated corrosion possesses advantages of flexibility and low cost and has been widely applied (Ahn and Reddy 2001; Almusallam et al. 1996; Lee et al. 2002). In the galvanostatic method, reinforcements act as anode and current is impressed to expedite oxidation reaction. Magnitude of current can be estimated by Faraday's law.

2.3 Adverse effect on structural properties

Once chloride content exceeds threshold value, corrosion of reinforcements will initiate. Corrosion will generate volumetric expansion of rusted reinforcements and introduce tensile stress in surrounding concrete, eventually causing cracking and spalling of concrete cover. Damage in concrete exposes reinforcements to corrosive environment, which destroys structural integrity and accelerates the corrosion. This section presents a review to summarize the detrimental effects of corrosion from following aspects: corrosion-induced cracks and spalling in concrete, bond between corroded reinforcements and concrete, mechanical properties of corroded reinforcements, performance of corroded concrete elements.

2.3.1 Corrosion-induced cracks and spalling in concrete

Liu and Weyers (1998) proposed a three-stage model for simulation of cracking induced by corrosion, namely filling, stressing and cracking. At the first stage, corrosion products fill interstices between reinforcements and concrete. This free expansion of rust does not exert any pressure to surrounding concrete. As corrosion reaction proceeds, reinforcement-concrete interface cannot accommodate growing corrosion products. Moreover, corrosion products have various degrees of expansion, up to six times than original iron (Figure 2.3). Such increase in quantity and volume of corrosion products in restricted space generates expansive stress in surrounding concrete. When the stress exceeds tensile strength of concrete, cracks appear in the reinforcement-concrete interface and develop towards surface of concrete. The cracks in concrete provide chloride and oxygen with a direct channel to surface of reinforcements, which aggravates the corrosion. Once the cracks propagate and connect each other, concrete cover may spall from substrate and expose the reinforcements to exterior environment

(Figure 2.4).

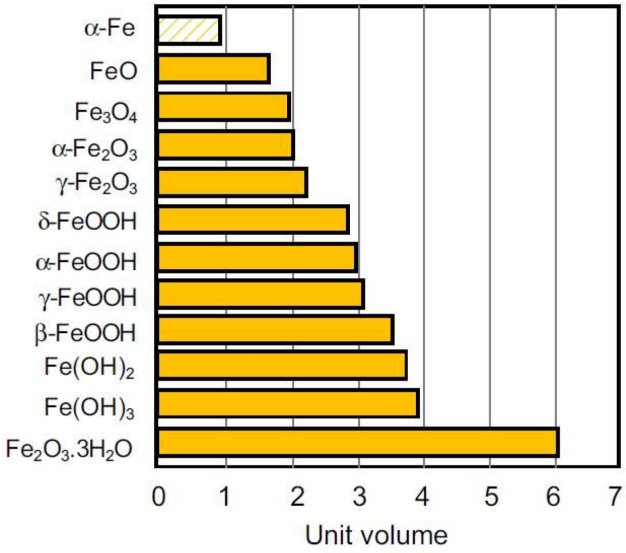

Figure 2.3 Volume of corrosion products (Lide 1999)

Figure 2.4 Cracks and spalling of concrete in a reinforced concrete beam

2.3.2 Bond between corroded reinforcements and concrete

Corrosion products at reinforcement-concrete interface can affect the bond between reinforcements and concrete. As degree of corrosion deepens, ribs of deformed reinforcements are damaged, which results in severe deterioration in mechanical interlocking with concrete. Al-Sulaimani et al. (1990) conducted pullout tests on reinforcements which was artificially pre-corroded by constant current. Bond strength of reinforcements first increases with degree of corrosion. Rust increases surface roughness of reinforcements and improves friction between reinforcements and concrete.

When degree of corrosion exceeds 1%, the bond strength continuously declines due to deterioration of bar ribs and reduction in section of reinforcements. Further, flaky corroded steel contributes to lubricate the reinforcements. Above factors facilitate slippage of corroded reinforcements from surrounding concrete. Fang et al. (2004) studied effect of degree of corrosion and confinement of stirrups on bond-slip behavior of both smooth and deformed bars. Test results showed deformed bars without confinement of stirrups suffer significant loss in bond strength with increasing degrees of corrosion. A corrosion-induced mass loss of 9% can decrease bond strength by 68%. Bond strength of deformed ones with confinement, by contrast, is insensitive to the corrosion level. The stirrups restrict cracking of concrete, impose hoop stress to longitudinal reinforcements and increase their interlocking with concrete, which diminishes adverse influence of corrosion on bond strength. As degree of corrosion aggravates, smooth bars without confinement experience a first rise and followed by a decline in bond strength, while smooth ones with confinement have slight improvement in bond strength. Corrosion induced roughness enhances the resistance of reinforcements to pullout in initial stage of corrosion. As increasingly severe corrosion of reinforcement, cracks appear and widen in concrete. Cracked concrete cannot provide effective confinement to embedded reinforcements. Stirrups can restrain cracking of concrete and thus benefit to bond smooth bars and concrete. Ratio of cover thickness to diameter of reinforcements has been attested to affect bond strength (Al-Sulaimani et al. 1990; Amleh 2000; Lin and Zhao 2016). The more the ratio is, the better confinement concrete cover can provide, and the higher bonding strength is.

2.3.3 Mechanical properties of corroded reinforcements

Corrosion results in sectional loss and mechanical degradation of reinforcements. Apostolopoulos and Papadakis (2008) accelerated corrosion of deformed bars by salt spray test. It was observed that pitting corrosion initiated at the bottom of ribs and developed to the zones between ribs. The ribs completely dissolved after 30 days of accelerated corrosion (Figure 2.5). Notches on reinforcements caused by chloride attack enlarged in both area and depth with growing corrosive duration. Reduction of mass and nominal diameter of reinforcements has a linear relationship with duration of exposure to salt spray. Du et al. (2005) and Wang et al. (2013) investigated influence of corrosion on cross-section shapes of reinforcements. They found shapes became irregular and residual diameters varied along length of reinforcements due to pitting corrosion. This uneven corrosion can decease yield load of reinforcements (Yuan et al. 2000). Corrosion diminishes nominal stress, i.e. ratio of load to original sectional area, while has little influence on true stress of reinforcements, i.e. ratio of load to actual sectional area (Apostolopoulos and Papadakis 2008). Almusallam (2001) had a similar view. He indicated that corrosion level does not affect tensile strength of reinforcements which is calculated according to actual area of cross section. Hui et al. (1997) studied mechanical loss of hot-rolled steel bars removed from corroded concrete structures. They found that corroded reinforcements with sectional loss less than 1% had almost same tensile strength and stress-strain relationships with non-corroded ones. Uniformly corroded reinforcements with sectional loss less than 5% still had obvious yield point. When the sectional loss exceeded 5%, stress concentration induced by corrosion began to exert negative influence on mechanical performance of reinforcements. Significant reduction was observed in both yield and ultimate strength. Compared to tensile strength, elongation of reinforcements is more sensitive to pitting corrosion (Ding and Cui 2000). Stress concentration results in premature yield of steel nearby the pitting and weakens ductility of reinforcements. Wang et al. (2011) and Zhang et al. (2006) found there was no obvious necking in the reinforcements with serious pitting corrosion. Almusallam (2001) accelerated corrosion of steel bars using galvanostatic method and tested their tensile performance. Corrosion considerably decreases elongation of reinforcement. Reinforcements with degrees of corrosion of 12.6%, 32% and 75% had reductions of 65%, 81% and 92% in elongation, respectively. Zhang et al. (2006) established relationships between nominal yiled strength, ultimate strength, ultimate strain and degree of corrosion of reinforcement removed from aging structures as follows,

$$f_{\mathrm{yc}}=\frac{\left(1\text{-}1.049\eta_{\mathrm{s}}\right)}{\left(1\text{-}\eta_{\mathrm{s}}\right)}f_{\mathrm{y0}} \tag{2.9}$$

$$f_{\mathrm{uc}}=\frac{\left(1\text{-}1.119\eta_{\mathrm{s}}\right)}{\left(1\text{-}\eta_{\mathrm{s}}\right)}f_{\mathrm{u0}} \tag{2.10}$$

$$\varepsilon_{\mathrm{uc}}=\mathrm{e}^{-2.501\eta_{\mathrm{s}}}\varepsilon_{\mathrm{u0}} \tag{2.11}$$

where f_{yc}, f_{uc} and $\varepsilon_{\mathrm{uc}}$ are nominal yield strength, ultimate strength and ultimate strain of corroded reinforcement, respectively. f_{y0}, f_{u0} and $\varepsilon_{\mathrm{u0}}$ are nominal yield strength, ultimate strength and ultimate strain of original reinforcement, respectively. η_{s} is the percentage of corrosion-induced mass loss.

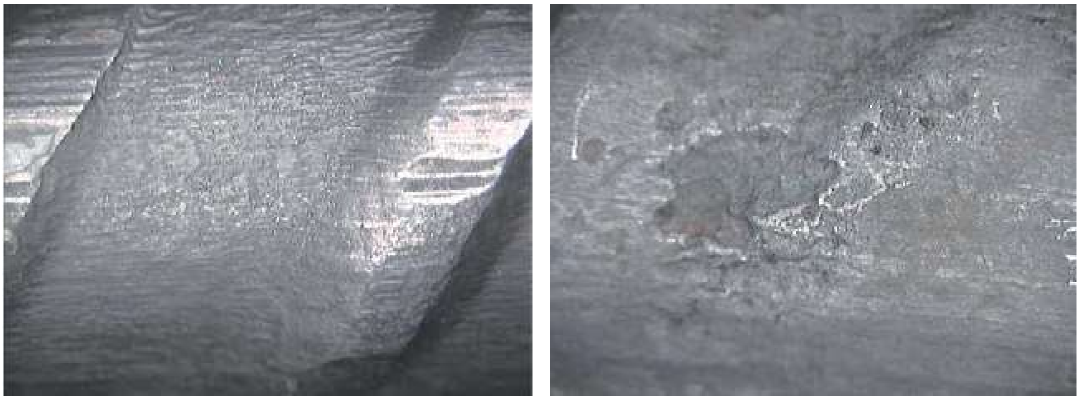

a. Ribs before corrosion

b. Corrosion initiating at bottom of ribs

c. Corrosion spreading to zones between ribs

d. Completely dissolved ribs

Figure 2.5 Corrosion process on surface of deformed bar (Apostolopoulos and Papadakis 2008)

2.3.4 Performance of corroded concrete elements

Corrosion of reinforcement can cause severe structural deterioration, such as spalling of concrete cover, cross-sectional loss of reinforcements and bond degradation between concrete and reinforcements. Abundant studies have been developed on performance of corroded concrete structures. Chung et al. (2008) conducted four-point flexural test on simply supported concrete slabs. Their test results showed slight corrosion can improve flexural capacity of slabs. When cross-section loss of reinforcements exceeded 2.89%, flexural capacity started to decline rapidly. Variation in loading capacity can be mainly ascribed to bond strength of corroded reinforcements. Zeng and Song (2011) tested flexural behavior of concrete beams with degrees of corrosion of reinforcement ranging from 6% to 15%. Both loading capacity and stiffness of corroded beams decreased with increasing degrees of corrosion. Plane cross-section assumption is not applicable to corroded beams due to bond deterioration between reinforcements and concrete. Zeng and Song (2011) proposed an equation to predict bending capacity of corroded beams as follow,

$$M_{\mathrm{uc}}=\left(1.0034\text{-}0.0159\eta_{\mathrm{s}}\right)M_{\mathrm{u0}} \qquad 6\%\leq\eta_{\mathrm{s}}\leq 12\% \tag{2.12}$$

where M_{uc} and M_{u0} are bending capacity of corroded and control beams, respectively. η_{s} is percentage of corrosion-induced mass loss.

Rodriguez et al. (1997) found corrosion increased deflection and crack width of concrete beams and changed their failure mode from flexural to shear failure. Pitting corrosion on stirrups vastly impaires shear capacity of concrete beams (Xu and Niu 2004). Hui et al. (1997a) compared failure causes of concrete members under flexural or compressive load. They pointed out that the former arises from bond deterioration and section loss of reinforcements, while the latter is related to section loss of both reinforcements and concrete. This conclusion has been verified by many studies (Shi et al. 1999; Tapan and Aboutaha 2011; Wang and Liang 2008). Li et al. (2012) indicated corroded columns have similar failure process but less ductility than control ones under axial compression because corroded stirrups cannot provide effective confinement to core concrete.

Additionally, seismic behavior of corroded concrete structures causes widespread concern. Ma et al. (2012) studied seismic performance of circular corroded columns under varying axial load ratios from 0.15 to 0.4. Both high axial load and level of corrosion reduce stiffness, energy dissipation capacity and ultimate displacement of column specimens. Horizontal loading capacity rises with axial load ratio. Shi et al. (2000) observed serious corrosion and fracture in stirrups of columns. Without confinement of stirrups, corroded columns suffered obvious loss in loading capacity, stiffness and ductility under repeated horizontal load. Dai and Yuan (2005) pointed out hysteretic loop of corroded specimens presents as S shape rather than plump shuttle one, which is attributed to slippage of reinforcements from concrete due to corrosion induced bond deterioration.

2.4 Techniques for protecting reinforcements and strengthening corroded concrete structures

2.4.1 Prevention of corrosion

Corrosion of reinforcement has led to degeneration in loading capacity and durability of concrete members, which threatens structural safety and results in severe economic loss. In recent years, various anti-corrosion methods have been developed to prevent corrosion of reinforcement. Concrete cover acts as physical barriers to insulate reinforcements from exterior aggressive environment. Dense and thick cover contributes to maintain alkalinity of interior concrete and restrain penetration of chlorides. Increasing thickness of concrete cover is regarded as an economical and easy-operational method to reduce risk of corrosion (Böhni 2005). Rasheeduzzafar et al. (1985) observed severe corrosion and spalled cover in reinforced concrete slabs with cover thickness of 0.5 inch after 20 years' service. The corrosion, however, was not significant in slabs with one inch of cover under the same service life. In addition, diffusion coefficient of oxygen and permeability were reported to decline with water cement ratio of concrete (Goto and Roy 1981; Jaegermann 1990; Kobayashi and Shuttoh 1991). Concrete with low water cement ratio and thick cover is beneficial to extend diffusion path of chloride and postpone corrosion of reinforcements. The effect of water cement ratio and cover thickness on corrosion of reinforcements is also specified in many technical guides. Hong Kong code of practice for structural use of concrete (2013) advises concrete structures near a coast should have nominal cover not less than 45 mm and water cement ratio not more than 0.55. Too thick cover, whereas, will reduce force arm of reinforcements thereby weakening bending capacity of elements. In addition, thick concrete cover increases crack width of reinforced concrete members under bending, which impairs effect of the cover (Lan et al. 1991).

Epoxy coating is an effective technique for protection of reinforcements developed in the 1970s (Manning 1996). The waterproof coating plays its protective role by insulating reinforcements from corrosive agents penetrating concrete cover. It is generally regarded as a reliable barrier to chloride under the precondition of structural integrity. Nevertheless, any damage during transportation and fixing, and cracking of the coating at bends of reinforcements may exposed bare steel to aggressive environment (Erdoğdu et al. 2001). Pitting corrosion will cause defects of coating owing to macro cell effect. Large area ratio of coated reinforcement (as cathode) to the defects (as anode) leads to rapid corrosion. Moreover, twice price of uncoated bars and weak bond with concrete restrict the application of epoxy coated bars (Bertolini et al. 2004).

Risk of corrosion can also be lowered by application of corrosion inhibitors. Corrosion inhibitors can work not only as admixture in fresh concrete but surface-applied agents for existing structures. The inhibitors function by increasing polarization and passivation of anode (for anodic inhibitor), or increasing hydrogen overvoltage and formation of precipitate on cathode (for cathodic inhibitor) (Trabanelli 1987). Since 1970s, nitrite has been extensively used in concrete structures (Hong 2005). It acts as a passivator by oxidizing ferrous ions formed in Equation (2.4) to ferric ions as follows.

$$2Fe^{2+} + 2OH^{-} + 2NO_2^{-} = 2NO + Fe_2O_3 + H_2O \tag{2.13}$$

This process produces an insoluble and stable oxide film on reinforcements. Nitrite prevents reinforcements from corrosion and simultaneously improves the compressive strength of concrete. Collins et al. (1993) evaluated seven different inhibitors in respect of corrosion, compressive strength and resistivity. Calcium nitrite performed best in mitigating corrosion and borate compounds were found to retard the setting of cement. Nitrate, however, may accelerate pitting corrosion when its dosage is insufficient (Lashiari 1996). Moreover, it is harmful to health and thus not allowed to be used in structures immersed in water in consideration of environmental protection and health. In recent years, environmentally friendly corrosion inhibitors have been rapidly developed. They are non-toxic and provide both cathodic and anodic protection (Bertolini et al. 2004).

In addition, electrochemical techniques, for instance, cathodic protection and electrochemical chloride removal have been extensively studied but rarely applied in building structures. High cost and potential adverse impacts such as concrete degradation, bond loss and hydrogen embrittlement of reinforcements hinder their popularization (Miranda et al. 2007; Pedeferri 1996).

2.4.2 Strengthening corroded concrete structures

For existing structures, corrosion-induced damage has threatened their safety and durability. Strengthening work, therefore, is necessary to rehabilitate loading capacity and extend service life of structures. Over the years, diversified strengthening techniques and materials, such as concrete jacketing (Li et al. 2009), patching (Sahamitmongkol et al. 2008), steel jacketing (Peng et al. 2015), FRP wrapping (Kashi et al. 2017; Tastani and Pantazopoulou 2004) and ferrocement (Jayasree et al. 2016; Mourad and Shannag 2012), have been proposed for the rehabilitation.

Concrete jacketing is an effective strengthening method at low cost. It increases cross-sectional area and provides extra loading capacity for concrete elements. Jackets can be prepared by casting concrete or shotcrete. This technique is applicable to various cross sections (Figure 2.6). It has been used to strengthen corroded concrete columns and improve loading capacity and hysteretic characteristics (Li et al. 2009; Liu 2009).

However, this method reduces usable area of buildings and time-consuming to construction.

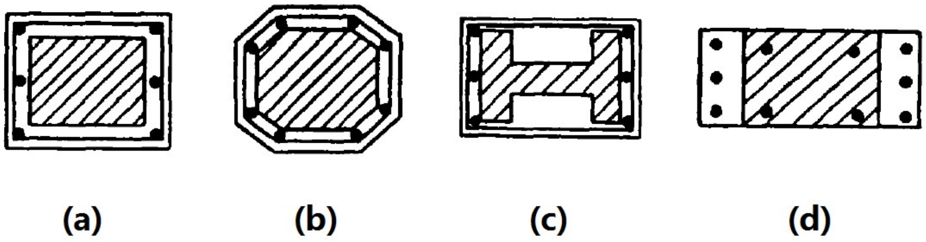

Figure 2.6 Various concrete jackets

Different from concrete jacketing, patch repairing retains original dimensions of repaired members. It includes removing corrosion-damaged concrete cover, cleaning corroded reinforcements and rehabilitation of concrete cover (Figure 2.7). Al-Dulaijan et al. (2002) studied effect of rebar cleanliness on durability of repaired concrete beams. It was indicated that rust existing on steel bars will cause further corrosion after repair. Cleaning corroded bars using sand blasting contributes to formation of stable passive film on the bars. For severely corroded structures, it is nessary to insert new bars to maintain loading capacity.

Figure 2.7 Patch repairing (Mainline Waterproofing Ltd 2017)

Epoxy and polymer modified mortar are recommended to rehabilite cover due to their high tensile strength, outstanding bond with concrete substrate and low permeability.

Sahamitmongkol et al. (2008) repaired corrode concrete beams by polymer modified mortar and epoxy-based material. Both repair materials can rehabilite bending capacity of beams comparable to or above that of control one. High ductility and bond strength of epoxy prevented interfacial failure and cracking of patching area. Kobayashi and Rokugo (2013) developed a new patching material consisting of cementitious material, polyvinyl alcohol fibers and polyethylene fibers. This fiber reinforced patching layer can prevent reinforcements from corrosion under salt spraying for 60 days and increase bending capacity of corroded beams by 33%. Nevertheless, local patch repair may cause corrosion in unrepaired area. It was reported that patch repair activated corrosion close to repaired area because of transfer of anodes on chloride contaminated members (Bertolini et al. 2004).

Steel jackets and steel plates have the advantages of high strength, thin thickness, easy and rapid installation, and thus are extensively used (Figure 2.8). Peng et al. (2015) and Li et al. (2013) strengthened corroded concrete beams by bolting and bonding steel plates with thickness of 3 to 5 mm, respectively. The strengthening effectively improved loading capacity and ductility, and reduced mid-span deflection of beams. Steel jackets have been used to strengthen beam-column joints of a derrick and consumed less time than concrete jackets (Zhang and Chen 2007). This strengthening method, however, does not consider durability of steel jackets in chloride-contaminated concrete structures.

Figure 2.8 Specimens strengthened by steel jackets (Belal et al. 2015)

Figure 2.9 Corroded grain silos strengthened by CFRP (QuakeWrap 2016)

FRP has recently become a favorite strengthening material due to its durability better than steel in corrosive environment. FRP is waterproof and chemically inert to chloride aggression, which guarantees durability of strengthened structures (Kashi et al. 2017). Bond strength of corroded reinforcements can be improved by confinement of FRP to columns (Deng et al. 2010). FRP strengthening is generally achieved by wrapping column or bonded on tensile region of beams and slabs (Figure 2.9). It can significantly enhance loading capacity and seismic performance of corroded elements (Chen et al. 2013; Tastani and Pantazopoulou 2004; Triantafyllou et al. 2017). Zhang et al. (2010), Haddad (2016) and Al-Saidy et al. (2010) strengthened corroded simply supported beams by bonding CFRP sheets on bottom of beams. Bending capacity and stiffness of beams increased with increasing layers of CFRP. Excessive CFRP will change failure mode of beams from tensile failure of CFRP to crushing of concrete. FRP can also increase compressive strength and ductility of corroded columns by transverse confinement, while without change in axial stiffness (Joshi et al. 2015). A classical model of compressive strength of concrete confined by FRP jackets is proposed as follows.

$$f_{\mathrm{cc}} = f_{\mathrm{c}}^{'} + \lambda \sigma_{\mathrm{lat}} \tag{2.14}$$

where f_{cc} and $f_{\mathrm{c}}^{'}$ are compressive strength of confined and unconfined concrete, respectively. λ ranges from 2.0 to 3.0 in various literatures (Lam and Teng 2002; Miyauchi et al. 1999; Tastani and Pantazopoulou 2004). σ_{lat} is the lateral pressure to concrete, which is given by Tastani and Pantazopoulou (2004) as follows.

$$\sigma_{\mathrm{lat}}=\frac{1}{2}\left(k_{\mathrm{f}}\cdot\rho_{\mathrm{fv}}\cdot E_{\mathrm{f}}\varepsilon_{\mathrm{f}}+k_{\mathrm{st}}\cdot\rho_{\mathrm{sv}}\cdot f_{\mathrm{yst}}\right) \tag{2.15}$$

where k_{f} and k_{st} represent proportion of region confined by FRP and stirrups in gross cross-section, respectively (Figure 2.10). k_{f} and k_{st} can be obtained by Equations (2.16) and (2.17). $w_{\mathrm{i}}^{'}$ and $s^{'}$ are clear distance between adjacent main reinforcements and stirrups, respectively. ρ_{fv} and ρ_{sv} are volumetric fraction of FRP and stirrups, respectively. E_{f} and ε_{f} are elastic modulus and strain of FRP jackets, respectively. f_{yst} is yield strength of stirrups. ρ_{cc} is area ratio of main reinforcements to core section.

$$k_{\mathrm{f}}=1-\frac{b_{\mathrm{s}}^{2}+d_{\mathrm{s}}^{2}}{3bd} \tag{2.16}$$

$$k_{\mathrm{st}}=\frac{\left(1-\sum_{\mathrm{i}=1}^{\mathrm{n}}\frac{w_{\mathrm{i}}^{'2}}{6b_{\mathrm{s}}d_{\mathrm{s}}}\right)\left(1-\frac{s^{'}}{2b_{\mathrm{s}}}\right)\left(1-\frac{s^{'}}{2d_{\mathrm{s}}}\right)}{\left(1-\rho_{\mathrm{cc}}\right)} \tag{2.17}$$

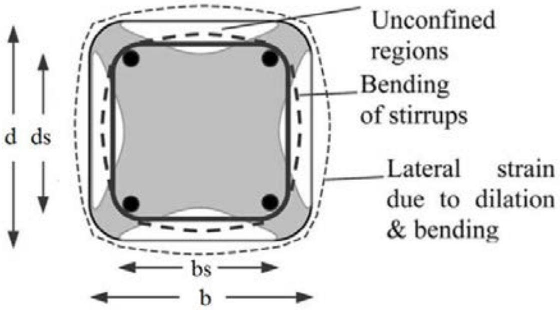

Figure 2.10 Effectively confined region

Tastani and Pantazopoulou (2004) indicated passive confinement of FRP increased with lateral dilation of concrete core. Failure began from the parts with lower corrosion and extended to the whole specimen. Abrupt fracture of FRP jackets and crushed concrete core were observed. Benefited from confinement of FRP jackets, the corroded columns had significant increase in both axial deformation and strength. Chen et al. (2011) tested corroded concrete columns confined by CFRP under axial compression, small and large eccentricity, respectively. FRP strengthening resulted in enhancement ranging from 24% to 67% in loading capacity of columns with degree of corrosion at 30%. However, FRP rapidly loses its strength at moderate temperature because resin matrix is transformed into viscous flow state at temperatures from 60 to 80 ℃ (ACI 440.2R-02). Mechanical contribution of FRP jackets is ignored when FRP-confined columns are subjected to fire (Han et al. 2006). Poor fire resistance of FRP limits its application in buildings.

As an alternative, ferrocement exhibits great potentiality in strengthening structures and it is resistant to fire and corrosion. Ferrocement is a thin cementitious composite reinforced by layers of meshes with small diameter (Figure 2.11) (ACI 549R-97). Meshes in cement contribute to crack control and improve tensile strength and ductility. Tensile strength of ferrocement is generally related to specific surface of reinforcements and angle between mesh orientation and loading direction (Abdullah and Mansur 2001). Compressive strength of ferrocement is proportional to cross-sectional area and water-cement ratio of cement matrix (Naaman 2000). Benefited by protection of cement cover, ferrocement performs well in fire. According to Williamson and Fisher (1983), ferrocement walls had fire resistance comparable to concrete ones. Kaushik et al. (1996) found ferrocement encased columns had higher residual strength than control ones after fire. Ferrocement has been widely used in the construction of boats, silos, tanks and prefabricated housing units owing to low cost and excellent compressive and tensile performance. Recently, use of ferrocement has been extended to the field of strengthening structures (Figure 2.12). Mourad and Shaannag (2012) strengthened eight preloaded concrete columns by ferrocement jackets with two layers of welded wire meshes. The strengthening improved axial loading capacity and stiffness of columns by 33% and 26%, respectively. Jayasree et al. (2016) investigated the effect of ferrocement jackets on flexural behaviour of corroded concrete beams. Experimental results showed ferrocement with mesh fraction of 1.2% by volume can increase bending capacity by 39% in beams with degree of corrosion of 10%. The strengthened beams even achieved higher ultimate load and stiffness than uncorroded ones. Kondraivendhan and Pradhan (2009) investigated the confinement of ferrocement on cylindrical concrete specimens. Specimens failed due to yielding of transverse wires in ferrocement and compressive failure of core concrete. Ferrocement efficiently enhanced compressive strength, axial and radial strain of concrete specimens. The lower compressive strength of concrete core was, the higher enhancement the ferrocement resulted in. Walliuidin and Rafeeqi (1994) proposed a model to predict compressive strength of cylindrical specimen confined by ferrocement as follows.

$$f_{cc} = f_c + k_m k_g k_p f_y \tag{2.18}$$

where f_{cc} and f_c are compressive strengths of confined and unconfined concrete, respectively. k_m is the coefficient concerning method of strengthening, which equals to 0.83, 0.88 and 1.00 for precast ferrocement shell, wrapped wire mesh layers, and integrally cast ferrocement with concrete core, respectively. k_g is the coefficient concerning grade of concrete. k_p is the coefficient concerning layers of wire meshes. f_y is yield strength of wire mesh.

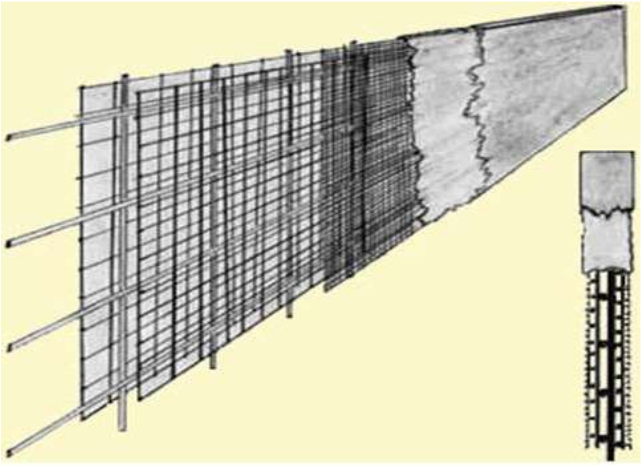

Figure 2.11 Cross section of ferrocement (The Constructor 2017)

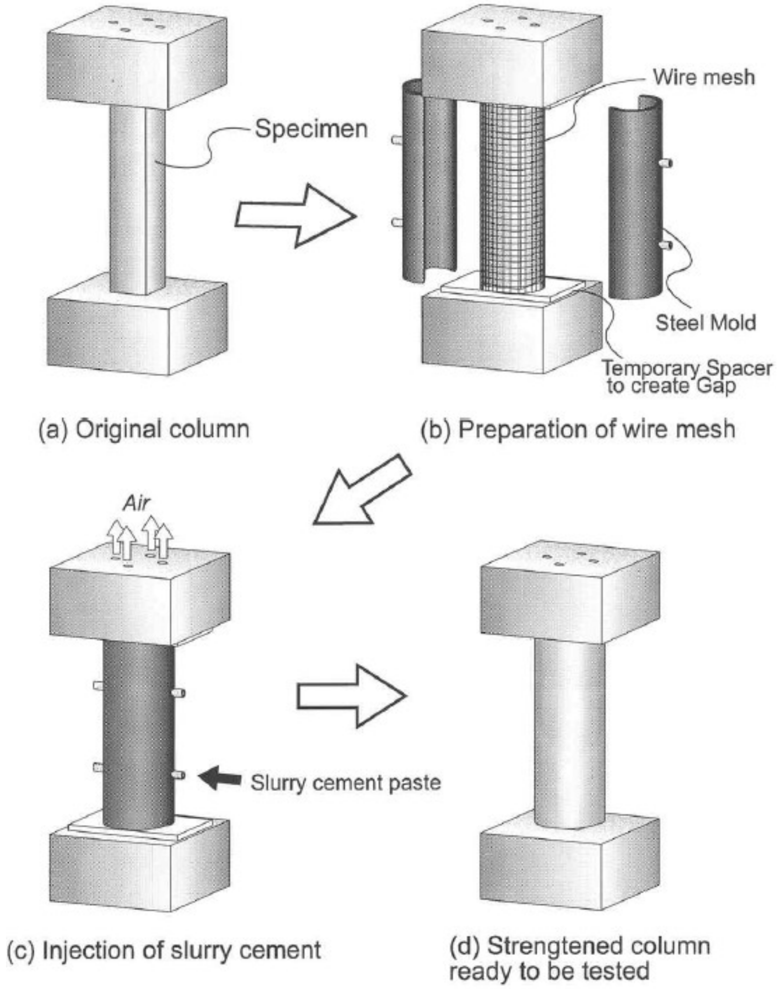

Figure 2.12 Strengthening columns using ferrocement jackets (Takiguchi and Abdullah 2001)

Traditional strengthening techniques only promote mechanical performance of corroded members. Chlorides remaining inside concrete substrate may cause new corrosion. Bencardino and Condello (2016) proposed an inhibiting-repairing-strengthening technique to retrofit corroded concrete members. It was achieved by installation of stainless steel fabric on concrete core and recovery of concrete cover by geoploymeric matrix. This new rehabilitation technique was demonstrated to be more effective and durable than current externally-bonded one. Li et al. (2004) developed styrene butadiene rubber modified concrete mixed with corrosion inhibitor to strengthen calcium chloride-contaminated concrete columns. The composite concrete succeeded in preventing migration of chloride to wrapped reinforcements. The above innovative strengthening methods satisfy requirement of both mechanical performance and resistance to corrosion. This criterion will be considered in the development of strengthening material in this study.

2.5 Performance of AAS

Portland cement has been widely used in civil engineering since it was invented in the 1820s. However, it consumes much fossil fuel and exhausts a large amount of greenhouse gas to atmosphere during manufacture. This is because calcination of raw cement materials in kilns involves large energy consumption and becomes main source of carbon dioxide (Equation (2.19)). One ton of carbon dioxide is emitted for each ton of cement produced (Roy 1999).

$$5CaCO_3+2SiO_2 \rightarrow 3CaO\cdot SiO_2+2CaO\cdot SiO_2+5CO_2 \qquad (2.19)$$

In contrast, blast furnace slag is environmentally friendly material with lower energy consumption. It is derived from industrial waste of iron production and has large reserve. Output of granulated slag in China reached 200 million tons in 2016 (CCPA 2017). Moreover, blast furnace slag has high hydraulic activity and can develop strength comparable to cement in alkaline environment. These advantages make it possible to replace Portland cement by AAS in strengthening corroded concrete buildings. Properties of this alkali activated material are introduced in this section.

2.5.1 Ground granulated blast furnace slag

Ground granulated blast furnace slag ("GGBFS") is by-product of iron manufacture. In production process of iron, iron ore, limestone and coke are charged into a blast furnace. Under the action of carbon monoxide, hematite and magnetite in iron ore are reduced to pure iron. Limestone, meanwhile, reacts with other component of iron ore, such as silicon dioxide, aluminium oxide, and magnesium oxide, and forms blast furnace slag (Shi et al. 2006). During fast cooling of molten blast furnace slag, quantities of amorphous glassy $CaO\text{-}Al_2O_3\text{-}SiO_2\text{-}MgO$ compounds form and give slag potential activity. Activity of GGBFS mainly depends on its chemical composition, content of glass and fineness. CaO is primary active oxide which can form hydraulic products including C-S-H gel, $2CaO\cdot Al_2O_3\cdot SiO_2$ and $2CaO\cdot SiO_2$. Al_2O_3 is another important component. It is necessary oxide for generating zeolites in alkaline environment. MgO exists in form of stable compound and does not affect volume stability of GGBFS. Moreover, MgO can decrease polymerization degree of $(SiO_4)^{4-}$ and $(AlO_4)^{5-}$ and facilitate vitrification of slag. Besides above three oxide, glass content is another key factor to determine hydraulic properties of GGBFS. This is because the polymerization degree of $(SiO_4)^{4-}$ and $(AlO_4)^{5-}$ in glassy phase is less than that in crystal phase, which means GGBFS containing glass content can easily break up and react with alkali solution (Pu 2010). In addition, fine GGBFS has large surface area and sufficient hydraulic reaction. Wang et al. (1994) suggested GGBFS with fineness ranging from 400 to 550 m^2/kg is suitable for production of AAS. Further improvement on fineness has little effect on strength of AAS while too fine GGBFS may lead to rapid setting of AAS.

2.5.2 Hydration of AAS

Hydraulicity of GGBFS can be motivated by alkaline activators. Various activators, such as silicate, hydroxide, carbonate and sulfate, were tried (Fernández-Jiménez et al. 1999; Shi 1996; Wang et al. 1994; Živica 2007). Wang et al. (1994) pointed out anions of alkaline activators play more important role than cations. They compared effect of NaOH, Na_2CO_3, Na_2SO_4 and Na_2SiO_3 on strength development of AAS mortar. Na_2SiO_3 activated GGBFS can achieve 1-day and 28-day compressive strength of 34.8 and 98 MPa, respectively. By contrast, GGBFS activated by other three activators developed slowly in both early and 28-day compressive strength. SiO_3^{2-} contributes to form silica gel which can react with Ca^{2+} and form calcium silicate hydrates. This increases strength of AAS and consumes $Ca(OH)_2$ vulnerable to corrosive environment. Shi (1996) studied pore structure of AAS mortar. He found GGBFS activated by Na_2SiO_3 has much lower porosity than that activated by NaOH or Na_2CO_3. Dense micro-structure guarantees good strength and durability of Na_2SiO_3 activated GGBFS.

Hydration of GGBFS in alkaline solution includes disintegration of GGBFS particles and polycondensation of hydration products. Pu (2010) divided hydration of AAS into six stages. In the first stage, covalent bonds and ionic bonds of GGBFS fracture under action of hydroxide ions. GGBFS particles are decomposed into various ions, such as Ca^{2+}, $Ca(OH)^{+}$, $Ca(OH)(H_2O)^{+}$, SiO_4^{4-} and AlO_4^{5-}. This stage is an endothermic process. When concentration of cations and anions becomes saturated, intermediate complexes form in solution. Hydroxide ions are consumed accompanied by formation of highly amorphous monomers. This stage shows up as the first exothermic peak in hydration heat curves. The third stage is an inductive stage, in which accumulation of disintegrated GGBFS on surface of unreacted particles hinders their reaction with alkali. The disintegrated slag acts as a semipermeable membrane. It allows ingress of all ions while intercepts egress of silicate, which leads to rising osmotic pressure inside membrane. When the osmotic pressure exceeds strength of the membrane, hydration shell spalls and exposes interior GGBFS to alkaline solution, which speeds up reaction of GGBFS. Hydration of AAS shifts into an acceleration stage. The second exothermic peak appears in hydration heat curves. Increasing amorphous monomers in solution facilitate condensation polymerization of hydration products. Large quantities of polymer form in the fifth stage. Simultaneously, reaction rate of GGBFS and hydration heat diminish owing to consumption of hydroxide. In the last stage, crystallized hydration products including C-S-H, hydronephelite and natrolite grow continuously.

2.5.3 Mechanical properties and durability of AAS

GGBFS activated by sodium silicate has rapid and high development in strength. It was reported that AAS concrete can develop compressive strength of 68.1 MPa and 117.0 MPa at 1 day and 28 days, respectively (Pu 2010). Such high early strength is difficult to achieve using Portland cement (Wang et al. 1995). Collins and Sanjayan (2001) found curing conditions play an important role in strength of AAS. AAS immersed in saturated lime water had continuous growth in compressive strength until 365 days, while AAS sealed in polyethylene bags gained little improvement on compressive strength after 91 days. Gradual reduction was observed in strength of AAS exposed to air after 56 days. The exposed specimens showed visible micro-cracks on surface and suffered compressive strength loss of 54% as compared with bath cured ones at 365 days.

Dense micro-structure offers AAS not only high strength but outstanding anti-permeability and resistance to chemical attack. AAS concrete can keep its imperviousness under water pressure of 4 MPa for 24 hours, which is superior to OPC concrete by 1.8 MPa even though the latter is improved by silica fume (Wang et al. 1995). Shi (2003) tested corroded depth of AAS paste immersed in nitric acid and acetic acid with pH value of 3.0. Test results showed AAS specimens corroded more slowly than OPC ones in the acid solution. Difference in performance of AAS and OPC can be attributed to their different hydration products. There are C-S-H with higher Ca/Si ratio and more calcium hydroxide and calcium sulphoaluminates in OPC than AAS. Once corroded by acid, calcium hydroxide and calcium sulphoaluminates dissolve and C-S-H releases most lime, which leave a porous layer to OPC and cannot resist further attack. In contrast, Si-rich C-S-H in AAS leaves a layer of silica and aluminosilicate gels to protect uncorroded paste (Pavlík 1994). Low $Ca(OH)_2$ content provides AAS with good fire resistance owing to exemption of CaO-induced expansive cracking at elevated temperature. Research results have indicated fire resistance of AAS is better than that of OPC (Zheng et al. 2009). High alkalinity and low permeability of AAS contribute to passivate reinforcements and isolate them from aggressive media. Diffusion rate of chloride ions in AAS is much lower than that in OPC concrete (Roy et al. 2000). Kukko and Mannonen (1982) immersed AAS concrete in saline water for one year. No rust was observed on steel bars embedded in the concrete. Pu (2010) accelerated corrosion of steel bars embedded in concrete using drying-wetting cycle. He found corrosion-induced mass loss of bars was 0.18% in AAS concrete after 75 cycles while that rose to 1.9% in OPC concrete after only 45 cycles. Degree of corrosion of reinforcements in AAS is closely related to the fineness of GGBFS, alkali content and water slag ratio of AAS. Fine GGBFS, high alkali content and low water slag ratio are beneficial to improve chloride threshold and compactness of AAS and to protect reinforcements (Chen 2008).

Although AAS exhibits excellent strength and durability, there are drawbacks to be solved before application of this new material. AAS has relatively high alkali content over 3% of slag mass (Puertas et al. 2009). High alkalinity accelerates hydration reaction and development of strength, but causes rapid setting. It was reported that initial setting was less than 15 minutes for AAS with high alkali content (Chang 2003; Wang 1991). Such rapid setting of AAS hinders its application. Scholars have developed various retarders, such as gypsum, phosphoric acid, soluble zinc salts and barium salts, to extend setting of AAS to a reasonable level (Chang et al. 2005; He et al. 2010; Zhang and Pan 2010). Zinc salts and barium salts have been proved to be effective retarders without negative effect on strength. However, the retarders increase cost of AAS. Additionally, excessive alkali will lead to efflorescence and drying shrinkage. Free alkali leaches out with evaporation of water and reacts with carbon dioxide in air, which forms carbonate on surface and affects appearance of AAS. AAS has shown great drying shrinkage due to water loss of silica gels during hydration (Melo Neto et al. 2008; Palacios and Puertas 2005; Ye et al. 2017). High shrinkage may weaken strength and durability of AAS. This study tries to solve above problems by optimization of mix proportion and introduction of reinforcements in AAS.

2.6 Summary

In this chapter, a literature review is presented to introduce mechanism and process of chloride-induced corrosion, hazards of corroded reinforcement on structural safety, techniques for protecting reinforcements and strengthening corroded structures, and properties of AAS. Following summaries can be drawn based on the literature review.

1. Corrosion of reinforcement is an electrochemical reaction in which chloride ions act as catalysts to destroy passivated films on reinforcements and initiate the corrosion.

2. Chloride threshold for corrosion is closely related to alkalinity, binder and admixture of concrete, interface between concrete and reinforcements, thickness of cover, moisture

and oxygen content in concrete, and environmental temperature.

3. Corrosion reduces cross section of reinforcement, weakens bond between reinforcement and concrete, and causes severe deterioration in loading capacity and ductility of concrete structures. Corrosion-induced expansion may spall concrete cover, which destroys integrity of structure and accelerates corrosion.

4. Increasing thickness of concrete cover, enhancement of compactness of concrete, and application of corrosion inhibitors are economical and effective methods to prevent corrosion of reinforcements.

5. Common strengthening methods have their limitations in strengthening corroded structures. Steel jackets and plates are unsuitable to chloride-contaminated structures. Concrete jackets reduce usable area of buildings. FRP and polymer-modified mortar prematurely fail at moderate temperature. Ferrocement jackets, by contrast, have the advantages of low cost, thin thickness, good mechanical performance and fire resistance, and turn out to be an appropriate strengthening technique for corroded structures.

6. AAS has higher strength, better durability and lower energy consumption than OPC. High alkalinity and low permeability of AAS contribute to prevent reinforcements from chloride attack. These properties make AAS an ideal material for strengthening corroded concrete structures.

CHAPTER 3

EFFECT OF ALKALI CONTENT AND MODULUS OF ACTIVATOR ON MECHANICAL PROPERTIES AND DURABILITY OF AAS

3.1 Introduction

Corrosion deterioration has endangered the structural integrity of reinforced concrete structures. AAS, as a high-strength and low-cost material, possesses potential in strengthening corroded structures. Mechanical properties and durability of AAS depend largely on alkali content (mass ratio of Na_2O to GGBFS) and modulus of activator (mass ratio of SiO_2 to Na_2O) (Bakharev et al. 1999; Chi 2012; Fernández-Jiménez et al. 1999). This chapter explores the effect of alkali content and modulus of activator on strength, drying shrinkage, setting time, and chloride resistance of AAS. Activators with different alkali contents and moduli were used to activate GGBFS. Flexural test, compressive test, shrinkage test, setting test and rapid chloride penetration test were conducted on AAS specimens. Mathematical models were established to describe strength, drying shrinkage, setting time and charge passed of AAS as a function of experimental variables. Performance of AAS was compared to OPC under the same water binder ratio.

3.2 Materials and specimens

3.2.1 Materials

GGBFS used in this study was Type S95 to Chinese Standard GB/T 18046-2008 (2008). Its chemical composition is given in Table 3.1 below.

Table 3.1 Composition of GGBFS (by mass)

Oxides	MgO	Al_2O_3	SiO_2	SO_3	K_2O	CaO	TiO_2	MnO	Fe_2O_3
Percentage	5.62	11.46	30.60	2.62	1.09	45.55	1.83	0.60	0.64

The basicity coefficient $K_b=(CaO+MgO)/(SiO_2+Al_2O_3)$ is equal to 1.22. Researches have reported that AAS activated by sodium silicate can achieve higher strength as compared with $NaOH$ or Na_2CO_3 (Bakharev et al. 1999; Fernández-Jiménez et al. 1999; Wang et al. 1994; Živica 2007). The activator adopted in this study was liquid sodium silicate with a modulus of 2.35 and Na_2O of 14.5% and SiO_2 of 34% by mass. Granular NaOH with a purity of 99% was mixed into sodium silicate solution to achieve the specified modulus. Fine aggregates obtained from river sand were dried in an oven at 105℃ for 24 hours and sieved with mesh size of 2.36 mm. OPC equivalent to ASTM Type I was used as reference binder.

3.2.2 Design of mix proportion and preparation of specimens

Two factors, alkali content and modulus of sodium silicate solution, were examined. Based on the preliminary test results, applying Na_2O more than 6% by mass of GGBFS could lead to large shrinkage and rapid setting. Insufficient alkali dosage may not effectively activate GGBFS. AAS mortar activated by 1% Na_2O could not be demoulded after 3-day curing due to slow strength development. According to Krizan and Zivanovic (2002), suitable modulus ranges from 0.6 to 1.5 in considering the effect of shrinkage on strength of AAS. A full factorial experiment (5×3) was employed. Na_2SiO_3 solutions with Na_2O contents ranging from 2% to 6% and moduli of 0.6, 0.9, and 1.2 were adopted. OPC specimens were prepared as reference. Water binder ratio and binder sand ratio were kept constant at 0.44 and 0.5, respectively (Table 3.2).

As shown in Table 3.2, a total of 16 groups of mixes, including 15 groups of AAS and one group of OPC, were prepared. In each group, six prismatic specimens (40×40×160 mm), four prismatic specimens (25×25×285 mm) and two cylinders (D100×200 mm) were prepared for strength test, drying shrinkage test and chloride penetration test, respectively. Procedure for preparing AAS mortar is given as follows:

1. Mix granular NaOH, water and liquid sodium silicate, and cool down the solution to room temperature.
2. Place the mixed solution and GGBFS in a mixer and mix them for 30 seconds at low speed. Add sand during mixing. Shift the mixer to medium speed and mix the mortar for 30 seconds. Suspend the mixing and scrape down the mortar on sides of the bowl. Mix the mortar for another 60 seconds at medium speed.
3. Cast the mortar into moulds and compact using a vibrating table. Cover the specimens with polyethylene film.
4. The specimens are removed from moulds 24 hours after casting, and cured in water at 27°C.

Besides mortar, AAS and OPC paste were also prepared for setting time test.

Table 3.2 Mix design of AAS and OPC

Group	Na_2O content	Modulus	Water binder ratio	Binder sand ratio (for mortar specimen)
1 / 2 / 3	2%	0.6 / 0.9 / 1.2	0.44	0.5
4 / 5 / 6	3%	0.6 / 0.9 / 1.2		
7 / 8 / 9	4%	0.6 / 0.9 / 1.2		
10 / 11 / 12	5%	0.6 / 0.9 / 1.2		
13 / 14 / 15	6%	0.6 / 0.9 / 1.2		
OPC	-	-		

3.3 Experimental test

3.3.1 Setting time test

Initial and final setting time of AAS and OPC paste were examined by a Vicat apparatus according to BS EN 196-3 (2005). Fresh paste was filled into a mould and placed under the Vicat apparatus. A needle used for initial setting was lowered until it contacted the paste and was released quickly to penetrate into the paste. The distance between the baseplate of mould and the needle was recorded. The time from mixing to the moment at which the distance reached 6 mm was defined as the initial setting time.

When the initial setting time was measured, the mould was inverted to expose the bottom of paste for testing the final setting time. Final setting test had a ring attachment at the end. The needle was lowered in the same way as the initial setting test. When the ring of needle fails to mark on the surface of paste, the paste reached its final setting time. During the intervals of testing, the paste was cured in water.

Figure 3.1 Setting test

3.3.2 Flexural and compression test

Flexural and compressive strength of AAS and OPC mortar were examined at both 7 and 28 days. A three-point flexural test was conducted on prismatic specimens by displacement control at 0.5 mm/min according to BS EN 13892 (2002) (Figure 3.2). According to Raphael (1984), three-point flexural test is an indirect tensile test like splitting tensile test that can reflect the tensile performance of material. Flexural strength ("f_f") can be obtained by the following equation.

$$f_\mathrm{f}=\frac{1.5F_\mathrm{f}l}{bd^2} \tag{3.1}$$

where F_f is the maximum load applied on specimens; l is the distance between two hinge supports; b and d are the width and height of cross-section, respectively.

Figure 3.2 Flexural test on AAS mortar

Fractured specimens obtained from the flexural test were used for measurement of compressive strength of AAS. Two steel plates with dimension of 40 × 40 × 10 mm were placed above and beneath the fractured parts (Figure 3.3). Loading rate of compression test was 2.4 kN/s. Compressive strength (f_c) can be obtained by the following equation.

$$f_c = \frac{F_c}{A} \tag{3.2}$$

where F_c is the maximum load obtained frrom compression test, and A is cross-section area of specimen, 1600 mm^2.

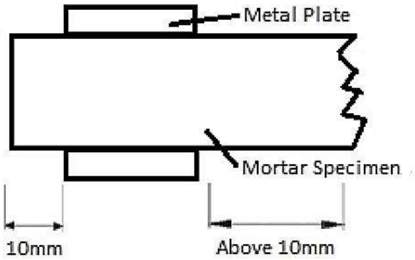

Figure 3.3 Compression test on AAS mortar

3.3.3 Drying shrinkage test

According to ASTM C1148-92a (2014), prismatic specimens were water-cured for 72 hours from the time of casting. The initial lengths (“L_1”) of specimens were then measured by a length comparator. Afterwards, the specimens were stored in a drying chamber at 25℃ and relative humidity of 50%. The length (“L”) of specimens were then measured every day in the first week, semiweekly in the following three weeks, and weekly until 112 days (Figure 3.4). Drying shrinkage of specimens is calculated by the following equation:

$$S=\frac{L_1\text{-}L}{L_0} \tag{3.3}$$

where L_0 is the length of the gauge, 250 mm.

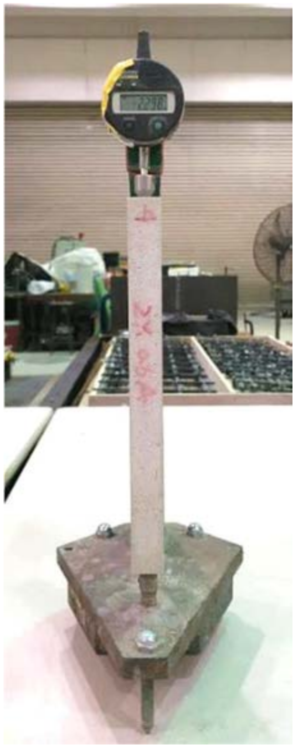

Figure 3.4 Drying shrinkage test

3.3.4 Rapid chloride penetration test

Rapid chloride penetration test was conducted at 28 and 90 days. According to ASTM C 1202 (2012), slices with thickness of 50 mm and diameter of 100 mm were cut from the middle portion of AAS cylinders. The slices were coated with epoxy around their circumferences. After the epoxy hardened, the slices were placed in a vacuum desiccator with their end faces exposed. Vacuum was maintained at a constant pressure of -6650 Pa. After three hours, water was injected into the desiccator to cover the specimens and with vacuum pump running for an additional hour (Figure 3.5). The specimens were soaked in water for 18 hours and then placed between a pair of cells and clamped. The cells were filled with NaOH solution (0.3N) and NaCl solution (3% by mass), acting as anode and cathode, respectively (Figure 3.6). A constant voltage of 60V was applied to the specimens for six hours. Under the external voltage, Cl^- and Na^+ will migrate and gather at the anode and cathode, respectively. The higher permeability specimens have, the more ions pass, and the stronger current is. The current passed was recorded at intervals of one minute by a data logger.

Figure 3.5 Vacuuming specimens in a desiccator

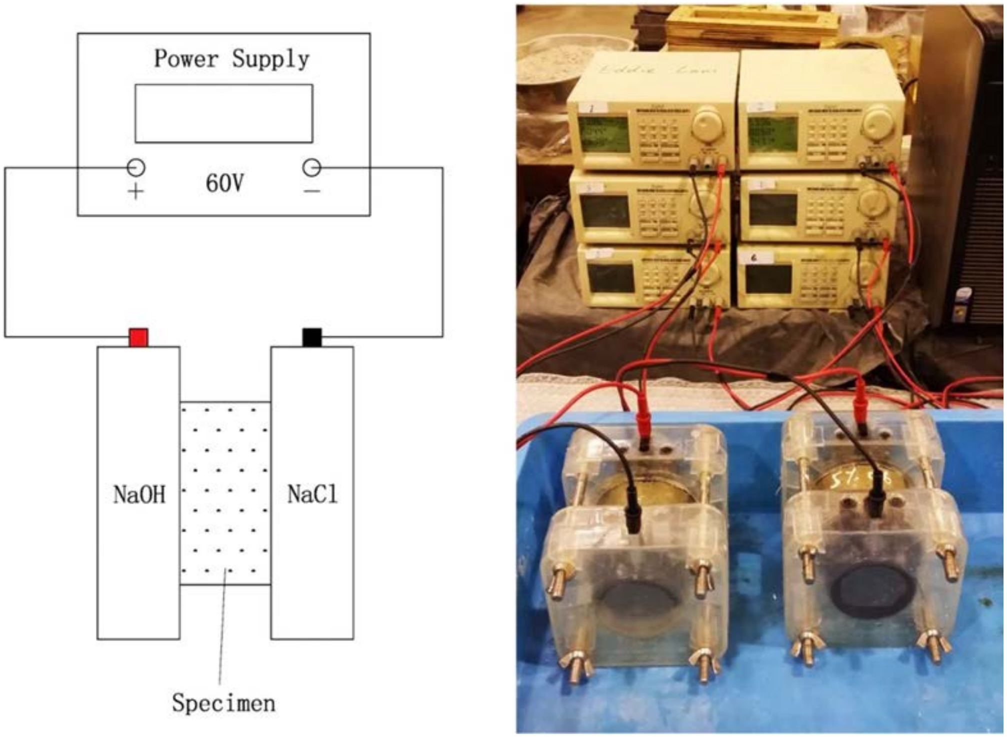

Figure 3.6 Rapid chloride penetration test

3.4 Results and discussion

3.4.1 Setting time

Initial and final setting time of AAS with varying alkali contents and moduli are given in Figure 3.7 and Figure 3.8, respectively. Both alkali content and modulus of activator play prominent role in setting time of AAS. The higher the alkali content and modulus are, the more rapidly the AAS sets. As the dosage of Na_2O increased from 2% to 6%, the average initial and final setting time were shortened from 12.4 and 15.6 hours to 0.9 and 1.5 hours, respectively. Increasing moduli from 0.9 to 1.2 reduce initial and final setting time by 78% and 70%, respectively. Rapid setting of slag in sodium silicate solution with high alkali content and modulus can be attributed to the promotion of OH^- and SiO_4^{4-} on hydration of AAS. OH^- in sodium silicate solution acts as destructive catalyst to break Ca-O bond in slag, and releases abundant Ca^{2+} into the solution. The metallic cations react with SiO_4^{4-} in sodium silicate and generate C-S-H gel between slag grains (Krizan and Zivanovic 2002). High concentration of OH^- and SiO_4^{4-} accelerate the reaction and setting of AAS (Chang 2003). Previous studies by Krizan and Zivanovic (2002), Shi and Day (1996) indicated that higher sodium silicate dosage can lead to earlier acceleration period and higher accelerated hydration peak of AAS.

AAS has always been regarded as a binder with rapid setting and hence difficult to be utilized in commercial practice (Chang 2003). The results in this study, however, showed that average setting time of AAS with alkali content of 2% and 3% was longer than that of OPC. This suggests high alkali content promotes rapid setting in AAS. Reducing alkali content to 3-4% can extend setting time of AAS to a level comparable to OPC and facilitate construction of AAS.

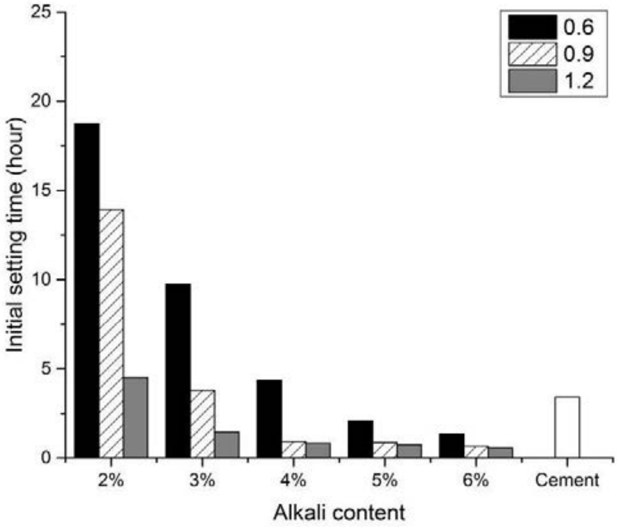

Figure 3.7 Initial setting time

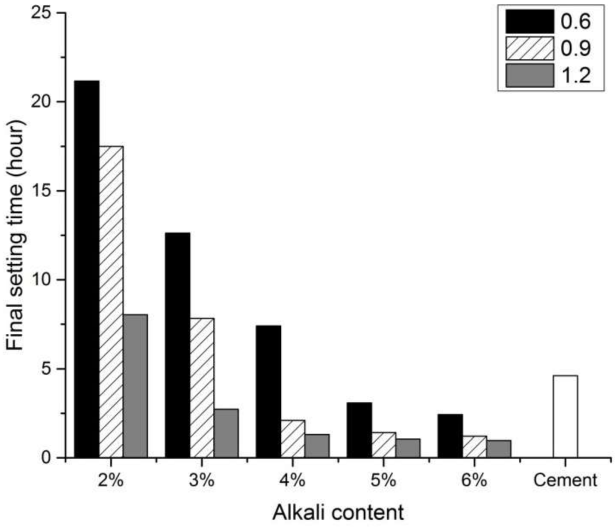

Figure 3.8 Final setting time

3.4.2 Drying shrinkage

Drying shrinkage of AAS mortar is shown in Figure 3.9. Shrinkage strain of AAS specimens ranged from 0.0027 to 0.0052 at 112 days, which were noticeably larger than that of OPC. This large distance in shrinkage is related to their difference in pore size distribution and hydration product. AAS has lower porosity but larger proportion of mesopores (i.e. radius of pores ranging from 1.25 to 25 nm) than OPC (Collins and Sanjayan 2000; Melo Neto et al. 2008; Shi 1996). Evaporation of water from mesopores causes capillary tension in pores and increases shrinkage. Moreover, the initial hydration product of AAS contains a large amount of silica gel which has high water content at about 90%. Once drying, the gel shrinks sharply and contributes to total shrinkage of AAS (Glukhovskij et al. 1983; Krizan and Zivanovic 2002).

Shrinkage strain of AAS rose sharply in the early age, but slowed down as age increased. When the age exceeded 60 days, the shrinkage strain leveled off. Most of shrinkage of AAS was generated during the early age, especially for the specimens with high Na_2O dosage and modulus. The proportion of 7-day to 112-day shrinkage was 34% for AAS with Na_2O content of 2% and modulus of 0.6, compared to 60% for AAS with Na_2O content of 6% and modulus of 1.2. Alkali content of activator exerted primary influence on drying shrinkage of AAS. As amount of Na_2O increased from 2% to 6%, average shrinkage value rose by 63% at 112 days. Increasing dosages of sodium silicate cause larger proportion of mesopores in total pore distribution and faster refinement of pore size, which explains the phenomenon that AAS with higher alkali content shows earlier and larger shrinkage strain. Modulus of sodium silicate also made a considerable contribution to drying shrinkage of AAS mortar. Shrinkage value increased with modulus under the same alkali content. Sodium silicate with high modulus can supply abundant silicate ions for hydration of AAS, but also form C-S-H gel which is easy to shrink in dry environment (Melo Neto et al. 2008).

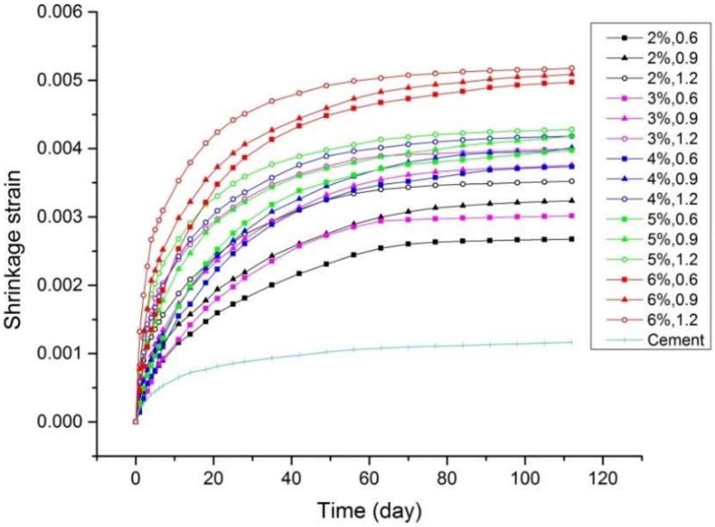

Figure 3.9 Drying shrinkage of AAS

3.4.3 Flexural and compressive strength

Variations of flexural strength of AAS with alkali content and modulus at 7 and 28 days are given in Figure 3.10 and Figure 3.11, respectively. AAS with Na_2O content of 2% developed slowly in early strength and cannot be demoulded until three days after casting. This phenomenon coincides with the finding in setting test that low alkalinity retarded the setting of AAS. High alkali content accelerated hydration process of AAS and resulted in higher 7-day strength. 28-day flexural strength of AAS, in contrast, ascended initially but declined with increasing alkali contents. With Na_2O content of 3% and modulus of 0.6, flexural strength of AAS reached its maximum value of 11.03 MPa. When alkali content exceeded 3%, there was no further increase, but reduction in flexural strength at 28 days (Figure 3.11). The flexural strength of AAS fell to 7.81 MPa when alkali content and modulus increased to 6% and 1.2, respectively. The reduction in flexural strength of AAS with increasing ages was also reported by Fernández-Jiménez et al (1999). This is attributed to shrinkage induced by redundant alkali activator (Melo Neto et al. 2008). An observation was conducted on two AAS slices cut from the middle portion of AAS cylinders and one AAS ferrocement specimen. The alkali contents of the two AAS slices and one AAS ferrocement specimen were 3%, 6%, and 9%, respectively. After cured in water for 28 days, there is no visible crack on the cross-section of the AAS slice with alkali content of 3%, while one crack was observed in the middle of the slice with alkali content of 6% (Figure 3.12 and Figure 3.13). As the alkali content increased to 9%, there were numerous cracks on the AAS ferrocement specimen (Figure 3.14). This is due to high alkalinity that causes large shrinkage and reduces flexural strength of AAS. Hydration of AAS can be intensified under high alkalinity and consumes the water in C-S-H gel. Interior of AAS specimens suffers from water loss which cannot be recovered by curing due to dense structure of AAS (Ye et al. 2017). This self-desiccation of hydration products not only results in large shrinkage of AAS, but breaks the bonding between slag particles (Krizan and Zivanovic 2002). Increasing silicate contents result in higher shrinkage of AAS due to an increase in C-S-H gel. Modulus of sodium silicate solution, hence, plays a negative role on the performance of AAS in flexural test. For each group under the same alkali level, flexural strength declined with increasing moduli (Figure 3.11). This agrees with the observation by Duran Atis et al. (2009) that increasing moduli cause shrinkage, leads to micro cracking in AAS matrix and seriously deteriorates the flexural strength. Wang and Scrivener (1995) and Ben Haha et al. (2011) compared hydration products of GGBFS activated by Na_2SiO_3 with modulus of 1.0 and NaOH (i.e. modulus=0). The C-S-H gel is less crystalline and contains more water in Na_2SiO_3 activated GGBFS, which indicates SiO_3^{2-} weakens the resistance of AAS to shrinkage.

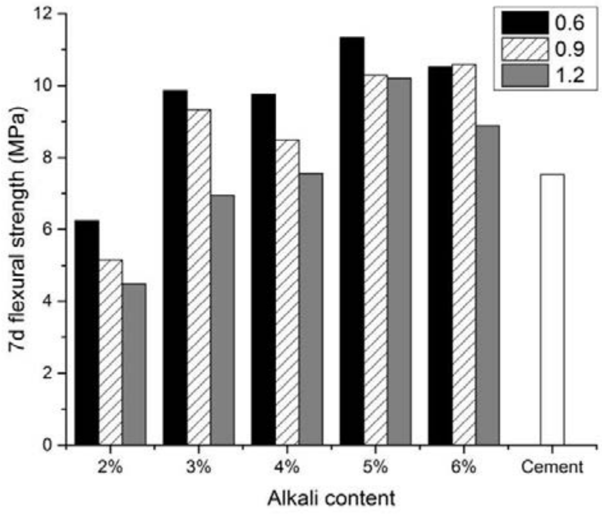

Figure 3.10 7-day flexural strength

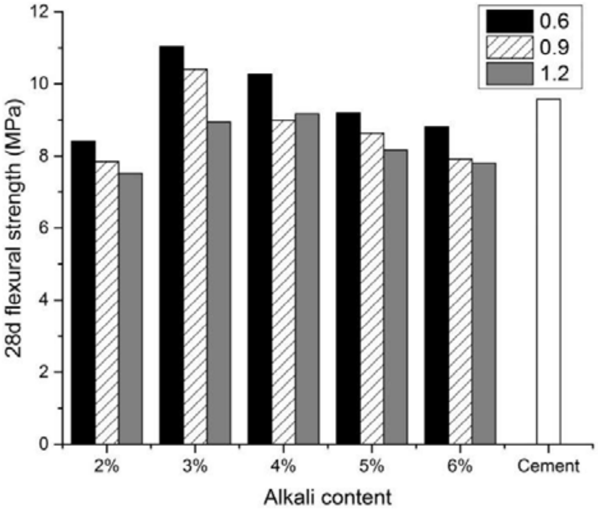

Figure 3.11 28-day flexural strength

Figure 3.12 AAS slice with alkali content of 3% and modulus of 1.2

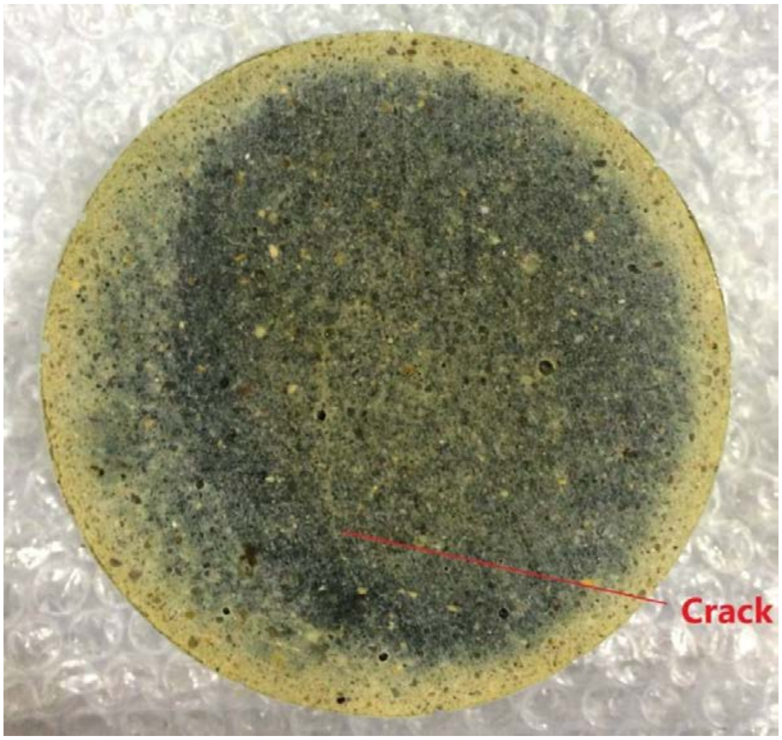

Figure 3.13 AAS slice with alkali content of 6% and modulus of 1.2

Figure 3.14 AAS with alkali content of 9% and modulus of 1.2

Figure 3.15 and Figure 3.16 show compressive strength of AAS with different alkali contents and moduli at 7 and 28 days, respectively. There were varying degrees of growth in compressive strength at 28 days compared to that at 7 days. Development of strength was mostly accomplished at the early age of AAS with high Na_2O dosage owing to promotion of alkali in hydration reaction. Different from flexural strength, both 7-day and 28-day compressive strength experienced a steady rise with increasing alkali contents and moduli. AAS with alkali content of 6% and modulus of 1.2 achieved the highest 7-day and 28-day compressive strength of 82.9 and 94.5 MPa, respectively. When the alkali content and modulus of AAS decreased to 2% and 0.6, respectively, its

7-day and 28-day compressive strengths were only a quarter and one third of the highest values, respectively. According to Neto et al. (2008) and Ben Haha et al. (2011), increasing dosages of Na_2O and SiO_3^{2-} can intensify hydration and formation of C-S-H gel, which contributes to denser microstructure and higher compressive strength. Although large amount of alkali activator may cause shrinkage and even micro-cracking in AAS, compressive strength is not as sensitive to cracking as flexural strength. It is because shrinkage-induced cracks propagate along transverse direction of specimens, i.e. perpendicular to tensile stress induced by flexure. The initiation and growth of cracks reduce the available area to carry tensile force. This reduction causes an increase in stresses at critical crack tips, which results in rapid propagation of crack until fracture of specimen. Different from tensile failure, compressive failure of specimen is caused by compressive stress acting parallel to the crack in the middle of specimen. The cracks separate mortar into individual prisms, but the separated prisms can still resist compression. Total effective area to resist compression remains constant. The effect of shrinkage-induced cracks on compressive strength is less significant than that on flexural strength of mortar. Alkali content of 2% is insufficient to arouse the potential of GGBFS. Alkali content higher than 5%, however, may cause large shrinkage and high cost. An appropriate Na_2O dosage ranging from 3% to 4% is therefore recommended to develop AAS with comparable flexural and compressive strength to OPC.

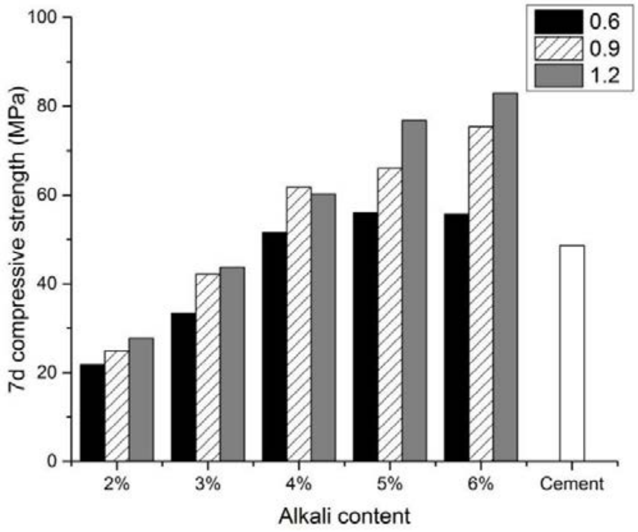

Figure 3.15 7-day compressive strength

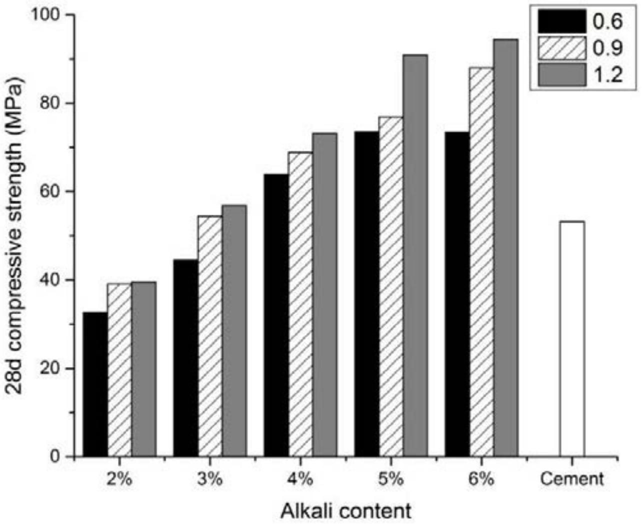

Figure 3.16 28-day compressive strength

In order to examine the variation of strength of AAS with age, flexural strength and compressive strength of AAS with modulus of 0.9 were tested at 90 days. The results are given in Figure 3.17 and Figure 3.18. AAS experienced sustainable growth in compressive strength after 28 days, but the growth was much less than that between 7 days and 28 days. Compared with that at 28 days, flexural strength at 90 days increased somewhat in AAS with alkali contents ranging from 2% to 3%, but reduced slightly when alkali content exceeded 4%. The difference in flexural strength of AAS between 28 and 90 days is less than 7%. Influence of shrinkage in flexural strength of AAS tends to reduce over time. This finding is also supported by the results of drying shrinkage. Most of the shrinkage was achieved at 28 days. 28-day strength can therefore be adopted as an indicator to evaluate mechanical performance of AAS.

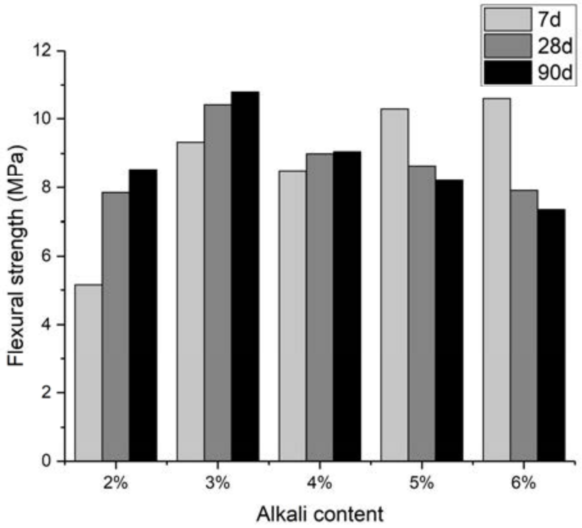

Figure 3.17 90-day flexural strength of AAS with modulus of 0.9

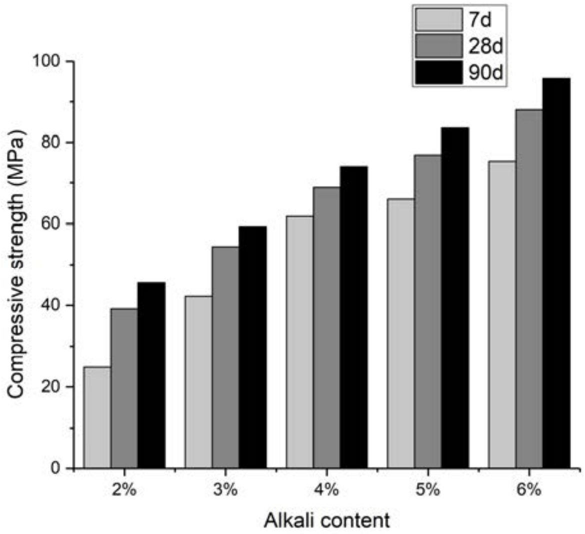

Figure 3.18 90-day compressive strength of AAS with modulus of 0.9

3.4.4 Chloride ion permeability

Total charge passed is given in Figure 3.19 and Figure 3.20. Charge passed in rapid chloride penetration test depends on both characteristics of pore structure and electrical conductivity of pore solution. The difference in chemical composition of pore solution between AAS and Portland cement will also affect charge passed in the test. Therefore, it cannot evaluate the resistance of different materials to chloride by comparison of charge passed only. Nevertheless, results of rapid chloride penetration test reflect migration rate of ions through specimens, which can be used to compare permeability of same material qualitatively. Douglas et al (1992), Shi (1996) and Al-Otaibi (2008) applied this test to evaluate permeability of AAS with different mix proportions. This test is also used in this study to examine effect of alkali content and modulus on permeability of AAS. Average charge through AAS at 90 days declined by 43% as compared with that at 28 days. The reduction in charge is related to densification of microstructure and decreasing ion concentration of pore solution in AAS with increasing curing time (Roy et al. 2000). As hydration proceeds, pore structure of AAS is refined and alkali ions are consumed by hydration reaction, which markedly decreases the charge through AAS. The electric flux gradually increased with increasing alkali contents, whereas it declined slightly under increasing moduli in the AAS hydrated for 90 days. These opposite effects of alkali content and modulus on permeability of AAS can be explained by alkali induced micro cracks and filling micro pores by silica gel, respectively.

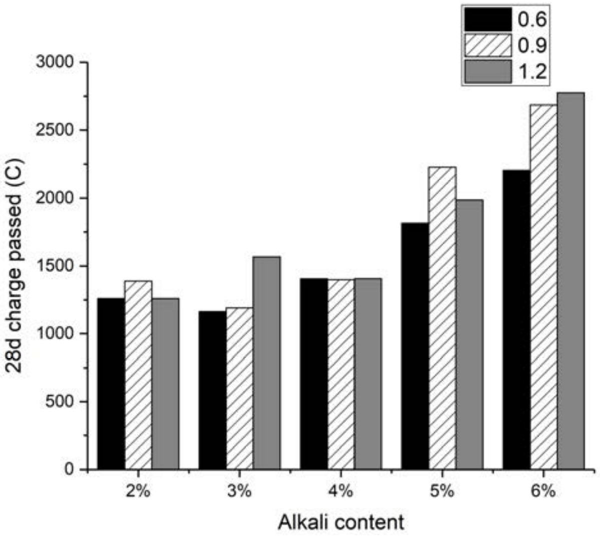

Figure 3.19 28-day charge passed

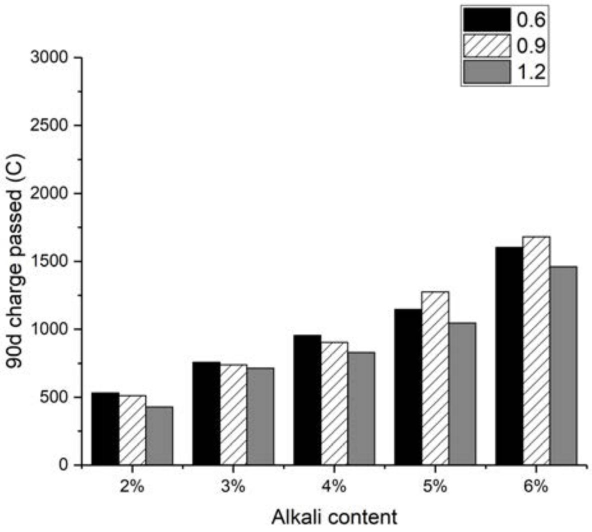

Figure 3.20 90-day charge passed

3.5 Summary

In this chapter, a complete factorial experiment was conducted to explore the effect of alkali content and modulus of sodium silicate on mechanical performance and chloride permeability of AAS. GGBFS was activated by sodium silicate solution with various alkali contents from 2% to 6% and moduli from 0.6 to 1.2. AAS was subjected to setting test, drying shrinkage test, three-point flexural test, compressive test and rapid chloride penetration test. Performance of AAS was also compared to that of OPC under equivalent water binder ratio. Based on the experimental results, the following can be drawn.

1. Both initial and final setting of AAS paste accelerate with increasing alkali contents and moduli of sodium silicate. AAS activated by sodium silicate solution with Na_2O content of 3% and modulus of 0.9 exhibits initial and final setting time of 3.8 and 7.8 hours, close to OPC.

2. Drying shrinkage of AAS mortar increases gradually with alkali content and modulus. Early shrinkage accounts for a large proportion of total shrinkage strain in AAS with high dosages of Na_2O and SO_3^{2-}. All the AAS specimens have shrinkage higher than that of OPC regardless of alkalinity and modulus.

3. High alkali content increases early strength, but reduces 28-day flexural strength of AAS owing to redundant alkali-induced shrinkage. Modulus plays negative influence on flexural strength of AAS. Alkali contents at 3-4% can activate AAS with flexural performance comparable to OPC.

4. With increasing alkali contents and moduli, there is a steady improvement in both 7-day and 28-day compressive strength of AAS. AAS can achieve the highest compressive strength of 94.5 MPa at 28 days.

5. The charge through AAS experiences a progressive increase with alkali content, but diminishes slightly with growing modulus. Water curing can improve the resistance of AAS to chloride ion penetration.

CHAPTER 4

OPTIMIZATION OF AAS MORTAR FOR STRENGTHENING CORRODED CONCRETE STRUCTURES

4.1 Introduction

The influence of alkali content and modulus of sodium silicate to the performance of AAS was qualitatively evaluated in the last chapter. This chapter aims to establish quantitative relationships from the experimental results and optimize a mix proportion of AAS for strengthening corroded concrete structures. To distinguish variation of experimental factors from errors, significance of experimental factors, such as alkali contents, moduli and their interactions, was assessed by analysis of variance ("ANOVA"). Mathematical models were established to describe the strength, drying shrinkage, setting time and charge passed of AAS as a function of the significant factors. A comprehensive evaluation of AAS was conducted based on the models with consideration of setting time, strength and durability. Effectiveness of the optimized AAS with corrosion inhibitors was then evaluated by artificially accelerated corrosion test.

4.2 Significance analysis and optimization of AAS

4.2.1 Significance and regression analysis on experimental factors

Six groups of test results, namely 28-day flexural strength, 28-day compressive strength, 90-day charge passed, initial setting time, final setting time and 112-day drying shrinkage were employed in significance analysis and optimization of AAS. A two-way ANOVA was conducted to identify the key factors (alkali content, modulus and their interaction) which play statistical significance on the test results (Table 4.1). SS_X, SS_Y, SS_{XY}, SS_e and SS_T are the sum of squares caused by factor "X" (alkali content), factor

"Y" (modulus), their interaction "XY", experimental error "e", and total sum of squares "T" (Equations (4.1)- (4.5)). *r*, *s* and *t* are the total levels of the factors X, Y, and times of repetition, respectively. $\bar{z}$ is mean value of all test values. $\overline{z_i}$ and $\overline{z_j}$ are mean values of the test values under factor "X" of *i* and factor "Y" of *j*, respectively. $\overline{z_{ij}}$ is mean value of the test values when factor "X" is *i* and factor "Y" is *j* (Equations (4.6) - (4.9)).

Table 4.1 ANOVA of experimental factors

Variance source	Sum of squares	Degrees of freedom	Mean square	*F*-value
X	SS_X	r-1	$MS_X = SS_X/(r-1)$	$F_X = MS_X / MS_e$
Y	SS_Y	s-1	$MS_Y = SS_Y/(s-1)$	$F_Y = MS_Y / MS_e$
XY	SS_{XY}	(r-1)(s-1)	$MS_{XY} = SS_{XY}/[(r-1)\ (s-1)]$	$F_{XY} = MS_{XY} / MS_e$
Error	SS_e	rs(t-1)	$MS_e = SS_e/[rs(t-1)]$	-
Total	SS_T	rst-1	-	-

$$SS_X = st\sum_{i=1}^{\mathrm{r}}(\overline{z_i}-\bar{z})^2 = \frac{1}{st}\sum_{i=1}^{r}\left(\sum_{j=1}^{s}\sum_{k=1}^{t}z_{ijk}\right)^2 - \frac{1}{rst}\left(\sum_{i=1}^{r}\sum_{j=1}^{s}\sum_{k=1}^{t}z_{ijk}\right)^2 \tag{4.1}$$

$$SS_Y = rt\sum_{j=1}^{s}\left(\overline{z_j}-\bar{z}\right)^2 = \frac{1}{rt}\sum_{j=1}^{s}\left(\sum_{i=1}^{r}\sum_{k=1}^{t}z_{ijk}\right)^2 - \frac{1}{rst}\left(\sum_{i=1}^{r}\sum_{j=1}^{s}\sum_{k=1}^{t}z_{ijk}\right)^2 \tag{4.2}$$

$$\begin{aligned} SS_{XY} &= t\sum_{i=1}^{r}\sum_{j=1}^{s}\left(\overline{z_{ij}}-\overline{z_i}-\overline{z_j}+\bar{z}\right)^2 \\ &= \frac{1}{t}\sum_{i=1}^{r}\sum_{j=1}^{s}\left(\sum_{k=1}^{t}z_{ijk}\right)^2 - \frac{1}{st}\sum_{i=1}^{r}\left(\sum_{j=1}^{s}\sum_{k=1}^{t}z_{ijk}\right)^2 - \frac{1}{rt}\sum_{j=1}^{s}\left(\sum_{i=1}^{r}\sum_{k=1}^{t}z_{ijk}\right)^2 + \frac{1}{rst}\left(\sum_{i=1}^{r}\sum_{j=1}^{s}\sum_{k=1}^{t}z_{ijk}\right)^2 \end{aligned} \tag{4.3}$$

$$SS_e = \sum_{i=1}^{r}\sum_{j=1}^{s}\sum_{k=1}^{t}\left(z_{ijk}\right)^2 - \frac{1}{t}\sum_{i=1}^{r}\sum_{j=1}^{s}\left(\sum_{k=1}^{t}z_{ijk}\right)^2 \tag{4.4}$$

$$SS_T = SS_X + SS_Y + SS_{XY} + SS_e \tag{4.5}$$

$$\bar{z} = \frac{1}{rst}\sum_{i=1}^{r}\sum_{j=1}^{s}\sum_{k=1}^{t}z_{ijk} \tag{4.6}$$

$$\overline{z_i} = \frac{1}{st}\sum_{j=1}^{s}\sum_{k=1}^{t}z_{ijk} \tag{4.7}$$

$$\overline{z_j}=\frac{1}{rt}\sum_{i=1}^{r}\sum_{k=1}^{t}z_{ijk} \tag{4.8}$$

$$\overline{z_{ij}}=\frac{1}{t}\sum_{k=1}^{t}z_{ijk} \tag{4.9}$$

F-values obtained from ANOVA were compared to the critical values under given confidence levels. F-values greater than $F_{0.05}$ and $F_{0.01}$ have "significant" and "very significant" influence on test results at confidence levels of 95% and 99%, respectively (Figure 4.1). Variations of 28-day flexural strength, 28-day compressive strength, 90-day charge passed, initial setting time, final setting time, and 112-day drying shrinkage of AAS with the "significant" or "very significant" factors were determined by 2nd-order polynomials (Aydin 2013). Coefficients of the polynomials were obtained by regression analysis.

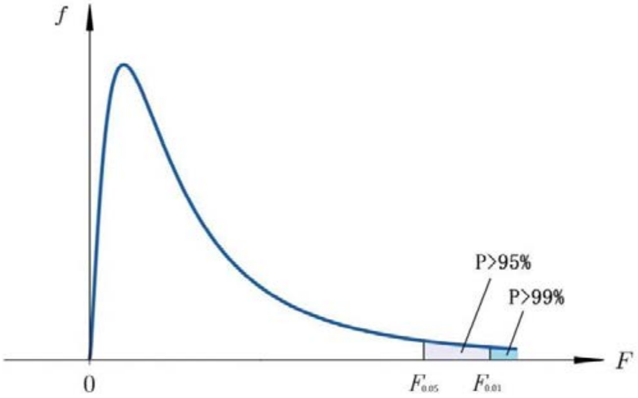

Figure 4.1 Critical values in F-distribution curve

4.2.2 Optimization of AAS

As the proposed material for strengthening corroded concrete structures, AAS should have balanced performances in strength, durability and usability. A single index cannot fully reflect overall performance of AAS. By means of the models established in Section 4.2.1, the best alkali content and modulus can be optimized to produce AAS suitable for strengthening work. In order to eliminate the effect of physical dimensions statistically, the models of 28-day flexural strength, 28-day compressive strength, 90-day charge passed, and 112-day drying shrinkage of AAS were normalized using an extremum method (Equation (4.10)) (Hwang and Yoon 1981).

$$N = \frac{M - \overline{z_{ij}}_{\min}}{\overline{z_{ij}}_{\max} - \overline{z_{ij}}_{\min}} \tag{4.10}$$

where M and N indicate the original and normalized models. In recognizing the positive effect of flexural strength and compressive strength, and the negative effect of chloride resistance and drying shrinkage on optimal AAS, signs of the normalized models were transformed accordingly (Equations (4.11) - (4.14)). For flexural strength and compressive strength,

$$I_f = N_f \tag{4.11}$$

$$I_c = N_c \tag{4.12}$$

For charge passed and shrinkage strain,

$$I_q = -N_q \tag{4.13}$$

$$I_s = -N_s \tag{4.14}$$

where I_f, I_c, I_q and I_s are transformed models of flexural strength, compressive strength, charge passed and shrinkage strain, respectively.

$$I = I_f + I_c + I_q + I_s \tag{4.15}$$

An index I was used to represent the comprehensive performance of AAS (Equation (4.15)). According to Aydin’s study, an equal weighting coefficient was determined for mechanical and durability indexes (Aydin 2013). A higher I-value represents better strength and durability. Cementitious materials should also have a setting time sufficient for mixing and casting before they lose plasticity. However, too long setting time will hinder demoulding and development of strength. ASTM C595 (2017) specifies that the initial setting time of Portland blast-furnace slag cement should not be less than 45 min, and the final setting time should not exceed seven hours. This specification is considered in optimization of AAS. By linear interpolation between tested setting time, available alkali contents and moduli are limited and given in the green part of Figure 4.2. Moreover, mortar for strengthening should perform better than concrete substrate in strength to ensure structural safety (Morgan 1996). Based on the above, AAS with high *I*-value, suitable setting time and strength superior to OPC will be optimized.

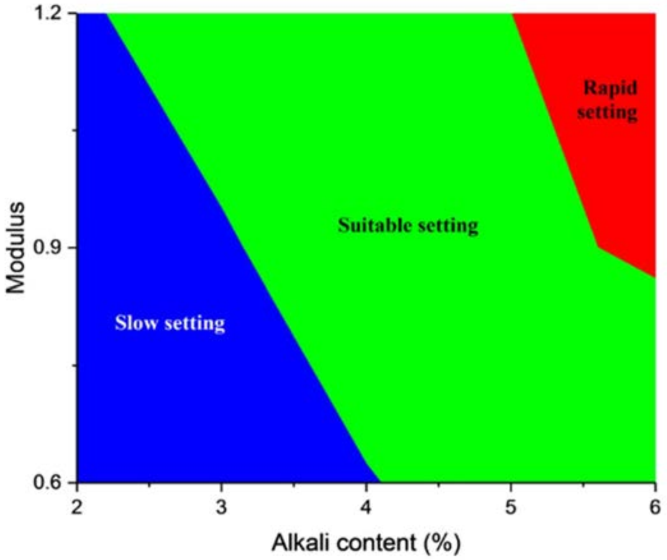

Figure 4.2 Suitable alkali contents and moduli from perspective of setting time

4.3 Artificial accelerated corrosion test on steel reinforcements wrapped by optimal AAS

To examine the protection of optimal AAS on steel reinforcements and effectiveness of corrosion inhibitors in AAS, artificially accelerated corrosion test was conducted on reinforced AAS columns. Five AAS and one OPC mortar columns with cross-section of 200×200 mm and height of 300 mm were prepared (Figure 4.3). Mix proportions of OPC and AAS were the same as the ones used in Section 3.2.2 and optimized in Section 4.2.2, respectively. Except one AAS specimen A0, four AAS specimens were mixed with a commercial corrosion inhibitor ("CCI") or $NaNO_2$, each at 1.5% and 3.0% by mass of GGBFS (Table 4.2). Effective components of the CCI are surfactants and amino alcohol. Four deformed bars with diameter of 12 mm ("T12") were used as main reinforcements. Each deformed bar was polished by a wire brush with 260 mm length unprotected and the rest coated with epoxy. Plain bars of 6 mm diameter ("R6") at 150 mm spacing were used as stirrups. Cover thickness was 38 mm to main reinforcements.

Meanwhile, AAS prismatic specimens (40×40×160 mm) containing the above corrosion inhibitors were prepared.

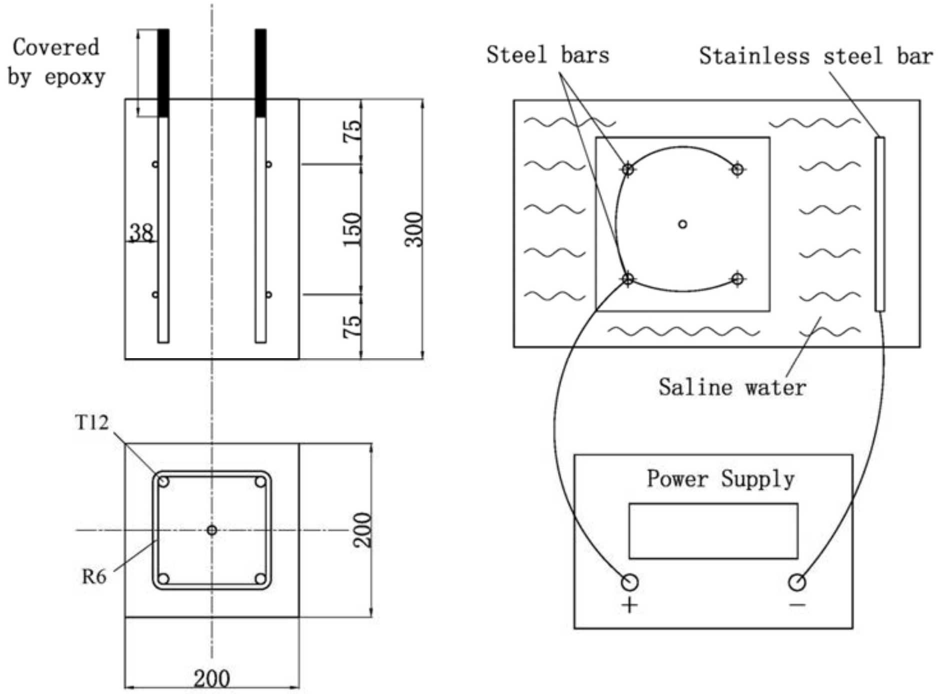

Figure 4.3 Artificially accelerated corrosion test (Unit: mm)

Table 4.2 Details of AAS and OPC column specimens

Specimen ID	P0	A0	B15	B30	C15	C30
Materials	OPC			AAS		
Corrosion inhibitor dosage	-	-	1.5% $NaNO_2$	3.0% $NaNO_2$	1.5% CCI	3.0% CCI

After 28 days of curing, a galvanostatic method was used to artificially accelerate corrosion of reinforcement. Column specimens were immersed in sodium chloride solution (5% by mass) and subjected to impressing anodic direct current. As shown in Figure 4.3, main reinforcements of column specimens were connected to the anode and one stainless steel bar was embedded and connected to the cathode of power supply. Yuan et al (2007) suggested that density of electrical current, i.e. ratio of current to surface area of reinforcements, should not exceed 0.01 mA/mm^2 in galvanostatic accelerated corrosion. Overlarge current will lead to insufficient oxygen in concrete and deficiently oxidized corrosion products. As a result, main product of accelerated corrosion is black ferroferric oxide, rather than brown ferric oxide under natural corrosion. The volume of the former is less than the latter, which underestimates width of cracks induced by corrosion (Lide 1999). In addition, high current will heat up the reinforcements. Part of the electric energy converts into thermal energy, which reduces corrosion of reinforcements than theoretical value (Gan et al. 2011). This phenomenon was also observed in the preliminary test. Concrete specimen became overheated when electric current density was 0.015 mA/mm^2. According to Faraday's laws of electrolysis, polarization time "*t*" can be obtained from following equation.

$$t = \frac{m\mathrm{Fz}}{I\mathrm{M}} \tag{4.16}$$

where *m* is mass of corroded reinforcement, obtained by multiplying mass of raw reinforcements by objective degree of corrosion of 10%; F is the Faraday constant, 96485.34 C/mol; z is the valence of ferrous ion; *I* is constant current applied to reinforcements, 0.23A in this study, less than the upper limit suggested by Yuan et al (2007); and M is the molar mass of iron, 56 g/mol.

After accelerated corrosion test, the specimens were then split along corrosion-induced cracks. To evaluate the degree of corrosion, main reinforcements were removed from specimens and cleaned by brushing in acid solution. According to ASTM G1-03 (2003), the solution was pre-made by first dissolving 3.5 g of hexamethylene tetramine in 500 ml of hydrochloric acid with hydrogen chloride content of 37% and water was added to 1000 ml. After acid cleaning, the bars were cleaned in water, dried and weighed. Cleaning was repeated until there was no change to the weight of bars. Ratio of mass loss to initial mass was calculated. Flexural and compression test were conducted on the prismatic specimens to examine the influence of corrosion inhibitors to strength of AAS.

4.4 Results and discussion

4.4.1 Significance of experimental factors

Applying ANOVA, significance of both factors and their interaction to 28-day flexural strength, 28-day compressive strength, 90-day charge passed, initial setting time, final setting time and 112-day drying shrinkage of AAS is analyzed (Table 4.3 - Table 4.8).

Variation of experimental results is caused by both variation of experimental factors and random errors. *F*-value, i.e. ratio of mean square of experimental factors to random errors, can reflect proportion of the former in total variation. The higher *F*-value is, the more that factor contributes to experimental results. Alkali content produces the most significant effect in all six groups of experimental results. This is followed by modulus of sodium silicate. Interaction between alkali content and modulus plays "very significant" effect on 28-day compressive strength, initial and final setting time, and 112-day drying shrinkage.

Table 4.3 ANOVA on 28-day flexural strength of AAS

Variance source	Sum of squares	Degree of freedom	Mean square	*F*-value	$F_{0.05}$	$F_{0.01}$	Results
Alkali content	30.17	4	7.54	27.84	2.69	4.02	Very significant
Modulus	11.46	2	5.73	21.15	3.32	5.39	Very significant
Interaction	2.93	8	0.37	1.35	2.27	3.17	Not significant
Error	1.34	30	0.04	-	-	-	-
Total	45.90	44	-	-	-	-	-

Table 4.4 ANOVA on 28-day compressive strength of AAS

Variance source	Sum of squares	Degree of freedom	Mean square	*F*-value	$F_{0.05}$	$F_{0.01}$	Results
Alkali content	29035	4	7258.8	1368.4	2.5	3.58	Very significant
Modulus	2703	2	1351.4	254.8	3.12	4.91	Very significant
Interaction	659	8	82.4	15.5	2.07	2.76	Very significant
Error	398	75	5.3	-	-	-	-
Total	32795	89	-	-	-	-	-

Table 4.5 ANOVA on 90-day charge passed of AAS

Variance source	Sum of squares	Degree of freedom	Mean square	*F*-value	$F_{0.05}$	$F_{0.01}$	Results
Alkali content	6.26×10^{6}	4	1.57×10^{6}	298.77	2.69	4.02	Very significant
Modulus	1.13×10^{5}	2	5.67×10^{4}	10.83	3.32	5.39	Very significant
Interaction	7.02×10^{4}	8	8.77×10^{3}	1.67	2.27	3.17	Not significant
Error	1.57×10^{5}	30	5.24×10^{3}	-	-	-	-
Total	6.60×10^{6}	44	-	-	-	-	-

Table 4.6 ANOVA on initial setting time of AAS

Variance source	Sum of squares	Degree of freedom	Mean square	*F*-value	$F_{0.05}$	$F_{0.01}$	Results
Alkali content	831.25	4	207.81	980.43	2.69	4.02	Very significant
Modulus	239.37	2	119.68	564.65	3.32	5.39	Very significant
Interaction	212.82	8	26.60	125.50	2.27	3.17	Very significant
Error	6.36	30	0.21	-	-	-	-
Total	1289.79	44	-	-	-	-	-

Table 4.7 ANOVA on final setting time of AAS

Variance source	Sum of squares	Degree of freedom	Mean square	F-value	$F_{0.05}$	$F_{0.01}$	Results
Alkali content	1235.88	4	308.97	857.99	2.69	4.02	Very significant
Modulus	319.20	2	159.60	443.20	3.32	5.39	Very significant
Interaction	179.75	8	22.47	62.39	2.27	3.17	Very significant
Error	10.80	30	0.36	-	-	-	-
Total	1745.63	44	-	-	-	-	-

Table 4.8 ANOVA on 112-day dry shrinkage of AAS

Variance source	Sum of squares	Degree of freedom	Mean square	F-value	$F_{0.05}$	$F_{0.01}$	Results
Alkali content	2.50×10^{-5}	4	6.26×10^{-6}	3578.95	2.58	3.77	Very significant
Modulus	3.25×10^{-6}	2	1.63×10^{-6}	929.37	3.21	5.11	Very significant
Interaction	1.03×10^{-6}	8	1.28×10^{-7}	73.27	2.16	2.94	Very significant
Error	7.87×10^{-8}	45	1.75×10^{-9}	-	-	-	-
Total	2.94×10^{-5}	59	-	-	-	-	-

4.4.2 Mathematical models for description of strength, drying shrinkage, setting time and charge passed of AAS

Relationships between the significant factors, such as alkali content (X), modulus (Y) and interaction (XY), and 28-day flexural strength (f_f), 28-day compressive strength (f_c), 90-day charge passed (Q), initial setting time (T_i), final setting time (T_f), and 112-day drying shrinkage (S) of AAS are given in Equations (4.17) - (4.22). The fitting models show good agreement with the experimental results (Figure 4.4 - Figure 4.9).

$$f_f = \begin{cases} -96.8X^2+224.7X-1.745Y^2+0.654Y+4.4 & (2\%\leq X<3\%) \\ 405X^2-103X+2.09Y^2-5.93Y+16.4 & (3\%\leq X\leq 6\%) \end{cases} \tag{4.17}$$

$$f_c = -17714X^2+2161X+561XY-13Y^2+23.4Y-19.8 \tag{4.18}$$

$$Q = 304976X^2+1610X-775Y^2+1240Y-80 \tag{4.19}$$

$$T_\mathrm{i} = 11567X^2-1701.5X+564XY+4.5Y^2-40Y+63.4 \tag{4.20}$$

$$T_\mathrm{f} = 12436X^2-1802X+520XY+0.76Y^2-33Y+66.1 \tag{4.21}$$

$$S = 0.538X^2+0.0307X-0.033XY-0.00114Y^2+0.0043Y+0.0001 \tag{4.22}$$

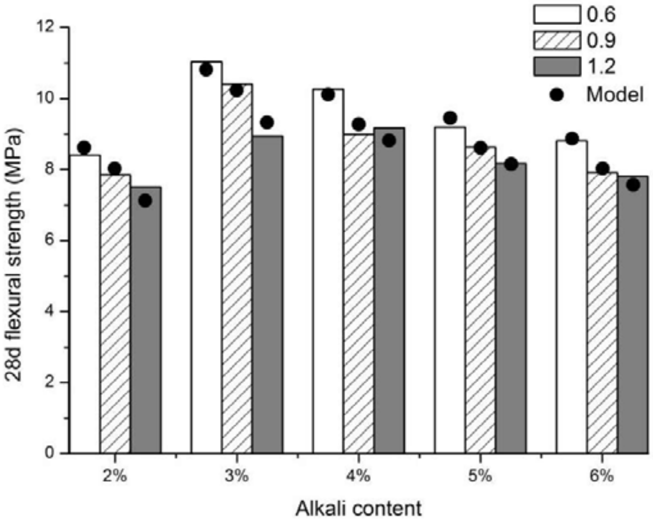

Figure 4.4 Fitted and experimental values of 28-day flexural strength of AAS

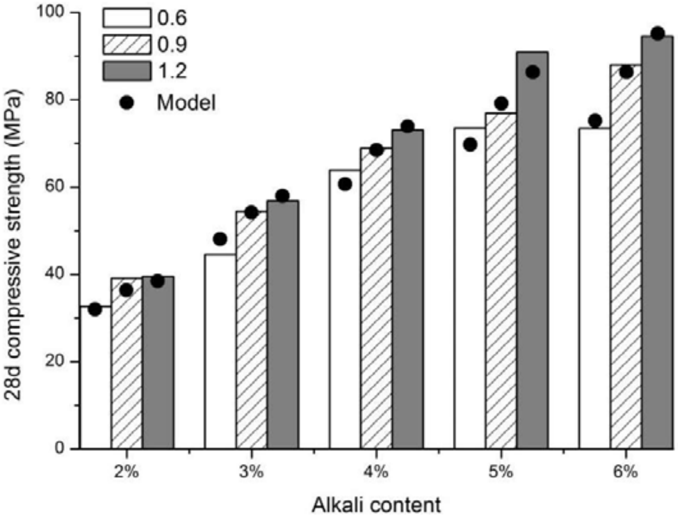

Figure 4.5 Fitted and experimental values of 28-day compressive strength of AAS

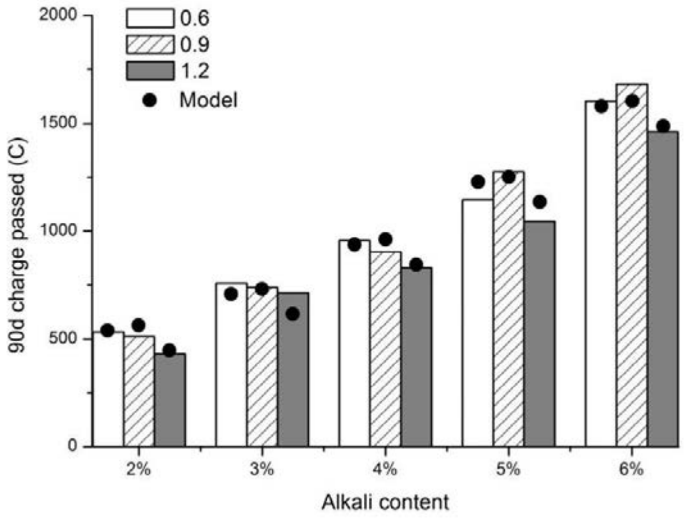

Figure 4.6 Fitted and experimental values of 90-day charge passed of AAS

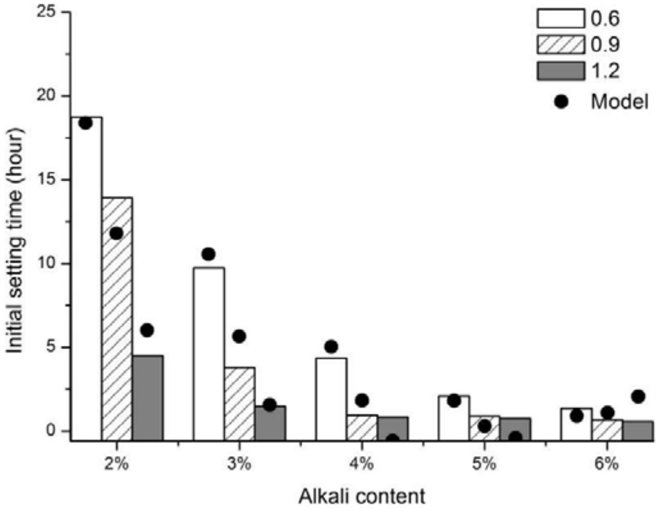

Figure 4.7 Fitted and experimental values of initial setting time of AAS

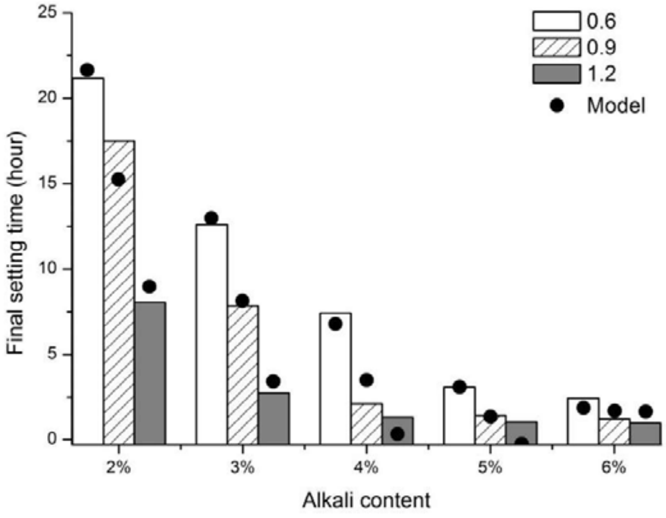

Figure 4.8 Fitted and experimental values of final setting time of AAS

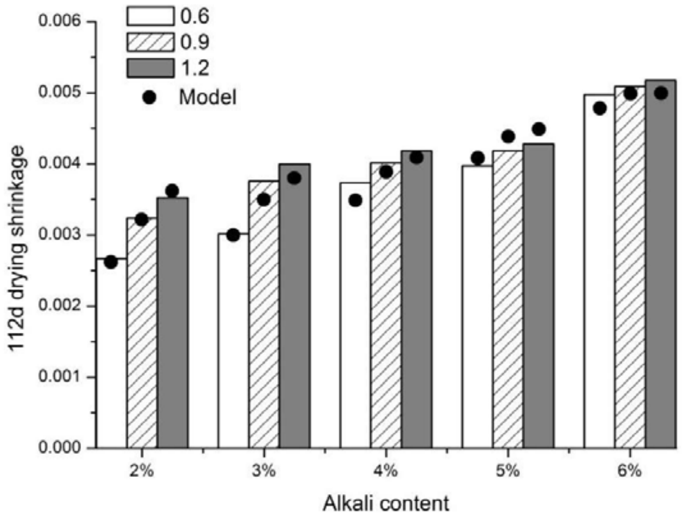

Figure 4.9 Fitted and experimental values of 112-day drying shrinkage of AAS

4.4.3 Optimized mix proportion of AAS

Equation (4.23) gives the comprehensive index I calculated based on the above mathematic models. AAS with alkali content of 3% and modulus of 0.95 scores the highest I-value of 0.445 under available alkali contents and moduli (Figure 4.10). 28-day flexural strength (f_f), 28-day compressive strength (f_c), 90-day charge passed (Q), initial setting time (T_i), final setting time (T_f), and 112-day drying shrinkage (S) of the optimal AAS are given in Table 4.9. The optimal AAS exhibits suitable setting time, higher flexural and compressive strength than OPC and elastic modulus “E” comparable to normal strength concrete.

$$I = \begin{cases} -772.56X^2+85.26X+22.26XY+0.368Y^2-2.143Y-0.299 \ (2\% \leq X < 3\%) \\ -630X^2-7.84X+22.26XY+1.458Y^2-4.014Y+3.11 \ (3\% \leq X \leq 6\%) \end{cases} \tag{4.23}$$

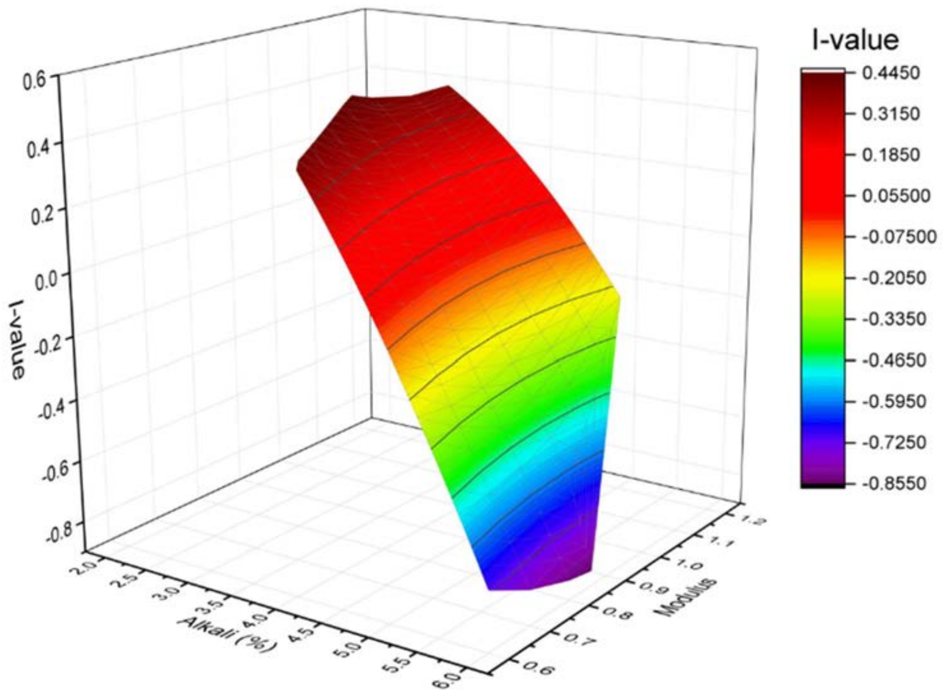

Figure 4.10 Comprehensive index *I* of AAS

Table 4.9 Performance of the optimal AAS

f_f	f_c	Q	T_i	T_f	S	E
10.1 MPa	55.0 MPa	725 C	1.97 h	6.83 h	0.00383	25.9GPa

4.4.4 Protection of AAS and corrosion inhibitors on reinforcements

With increasing polarization time, visible cracks caused by expansive corrosion products appeared on the specimens and developed along main reinforcements. This was followed by transverse cracks resulting from corroded stirrups. Rust exuded from the cracks and contaminated surface of specimens. Specimens varied in the time of cracking, from five to nine days (Table 4.10). AAS specimens showed later time of cracking than OPC one. This is benefited by low chloride penetrability of AAS and stable passive films of reinforcements formed in alkali solution of AAS. Similar phenomenon is also reported by Yu et al. (2015). They found the corrosion resistance of passive film was improved with increasing dosage of sodium hydroxide in simulated pore solution of AAS. Both corrosion inhibitors are effective to postpone corrosion-induced cracks in mortar. Amino alcohol in CCI can be absorbed by reinforcements and form insoluble iron compound to inhibit corrosion. The CCI, however, deteriorated the strength of AAS (Figure 4.11 and Figure 4.12). Surfactants in the CCI can easily generate bubbles during mixing and casting, which affects density and durability of mortar (Figure 4.13). This corrosion inhibitor, therefore, should be used with a matching defoaming agent. $NaNO_2$ is a typical corrosion inhibitor for protecting the anode against corrosion reaction. With increasing dosages of $NaNO_2$, the time when the first crack appeared became increasingly late. Nitrite facilitates positive movement of anode potential and improves passivation of reinforcements by its oxidation to iron (Söylev and Richardson 2008). In this study, $NaNO_2$ supplied more effective protection on reinforcements than CCI without any adverse influence on strength of AAS.

Table 4.10 Time of cracking on specimens (days)

P0	A0	B15	B30	C15	C30
5	7	8	9	7	8

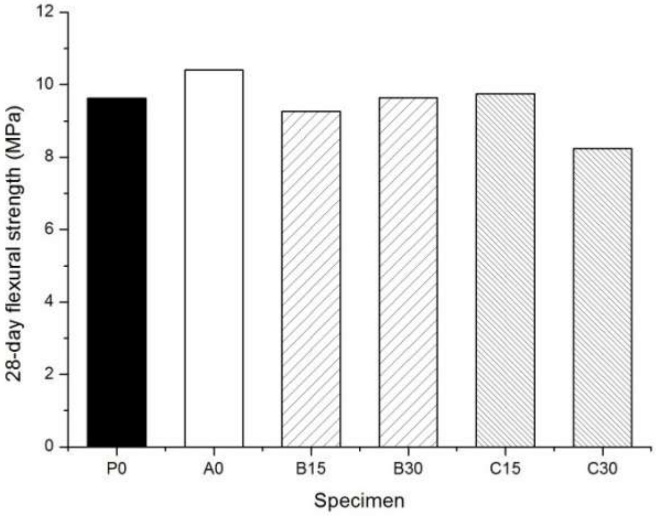

Figure 4.11 28-day flexural strength

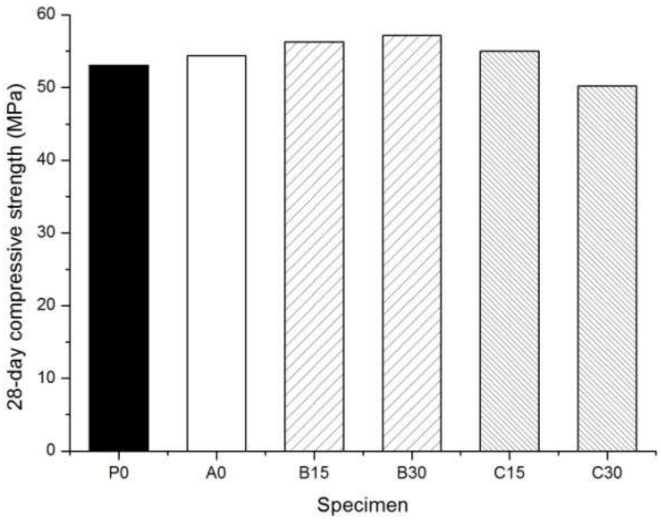

Figure 4.12 28-day compressive strength

Figure 4.13 Pores in AAS mortar mixed with a CCI

In order to simulate actual corroded structures with obvious corrosion-induced cracks and rust, the artificially accelerated corrosion tests were continued after the specimens cracked. The total time of polarization provided reference for the following accelerated corrosion on long column specimens. After polarized for 35 days, all specimens tended to be stable in development of cracks. The actual polarization time was longer than the estimated time of 28 days according to Equation (4.16). Similar phenomenon was also reported by Fang et al. (2004). As shown in Figure 4.14, artificially accelerated corrosion caused obvious longitudinal and transverse cracks and rust stains on the surfaces of specimens. The corrosion product, $Fe(OH)_2$, appeared green when specimens were split and rapidly oxidized to brown $Fe(OH)_3$ after exposed to air for several minutes (Figure 4.15). There was serious pitting corrosion on main reinforcements and stirrups (Figure 4.16 and Figure 4.17). Mass loss ratio of main reinforcements is given in Figure 4.18. OPC specimen suffered the severest corrosion of

9.93% by mass of steel bars. Measured mass loss of reinforcements embedded in AAS was only 64% of that in OPC and is consistent with the finding of Chen (2008). However, the difference in mass loss of reinforcement cannot be entirely ascribed to AAS and corrosion inhibitor. The mortar cover fails to hinder ingress of chloride after it cracks. Saline solution will be in contact with surface of reinforcements directly.

a) P0 b) A0 c) B15

d) B30 e) C15 f) C30

Figure 4.14 Specimens after accelerated corrosion

Figure 4.15 Colour change of corrosion product

Figure 4.16 Corroded main reinforcement

Figure 4.17 Corroded stirrup

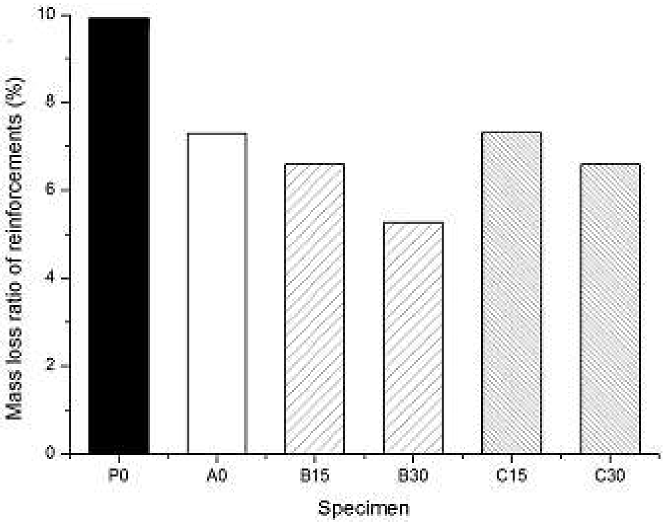

Figure 4.18 Mass loss ratio of main reinforcements

4.5 Summary

In this chapter, significance of experimental factors including alkali content, modulus and their interactions was analyzed. Relationships between the significant factors and experimental responses of AAS were modeled and in good agreement with test results. Mix proportion of AAS mortar was optimized based on comprehensive evaluation on strength, durability and setting time. Protection offered to reinforcements by the optimal AAS with corrosion inhibitors was examined by performing an accelerated corrosion test on column specimens. Primary summaries are drawn as follows.

1. Alkali content is the most significant factor and this is followed by modulus of sodium silicate. Interaction between alkali content and modulus exerts “very significant” influence on 28-day compressive strength, initial and final setting time, and 112-day drying shrinkage only.

2. AAS, especially AAS mixed with corrosion inhibitor can postpone the time of cracking induced by corrosion of reinforcements. The CCI used in this study exerts negative effect on strength of AAS. $NaNO_2$ with dosage of 3% by mass of GGBFS keeps good compatibility with AAS.

3. The optimized AAS comprises GGBFS activated by sodium silicate solution at alkali

content of 3%, modulus of 0.95 and $NaNO_2$ dosage of 3%. It will be employed as the mix proportion of AAS in Chapters 5-7 on the study of fibers reinforced AAS, AAS ferrocement, and strengthening corroded concrete columns.

CHAPTER 5

PERFORMANCE OF FIBERS REINFORCED AAS AND AAS FERROCEMENT

5.1 Introduction

Mix proportion of AAS optimized in Chapter 4 exhibits high strength, low permeability, appropriate setting time and excellent protection on reinforcements. AAS activated by silicate, however, has larger drying shrinkage than OPC due to dehydration of silicate gels during hardening. Intense drying shrinkage may result in micro cracks in paste, which weakens tensile performance of AAS. Experimental results in Chapter 4 have shown that flexural strength is far below compressive strength of AAS. Moreover, AAS specimens may fracture suddenly at flexural capacity, which shows obvious brittleness. As a strengthening material, AAS should possess outstanding performance including tensile strength and ductility. Numerous studies have shown that addition of fibers or meshes can efficiently reduce shrinkage and enhance tensile performance of mortar (Araya-Letelier et al. 2017; Bernal et al. 2010; Mustea and Manea 2017; Shah and Naaman 1976). In this chapter, fibers and steel meshes were used to reinforce AAS. Effect of reinforcement was assessed by three-point flexural tests. An AAS composite was selected based on ductility and flexural capacity. It was used to confine square concrete columns. Tensile strength of the AAS composite and its confinement on concrete columns were examined and modeled.

5.2 Flexural test on fibers reinforced AAS and AAS ferrocement

5.2.1 Materials

Mix proportion of AAS optimized in Section 4.4.3 was employed as rendering material in this chapter. Galvanized steel wire mesh ("GSWM"), SSWM, steel fibers with hooks, and aramid fibers were used to reinforce AAS mortar (Figure 5.1). Material properties of the meshes and fibers are given in Table 5.1. Two dosages of aramid fibers, SSWM and GSWM were used (Table 5.2). In the trial mix, steel fibers with dosage of 1.5% by volume of mortar clumped and failed to disperse. Therefore, dosage of 1.5% by volume was not considered for steel fibers. SSWM and GSWM were used to reinforce tensile region of AAS mortar under flexure. Their dosages were approximately half of that using aramid fibers. SSWM and GSWM were cut into slices with dimension of 160×40 mm (Figure 5.2).

a. Steel fibers b. Aramid fibers

Figure 5.1 Steel fibers and aramid fibers

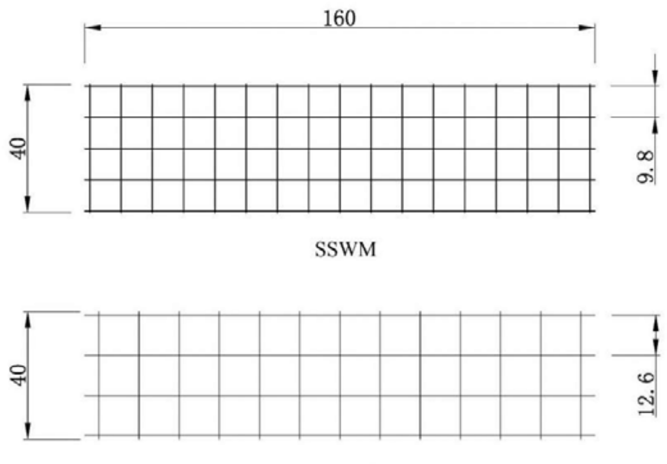

Figure 5.2 Schematic view of SSWM and GSWM (unit: mm)

Table 5.1 Material properties of meshes and fibers

	Diameter (mm)	Grid size / Fiber length (mm)	Elastic modulus (GPa)	Tensile strength (MPa)
GSWM	0.7	12.6	200	350
SSWM	0.9	9.8	194	350
Steel fiber	0.9	60	210	2300
Aramid fiber	0.12	20	73	3400

Table 5.2 Dosage of fibers or meshes in AAS mortar

Group	Fiber / mesh type	Dosage (by volume of mortar)
AF075	Aramid fiber	0.75%
AF150		1.50%
SF075	Steel fiber	0.75%
SSWM1	SSWM	0.37% (1 layer)
SSWM2		0.74% (2 layers)
GSWM2	GSWM	0.35% (2 layers)
GSWM4		0.70% (4 layers)

5.2.2 Specimens and test setup

As shown in Table 5.2, there are seven groups of specimens. In each group, three prismatic specimens (40×40×160 mm) were prepared for flexural test. Procedure of preparation of AAS mortar is same with that presented in Section 3.2.2. For fibers reinforced mortar, fibers were added into fresh AAS mortar and mixed for two additional minutes. For ferrocement, meshes were fixed in moulds by two wooden chips before mortar casting. Average distance from mesh to side of the mould was 6.7 mm. Meshes located on the centroid of triangular tensile stress distribution induced by flexure (Figure 5.3). Mortar was cast into moulds and compacted using a vibrating table. The specimens were removed from moulds 24 hours after casting and cured in water at 27^0C for 28 days.

Three-point flexural tests were conducted on prismatic specimens at 28 days. Loading rate was 0.3 mm/min. Load and deflection at middle span of specimens were recorded.

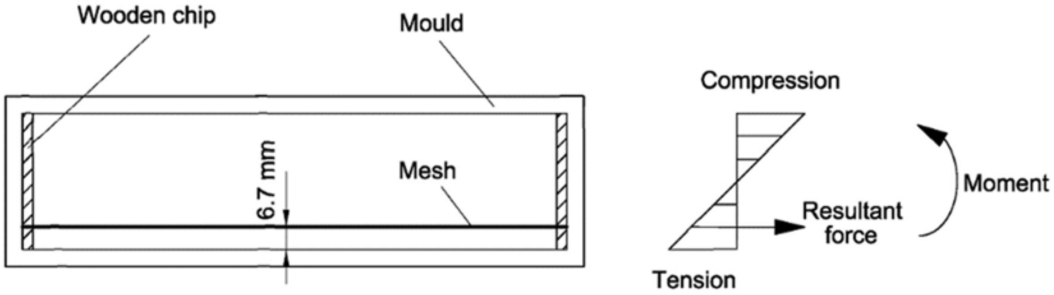

Figure 5.3 Fixation of meshes in moulds

5.2.3 Results and discussion

Failure modes of specimens are given in Figure 5.4. Specimens with two layers of SSWM experienced a mixed flexural-shear failure (Figure 5.4 (g)). The rest of specimens failed due to flexural failure (Figure 5.4 (a) - (f)). Steel fibers reinforced specimen had failure mode similar to aramid fibers reinforced ones. With increasing loading, one crack formed at bottom of specimens and extended upward. Fibers were pulled out from mortar. Due to strong anchorage of hooks, steel fibers split surrounding mortar, while aramid fibers were pulled out without damaging the mortar (Figure 5.4 (a) – (c)). Pattern of cracks in specimens with GSWM was similar to that in aramid fibers reinforced specimens. The GSWM, however, fractured successively once their tensile limit was reached, which resulted in brittle failure. Moreover, zinc coating of GSWM reacted with hydroxide in AAS (Equation (5.1)). The reaction product, hydrogen, resulted in large quantities of pore in mortar, which reduced strength of mortar (Figure 5.4 (d), (e)).

$$\mathrm{Zn} + 2\mathrm{OH}^{-} = \mathrm{ZnO}_2^{2-} + \mathrm{H}_2\uparrow \qquad (5.1)$$

Specimens with SSWM exhibited better ductility than the other specimens owing to large elongation of SSWM. Intensive cracks were distributed in middle span of specimens. When dosage of SSWM was increased to two layers, failure mode of specimens changed from flexural failure to a mixed flexural-shear failure. The specimens failed with fully developed diagonal cracks between loading point and support (Figure 5.4 (g)).

a. SF075

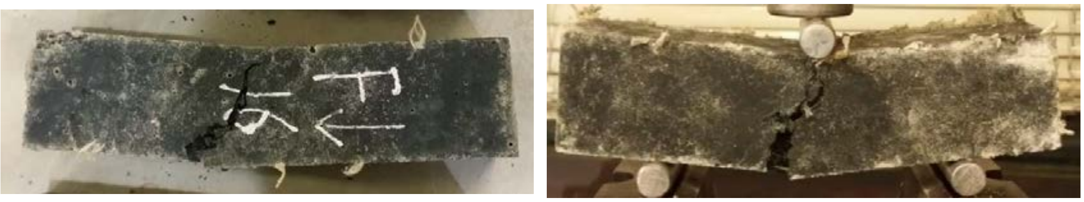

b. AF075 c. AF150

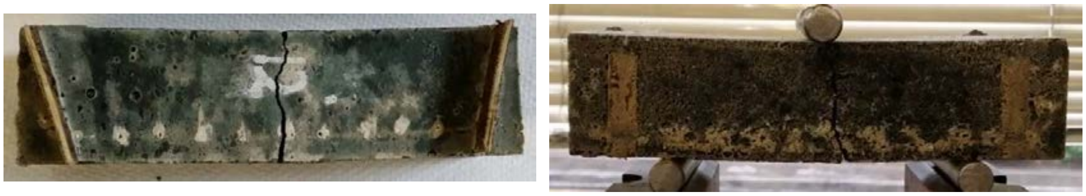

d. GSWM2 e. GSWM4

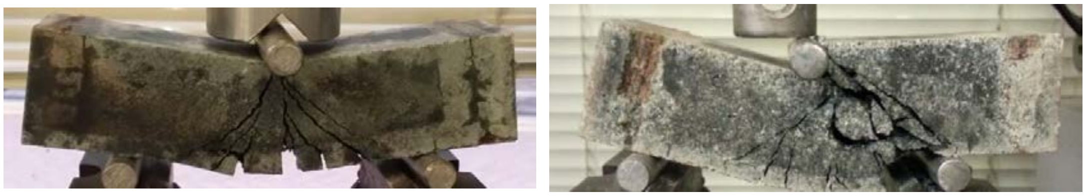

f. SSWM1 g. SSWM2

Figure 5.4 Failure modes of fibers reinforced AAS and AAS ferrocement

Load-deflection relationships of specimens reinforced by aramid fibers, steel fibers, SSWM, and GSWM are given in Figure 5.5 to Figure 5.8. Specimens with large dosage of fibers and meshes achieved approximately double peak load and deformation than the ones with small dosage. Loading capacity of steel and aramid fibers reinforced specimens gradually declined in post-peak stage, while that of GSWM ferrocement dropped sharply due to fracture of GSWM. Specimens with one layer of SSWM exhibited excellent ductility and increasing strength after yielding. Ferrocement with two layers of SSWM did not exhibit full potential owing to shear failure of mortar.

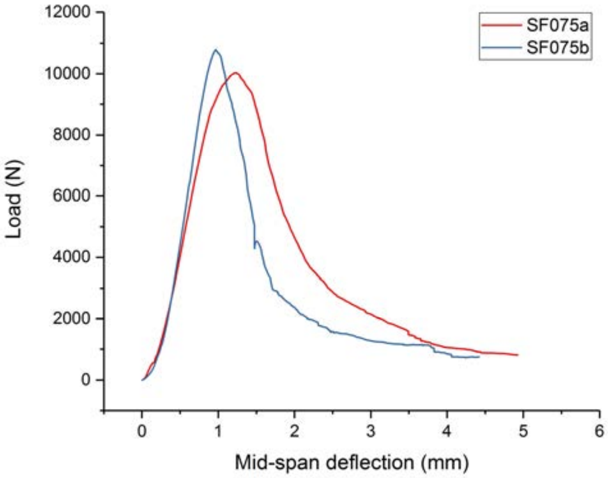

Figure 5.5 Load-deflection relationship of steel fibers reinforced mortar

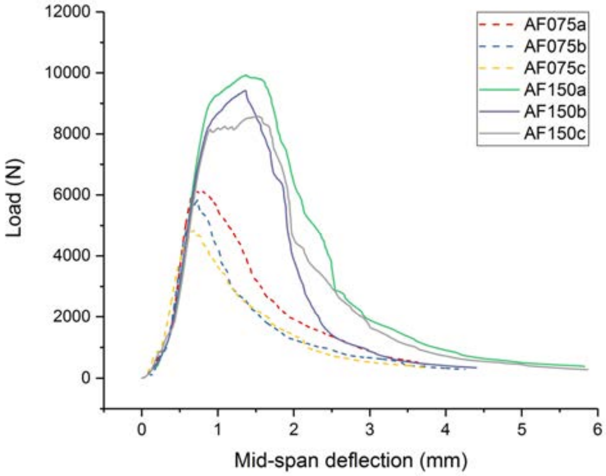

Figure 5.6 Load-deflection relationship of aramid fibers reinforced mortar

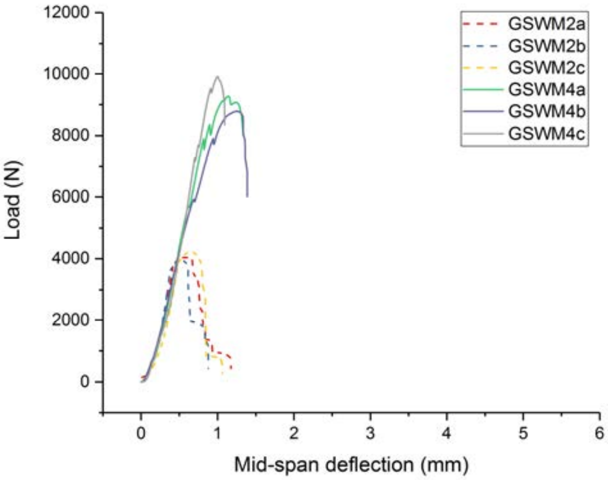

Figure 5.7 Load-deflection relationship of GSWM ferrocement

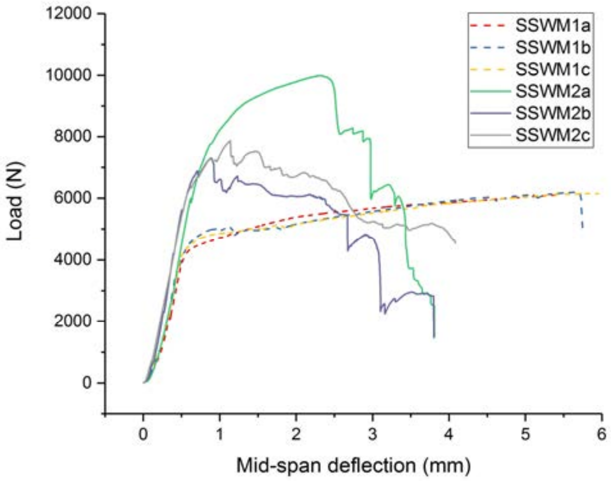

Figure 5.8 Load-deflection relationship of SSWM ferrocement

Peak loads of specimens reinforced by various fibers and meshes and control ones are given in Table 5.3. Most specimens displayed higher flexural capacity than control ones except ferrocement with one layer of GSWM. Hydrogen generated in the reaction between zinc coating and alkali reduces tensile strength of AAS mortar. Steel fibers reinforced specimens achieve peak load comparable to the ones reinforced by high dosage of aramid fibers, GSWM and SSWM. Because of relatively long length and restraint by moulds, steel fibers align parallel to direction of tensile stress, which contributes to flexural capacity of specimens. Moreover, hooks at ends of steel fibers improve anchorage and contribute to tensile strength of fibers. Nevertheless, high density of steel fibers leads to sedimentation of fibers in AAS mortar. Uneven distribution of fibers may result in defects in fibers reinforced mortar. Compared to aramid fibers and GSWM, SSWM has better elongation and compatibility with AAS. SSWM ferrocement shows good flexural capacity and ductility and is thus employed to confine concrete columns.

Table 5.3 Peak load of specimens reinforced by various fibers and meshes

Specimen	Peak load (N)	Average (N)	Enhancement
Control	4127	4310	-
	4497		
	4306		
AF075	6158	5618	30.4%
	5839		
	4858		
AF150	9924	9306	115.9%
	9419		
	8574		
SF075	10029	10410	141.5%
	10791		
SSWM1	6108	6152	42.7%
	6193		
	6156		
SSWM2	9989	8386	94.6%
	7296		
	7874		
GSWM2	4048	4076	-5.4%
	3956		
	4225		
GSWM4	9279	9327	116.4%
	8784		
	9918		

5.3 Tensile behavior of AAS ferrocement

5.3.1 Materials and specimens

AAS ferrocement exhibits superior strength and ductility. It can be used to provide confinement to concrete columns. Effectiveness of confinement is strongly linked to lateral pressure to core concrete which depends on tensile performance of AAS ferrocement (Mander et al. 1988). In order to quantify the confinement of concrete, tensile performance of AAS ferrocement with various layers of SSWM were tested by direct tensile tests in this section. Five groups of specimens, including mortar, mesh, ferrocement with one, two and four layers of SSWM, were prepared. There were three specimens in each group. Dimensions of specimens are given in Table 5.4. SSWM was fixed on the middle plane of ferrocement specimens by steel mould during casting. In order to prevent local failure, additional meshes were used to reinforce ends of ferrocement specimens. For mesh specimens, SSWM was embedded in epoxy resin at each end to facilitate clamping the SSWM in fixture (Figure 5.9). The specimens were demoulded 24 hours after casting and then covered by polyethylene film.

Table 5.4 Dimensions of specimens

Material	ID of specimens	Width (mm)	Thickness (mm)	Layers of SSWM
Mortar specimen	01	75.0	17.5	0
	02	75.0	17.0	
	03	75.0	17.2	
Mesh specimen	SSWM1	75.0	-	1
	SSWM2	75.0		
	SSWM3	75.0		
Ferrocement specimen	11	74.0	19.2	1
	12	75.3	18.5	
	13	75.5	18.5	
	21	74.5	17.3	2
	22	74.6	17.8	
	23	75.7	16.5	
	41	75.5	18.0	4
	42	76.3	17.6	
	43	77.4	18.7	

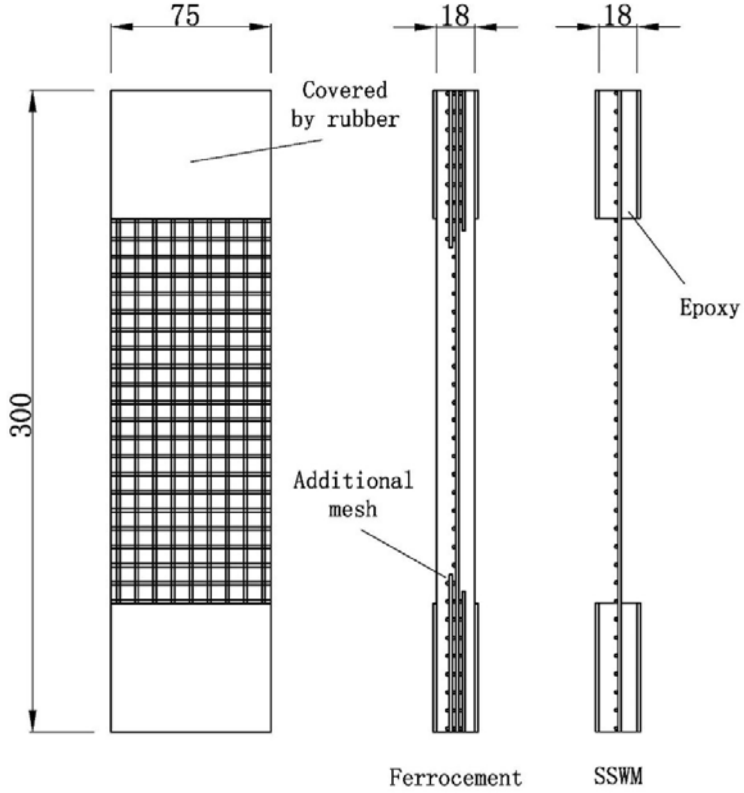

Figure 5.9 Schematic view of AAS ferrocement and SSWM specimens (unit: mm)

5.3.2 Test setup

Direct tensile tests were conducted on mortar and ferrocement specimens at 7 days. Rubber was pasted on the ends of ferrocement specimens to improve friction between fixture and specimens (Figure 5.9). Ends of fixtures were connected to universal joints to eliminate eccentricity. Axial load, with loading rates of 3 kN/min in elastic stage and 3.5 mm/min after specimens yielded, was applied to the specimens. Axial deformation of specimen was measured by one pair of LVDTs with gauge length of 120 mm. Epoxy-based adhesive was used to glue aluminum sheets with mesh specimens (Figure 5.10). Stress-strain relationship of stainless steel wire was also assessed experimentally.

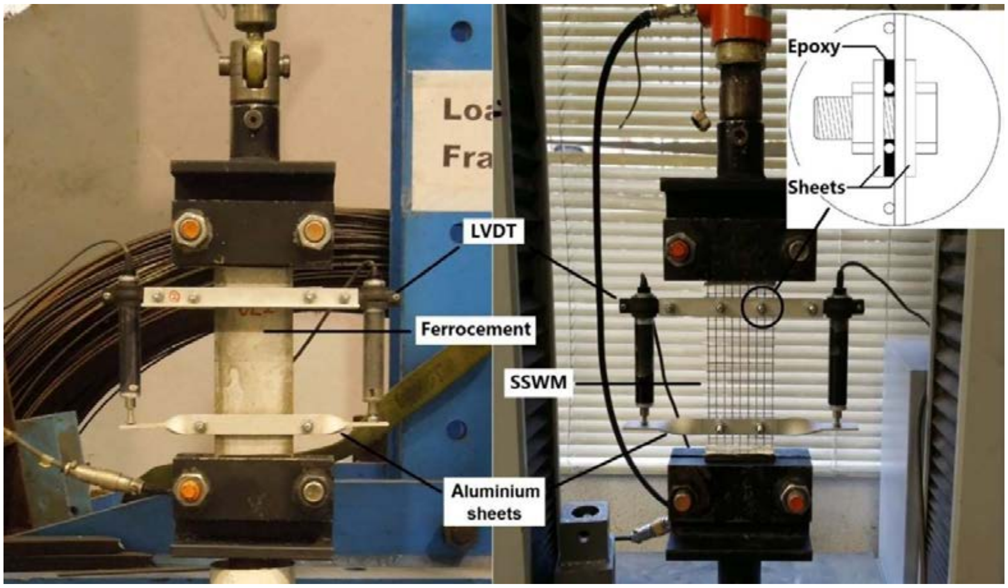

Figure 5.10 Direct tensile test

5.3.3 Results and discussion

Failure modes of AAS ferrocement specimens are given in Figure 5.11. Mortar specimens fractured suddenly once the first transverse crack formed (Figure 5.11(a)). Different from mortar specimens, ferrocement ones were able to resist tension after cracking and cracks were continuously formed with increasing loading. The more SSWM there were, the denser the cracks were. After ferrocement specimens reached their yield load, there was no further increase in number of cracks. Instead, the existing cracks widened, accompanied by chipping and spalling of mortar. Specimens with one and two layers of SSWM lost their loading capacities due to tensile failure of SSWM, while specimens with four layers of SSWM failed due to slippage of specimens out of the fixtures (Figure 5.11(b), (c), (d)). For mesh specimens, one wire fractured at welding point, which led to deterioration in tensile capacity (Figure 5.12). Both ferrocement and mesh specimens failed due to fracture of steel wire at welding point. It is because the meshes were made of steel wires welded to each other using pressure welding. The wires have smaller cross-sectional area at welding point and are thus easy to fracture under tension over there.

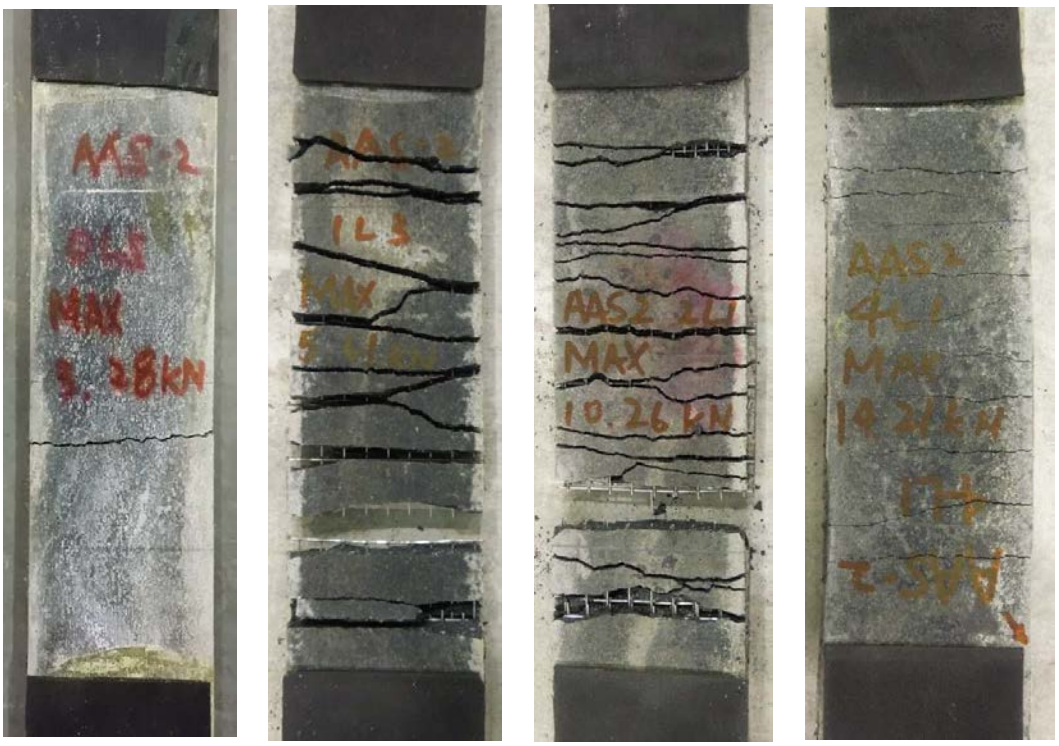

a. Mortar
b. AAS with one layer of SSWM
c. AAS with two layers of SSWM
d. AAS with four layers of SSWM

Figure 5.11 Failure modes of specimens with various layers of SSWM

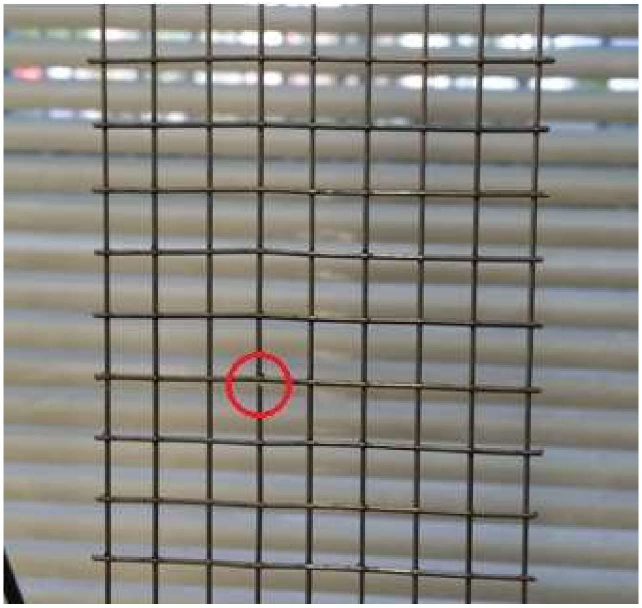

Figure 5.12 Failure modes of mesh specimen

Stress-strain relationship of stainless steel wire is given in Figure 5.13. Yield strength of stainless steel wire, at plastic strain of 0.2%, was 348 MPa. Axial load-deformation relationships of specimens are given in Figure 5.14. Load-deformation curves of ferrocement are consisted of two stages. The first stage is approximately linear and ceases when mortar cracked. Compared to mesh specimens, ferrocement with one layer of SSWM has higher strength at end of linear stage with contribution of AAS mortar. As the first crack appears in mortar, meshes begin to carry all the tensile load. With increasing displacement, loading capacity of mesh specimens approaches that of ferrocement specimens. However, distribution of tensile stress in ferrocement specimen is different from that in mesh specimen. After ferrocement cracks, tensile stress is only carried by mesh at cracks, while by both mortar and mesh at the section away from cracks. The mesh in ferrocement reaches its maximum stress only at cracks of ferrocement. On the contrary, the mesh specimen reaches its maximum stress along its full length under tension. All the welding points of mesh specimen carry the maximum stress. The mesh specimen has higher probability to fail at the welding points than the ferrocement with one layer of mesh. This explains the phenomenon that the ferrocement specimens with one layer of mesh had higher peak load than the mesh specimens.

SSWM dramatically improves performance of AAS mortar after cracking. Besides ductility, obvious enhancement was observed at both cracking load and peak load of ferrocement with increasing layers of SSWM (Table 5.5). Cracking load is defined as the tensile load at first crack. One layer of SSWM slightly increases cracking load by 28%, while two and four layers of SSWM result in double and four times improvement in cracking load. Benefited by strain-hardening behavior of stainless steel wire, ferrocement specimens display growing strength after yielding. Loading capacities of ferrocement with one and two layers of SSWM are improved by 35% and 37% after the first crack appears, respectively.

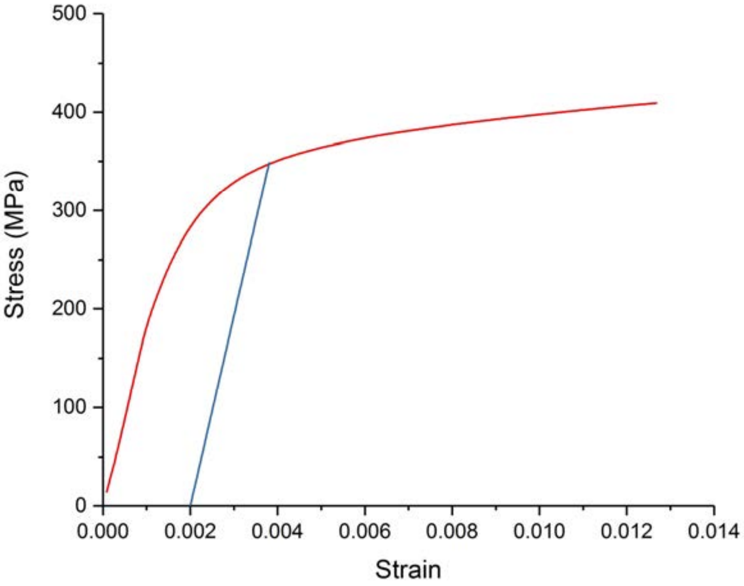

Figure 5.13 Stress-strain relationship of stainless steel wire

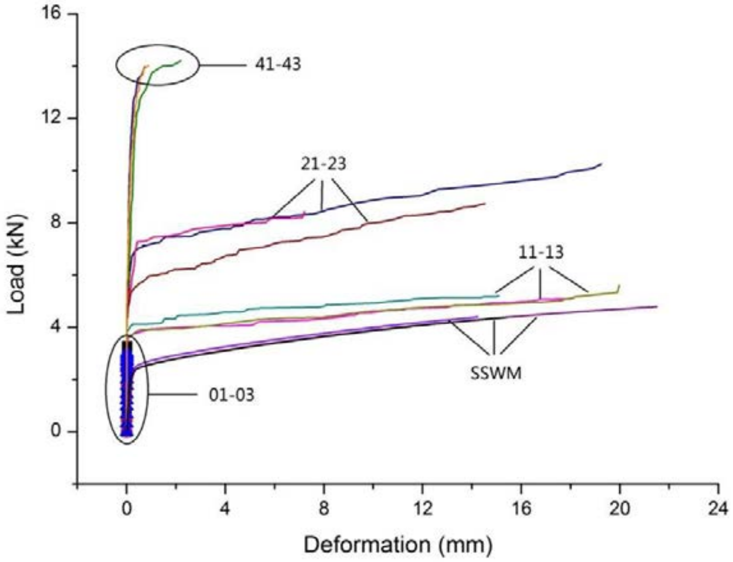

Figure 5.14 Axial load-deformation relationships of AAS ferrocement and SSWM

Table 5.5 Tensile capacity of AAS ferrocement

ID of specimens	Layers of SSWM	Cracking load (kN)	Average (kN)	Peak load (kN)	Average (kN)
01	0	3.28	3.07	-	-
02		2.89		-	
03		3.03		-	
11	1	4.12	3.94	5.20	5.33
12		3.81		5.17	
13		3.88		5.61	
21	2	7.01	6.65	10.26	9.14

22		5.66		8.74	
23		7.27		8.43	
41	4	12.33	12.95	14.21	14.07
42		13.51		13.99	
43		13.01		14.02	

Table 5.6 Tensile capacity of mesh specimens

ID of specimens	Layers of SSWM	Yield load (kN)	Average (kN)	Peak load (kN)	Average (kN)
SSWM1	1	2.45	2.48	4.80	4.53
SSWM2		2.55		4.41	
SSWM3		2.43		4.39	

Cracking load of ferrocement is associated with tensile strength of both mortar and mesh, while peak load of ferrocement depends on mesh only (ACI 549R-97). Cracking load (“$P_{\mathrm{cr,f}}$”) and peak load (“$P_{\mathrm{p,f}}$”) of AAS ferrocement in tension can be predicted by following equations.

$$P_{\mathrm{cr,f}} = f_{\mathrm{t,m}} A_{\mathrm{m}} + \sigma_{\mathrm{s}} A_{\mathrm{ss}} \tag{5.2}$$

$$P_{\mathrm{p,f}} = f_{\mathrm{u}} A_{\mathrm{ss}} \tag{5.3}$$

where $f_{\mathrm{t,m}}$ is tensile strength of mortar, which can be obtained by cracking load divided by cross-section area of mortar. σ_{s} is stress of wire corresponding to first crack in ferrocement, which is close to yield stress of wire (Kameswara Rao and Kamasundara Rao 1994). A_{m} and A_{ss} are cross-section area of mortar and SSWM, respectively. f_{u} is ultimate strength of wire. Equations (5.2) and (5.3) can also be expressed as follows.

$$P_{\mathrm{cr,f}} = f_{\mathrm{t,m}} A_{\mathrm{m}} + nP_{\mathrm{y,ss}} \tag{5.4}$$

$$P_{\mathrm{p,f}} = nP_{\mathrm{p,ss}} \tag{5.5}$$

where n is layers of SSWM. $P_{\mathrm{y,ss}}$ and $P_{\mathrm{p,ss}}$ are yield load and peak load of SSWM given in Table 5.6, respectively.

Applying Equations (5.4) and (5.5), $P_{\mathrm{cr,f}}$ and $P_{\mathrm{p,f}}$ of AAS ferrocement are calculated and given in Table 5.7. It can be seen that predicted cracking load is slightly overestimated for specimens with one layer of SSWM, while in good agreement for specimens with two and four layers of SSWM. Predicted peak load is close to tested value except the specimens strengthened with four layers of SSWM due to premature slippage of specimens from fixtures.

Table 5.7 Prediction of tensile capacity of AAS ferrocement

ID of specimens	Layers of SSWM	Cracking load (kN)		Peak load (kN)	
		Test values	Prediction	Test values	Prediction
11	1	4.12	5.66	5.20	4.53
12		3.81	5.59	5.17	
13		3.88	5.60	5.61	
21	2	7.01	7.64	10.26	9.07
22		5.66	7.73	8.74	
23		7.27	7.54	8.43	
41	4	12.33	12.38	14.21	18.13
42		13.51	12.33	13.99	
43		13.01	12.57	14.02	

5.4 Confinement of AAS ferrocement to concrete columns

This section aims to investigate confinement of AAS ferrocement to concrete columns. Axial compressive tests were conducted on square concrete columns wrapped by ferrocement laminates. Loading capacity and ductility of specimens under compression were compared.

5.4.1 Materials and specimens

To simulate the concrete of aged buildings, two batches of concrete with water-cement ratio of 0.75 were used. Their 28-day compressive strength (“f_{cu}”) estimated by 100mm cubes were 31.5 and 29.7 MPa, respectively. Mix proportion of concrete is given in Table 5.8. Eight square plain concrete columns were prepared. The column specimens had cross section of 200 mm × 200 mm and height of 600 mm. They were cured in air for 28 days after demoulding.

Table 5.8 Mix proportion of concrete (kg/m^3)

Water	210
Cement	280
Coarse aggregate (10mm)	395
Coarse aggregate (20mm)	790
Sand	705

Table 5.9 Details of specimens

Specimen	f_{cu} (MPa)	Strengthening materials
Control A	31.5	-
Control B	29.7	
0L A	31.5	AAS mortar
0L B	29.7	
1L A	31.5	AAS ferrocement with one layer of SSWM
1L B	29.7	
2L A	31.5	AAS ferrocement with two layers of SSWM
2L B	29.7	

Eight column specimens were divided into four groups, namely control, 0L, 1L and 2L. There were two specimens in each group. Specimens in groups 0L, 1L and 2L were strengthened by AAS mortar and ferrocement with one and two layers of SSWM, respectively (Table 5.9). Procedure of strengthening works is as follows: 1. Corners of column specimens were rounded by a polisher. Surface of columns was first chiseled by an impact hammer until coarse aggregates were exposed and then cleaned by compressed air; 2. Specimens of groups 1L and 2L were wrapped by one and two layers of SSWM, respectively (Figure 5.15); 3. The surface of specimens was dampened. Specimens were placed in wooden formwork. An expanded polystyrene cap was placed on bottom of specimens to prevent ferrocement from direct compression; 4. AAS mortar was cast into the gap between formwork and specimen (Figure 5.16). The mortar was compacted by hammering the formwork. Thickness of ferrocement jacket was 11 mm; 5.

The formwork was dismantled 24 hours after casting. Surface of ferrocement jacket was moistened and protected by polyethylene film (Figure 5.17).

Figure 5.15 Wrapping specimens with SSWM

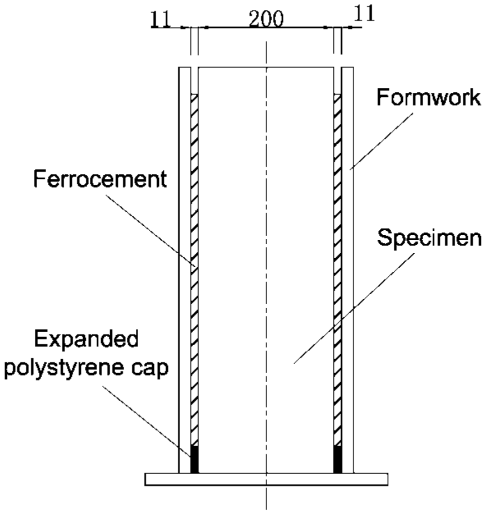

Figure 5.16 Sectional drawing of strengthened specimen (unit: mm)

Figure 5.17 Curing ferrocement jackets

5.4.2 Test setup

Compressive tests were conducted on column specimens seven days after casting AAS mortar. Both end faces of the specimens were capped by gypsum. Monotonic axial compression was applied by loading rate of 0.2 mm/min. Tests were terminated when load declined to 85% of its peak. A pair of LVDTs was used to measure axial deformation of specimens (Figure 5.18).

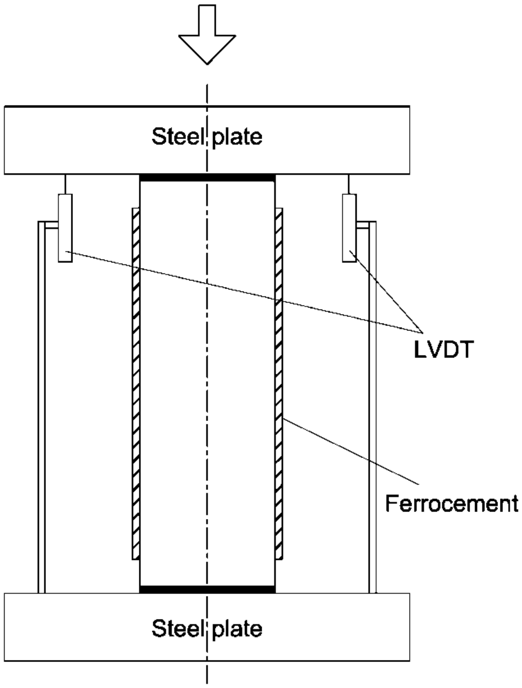

Figure 5.18 Schematic view of compressive test on plain concrete column

5.4.3 Results and discussion

Failure modes of specimens are given in Figure 5.19 (a) - (d). Control specimen did not crack until axial load approached peak value. With increasing displacement, short longitudinal cracks appeared and developed in lower part of control specimen. At post-peak stage, longitudinal cracks connected to each other accompanied by spalling of concrete chips (Figure 5.19 (a)). The first crack in specimen 0L B was observed in corner of mortar jacket. Subsequently, the cracks widened and new cracks appeared in middle of specimen. The cracks were fully developed with increasing displacement. Mortar jacket in the corners lost bonding with core concrete and spalled at end of test

(Figure 5.19 (b)). Figure 5.19 (c) shows the crack pattern of specimen 1L B. Similar to specimen 0L B, specimen 1L B first cracked at a corner of ferrocement jacket. With progressive increase in axial displacement, number of cracks in the jacket increased. Cracks in specimen 1L B were finer and denser than those in specimen 0L B. Cracks of specimen 2L B were mainly distributed in corners of ferrocement jacket (Figure 5.19 (d)). Longitudinal cracks started to generate in middle of the jacket when axial load declined to 95% of its peak value. Specimens with one and two layers of SSWM lost their loading capacity owing to tensile failure of ferrocement jacket. Spalled cover at corners of specimen 2L B was removed after test. SSWM was found to fail due to tensile failure (Figure 5.20). All the strengthened specimens first cracked in corners of jackets, which was attributed to stress concentration (Kaish et al. 2012). The cracks propagated longitudinally in mortar jacket and ferrocement jacket. It is because the core concrete expanded along the transverse direction when they were subjected to axial compression. The transverse expansion of core concrete caused tensile stress in mortar jacket and ferrocement jacket. When the tensile stress exceeded tensile strength of the jackets, longitudinal cracks appeared on the jackets. After the first crack appeared, loading capacity of strengthened specimens started to decline.

a. Specimen control B

b. Specimen 0L B

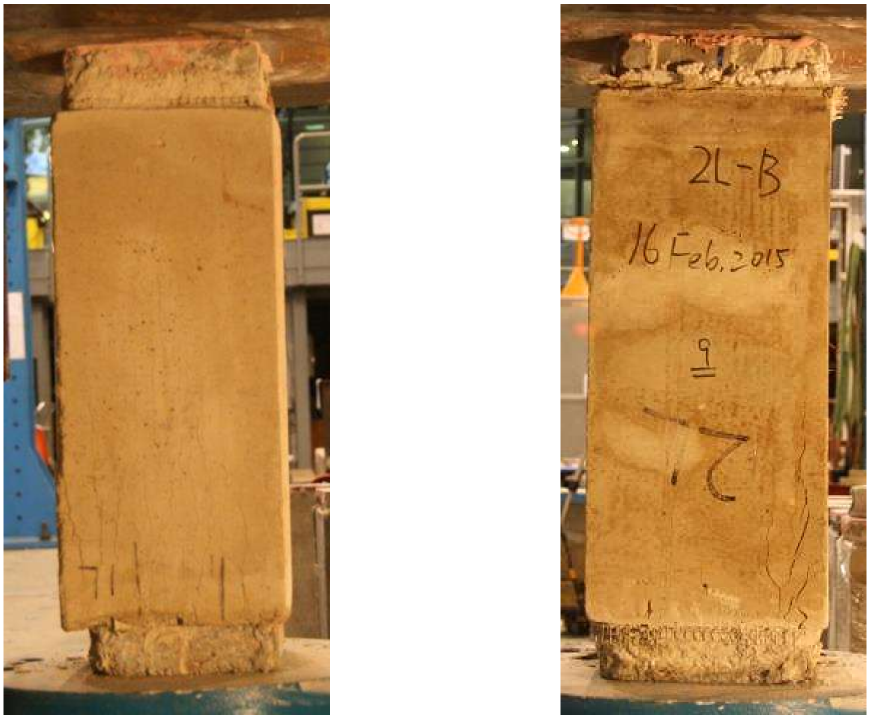

c. Specimen 1L B

d. Specimen 2L B

Figure 5.19 Failure modes of specimens

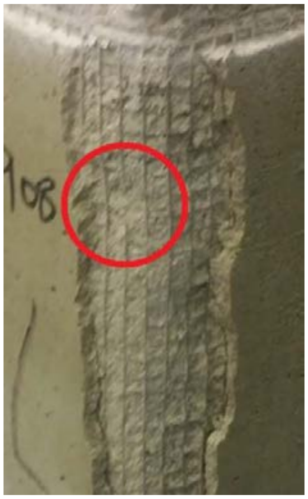

Figure 5.20 Tensile failure of SSWM

Load-deformation relationships of specimens under axial compression are given in Figure 5.21. At initial stage, all the curves were close to each other. When axial load exceeded 700 kN, the control specimens suffered progressive increase in axial deformation, while ferrocement confined specimens maintained their stiffness. When their load reached the peak, specimens confined by ferrocement with two layers of SSWM exhibited the highest peak load, followed by specimens confined by ferrocement with one layer of SSWM and mortar, and control specimen ranked last. Loading capacity of control specimens sharply dropped at post-peak stage, while ferrocement jackets postponed decline in loading capacity and improved ductility of strengthened specimens. Deformation corresponding to peak load and when specimens failed, i.e. peak deformation and ultimate deformation, increased with increasing layers of SSWM.

Peak load, peak deformation and ultimate deformation of specimens are compared under same compressive strength of concrete (Table 5.10). Compared to control specimens, specimens confined by mortar jacket had improvement from 6% to 11% in loading capacity. Ferrocement jackets with one and two layers of SSWM can increase peak load of specimens by 13% and 25%, respectively. Under confinement of AAS ferrocement, column specimens achieved growths up to 51% and 112% in peak deformation and ultimate deformation, respectively.

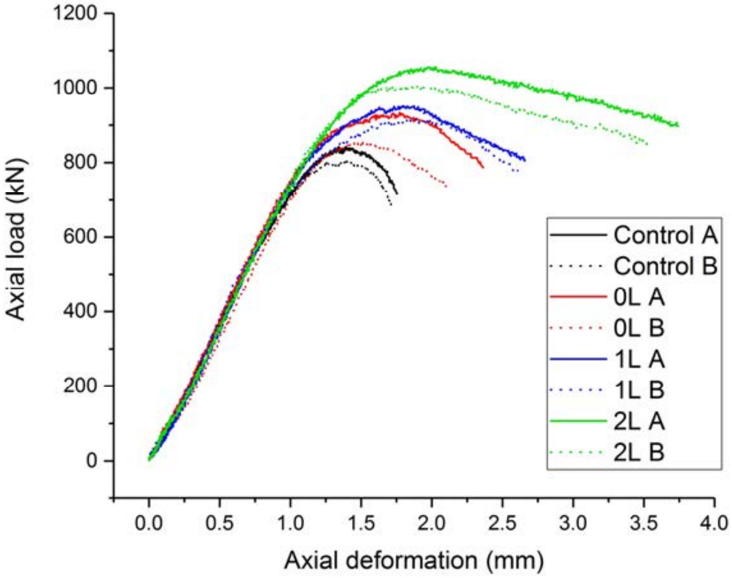

Figure 5.21 Axial load-deformation relationships of specimens

Table 5.10 Peak load, peak deformation and ultimate deformation of specimens

Specimen	f_{cu} (MPa)	Peak load (kN)	Enhancement	Peak deformation (mm)	Ultimate deformation (mm)
Control A	31.5	842.3	-	1.34	1.76
0L A		933.6	10.8%	1.77	2.37
1L A		951.6	13.0%	1.80	2.66
2L A		1056.3	25.4%	2.02	3.73
Control B	29.7	806.4	-	1.42	1.71
0L B		854.5	6.0%	1.47	2.13
1L B		917.9	13.8%	1.89	2.61
2L B		1004.8	24.6%	1.90	3.54

An analytical model based on Saatcioglu and Razvi (1992) is proposed to predict compressive capacity of ferrocement confined columns as follow.

$$f'_{cc} = f'_{c} + k_1 f_{le} \tag{5.6}$$

$$f'_{c} = 0.79 f_{cu} \tag{5.7}$$

$$f_{le} = k_2 f_l \tag{5.8}$$

$$k_1 = 6.7(f_{le})^{-0.17} \tag{5.9}$$

where f'_{cc} and f'_c are compressive strength of confined and unconfined concrete estimated by cylinder. k_2 reflects influence of intervals of lateral reinforcement. k_2 is 1.0 for mortar and ferrocement jackets. f_l is lateral pressure of the jackets on square columns. Experimental results showed loading capacity of confined specimens converted from ascent to descent when the first crack appeared in AAS jacket. Therefore, cracking strength of AAS jacket is considered as maximum lateral confinement to core concrete (Figure 5.22). f_l is given by

$$f_l = \frac{2P_{cr,f}}{b_c s} \tag{5.10}$$

where $P_{cr,f}$ is cracking load of AAS mortar or AAS ferrocement, which can be obtained from Equation (5.4). b_c is width of core concrete. s is longitudinal length of AAS jacket.

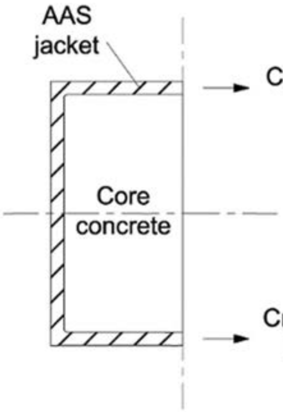

Figure 5.22 Lateral confinement on square columns

Axial loading capacity of unconfined and confined plain concrete columns can be predicted by following equations.

Unconfined column $$P = 0.85 f'_c A_c \tag{5.11}$$

Confined column $$P = 0.85 f'_{cc} A_c \tag{5.12}$$

where f'_c and f'_{cc} are unconfined and confined strength of concrete, respectively. A_c is cross-sectional area of concrete. Prediction of confined strength and axial loading capacity of square columns is given in Table 5.11. Compressive strength of concrete confined by AAS jackets is higher than that of unconfined concrete by 7% to 24%. Predicted peak load is in agreement with test values.

Table 5.11 Prediction of axial loading capacity of square cocrete columns

Specimen	f_c' (MPa)	f_{cc}' (MPa)	Peak load (kN)	
			Prediction	Test value
Control A	24.9	-	846.1	842.3
0L A		26.7	908.4	933.6
1L A		28.7	975.1	951.6
2L A		30.5	1036.7	1056.3
Control B	23.5	-	797.7	806.4
0L B		25.3	860.1	854.5
1L B		27.3	926.7	917.9
2L B		29.1	988.3	1004.8

5.5 Summary

In this chapter, different types of fibers and meshes were used to enhance the flexural performance of AAS mortar. Tensile performance of AAS ferrocement with various layers of SSWM was examined by direct tensile test. Eight square concrete columns were subjected to axial compressive test. Confinement of AAS ferrocement on the columns was investigated and analyzed. Based on the experimental results, summaries are drawn as follows.

1. SSWM can effectively strengthen AAS mortar on both flexural strength and ductility. Uneven distribution of steel fibers in mortar and poor compatibility of GSWM with AAS make these materials unsuitable for strengthening work.

2. SSWM ferrocement exhibits excellent tensile strength and ductility. Cracking stress of ferrocement depends on tensile strength of both SSWM and AAS mortar, while peak load of ferrocement is only related to ultimate strength of SSWM.

3. Ferrocement jacket can increase loading capacity of square concrete columns from 6% to 25% under axial compression. Peak loads of confined specimen increase with increasing layers of SSWM in ferrocement jackets. Confined columns show gentler deterioration at post-peak stage, larger peak deformation and ultimate deformation than unconfined ones. Predicted compressive capacity of confined square columns is close to test results.

CHAPTER 6

USING AAS FERROCEMENT TO STRENGTHEN CORRODED CONCRETE COLUMNS UNDER AXIAL COMPRESSION

6.1 Introduction

Corrosion of reinforcement is considered as a primary factor weakening durability of reinforced concrete structures in corrosive environment. Numerous studies have indicated that the corrosion can cause different extents of damage in concrete structures, such as cracking and spalling of concrete cover, degraded performance of reinforcements, declining loading capacity, and even collapse. It is therefore necessary to strengthen corroded structures to improve their structural performance and durability. AAS mortar and AAS ferrocement have shown their potential in protection of reinforcements and confinement on plain concrete columns in Chapters 4 and 5, respectively. In this chapter, AAS ferrocement is proposed to strengthen corroded reinforced concrete columns. It is the objective of this chapter to investigate improvement of AAS ferrocement jackets on axial compressive strength of corroded columns. For this objective, nine column specimens were subjected to artificially accelerated corrosion. Five corroded specimens were strengthened using AAS mortar and ferrocement jackets. Axial compressive tests were conducted on control, corroded and strengthened specimens. Test results were used to assess corrosion-induced damage to the specimens and effectiveness of proposed strengthening methods.

6.2 Materials and specimens

6.2.1 Materials

Concrete with water-cement ratio of 0.75 was used to simulate the concrete used in the 1950s. Sodium chloride with dosage of 1% of cement mass was added into concrete.

Mix proportion of concrete is given in Table 6.1. The concrete achieved slump of 150 mm. Its 28-day compressive strength estimated by 100mm cubes was 32.5 MPa. Mix proportion of AAS mortar was identical with that used in Chapter 5. AAS ferrocement used for strengthening work consisted of two or four layers of SSWM encapsulated in AAS mortar.

Table 6.1 Mix proportion of concrete (kg/m^3)

Water	210
Cement	280
Coarse aggregate (10mm)	395
Coarse aggregate (20mm)	790
Sand	705
Sodium chloride	2.8

Deformed bars with diameter of 12 mm (“T12”) and plain bars with diameter of 6 mm (“R6”) were used as main reinforcements and stirrups, respectively. Measured yield strength and ultimate strength of T12 and R6 bars are given in Table 6.2.

Table 6.2 Measured yield strength and ultimate strength of reinforcements (MPa)

	Yield strength	Ultimate strength
T12	550	651
R6	477	530

6.2.2 Preparation of specimens

Reinforced concrete column specimens were designed according to a five-storey building completed in 1955. The column specimens had height of 900 mm and a cross section of 200 mm × 200 mm. Concrete cover to main reinforcement was 38 mm. Reinforcements were consisted of four T12 main reinforcements and ten R6 stirrups. Spacing of stirrups was 150 mm at mid-height of specimen. Stirrups were intensified at both ends of specimen to prevent failure at the end sections. 90° hooks were bent at both ends of the stirrups. The main reinforcements and stirrups were protected by epoxy at two ends of corroded and strengthened specimens (Figure 6.1).

Ten full-scale specimens were cast horizontally and compacted on a vibrating table. The specimens were removed from the formwork one day after casting, and were cured in water for 28 days. Compressive strengths of concrete ("f_{cu}") were tested when the column specimens were tested (Table 6.3).

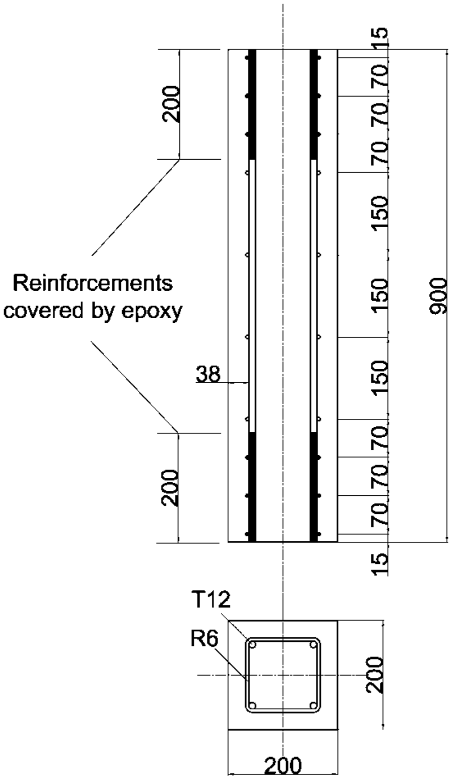

Figure 6.1 Schematic view of specimens (unit: mm)

6.2.3 Artificially accelerated corrosion on column specimens

After cured, nine specimens except control specimen were subjected to artificially accelerated corrosion. Objective degrees of corrosion, i.e. corrosion-induced mass loss of main reinforcements, were 10% and 20% (Table 6.3). The column specimens were immersed in sodium chloride solution with concentration of 5%. Air was pumped into the solution to supply oxygen to corrosion reaction. Main reinforcements were connected to the anode and sodium chloride solution was connected to the cathode of direct current power supply (Figure 6.2). According to Faraday's laws of electrolysis, electric current was kept at 0.68A for 21 and 42 days for specimens with objective degrees of corrosion of 10% and 20%, respectively.

Table 6.3 Details of specimens

Details of specimen	Specimen ID	Objective degree of corrosion	Strengthening scheme	f_{cu} (MPa)
Control	A0	-	-	32.5
Corroded	A10M	10%		33.2
	A10			33.2
	A20M	20%		33.2
	A20			33.2
Strengthened	A10S2	10%	Ferrocement jacket with two layers of SSWM	35.1
	A20S0N	20%	Mortar jacket and new stirrups	33.5
	A20S2		Ferrocement jacket with two layers of SSWM	33.5
	A20S2N		Ferrocement jacket with two layers of SSWM and new stirrups	33.5
	A20S4		Ferrocement jacket with four layers of SSWM	33.5

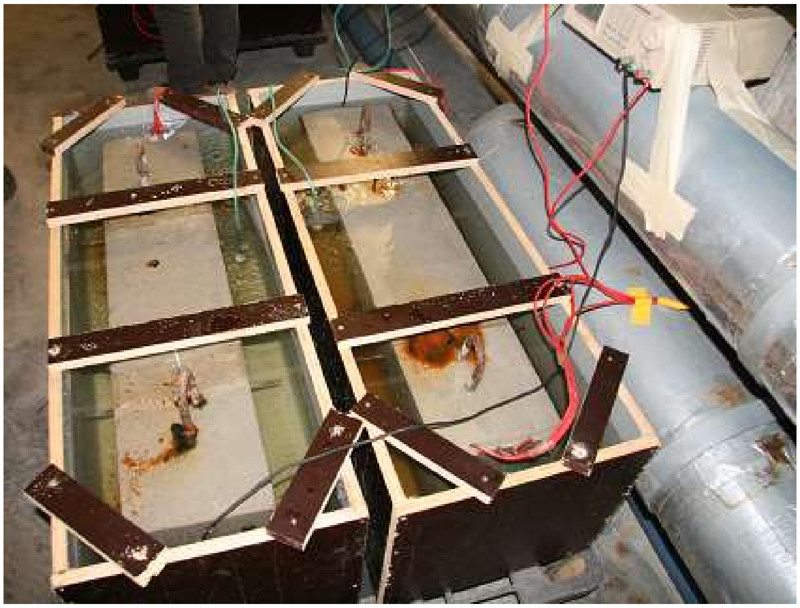

Figure 6.2 Artificially accelerated corrosion on column specimens

Accelerated corrosion resulted in obvious longitudinal cracks in specimens. Corrosion products exuded through the cracks and contaminated surface of specimens. One hook fractured due to severe corrosion in specimens with objective degrees of corrosion of 20%

(Figure 6.3). To evaluate degrees of corrosion, stirrups and main reinforcements at the mid-height of specimens A10M and A20M were cut off and cleaned in hydrochloric acid solution according to ASTM G1-03. Mass losses of main reinforcements and stirrups are given in Table 6.4. As shown in Figure 6.4, ribs were partially visible on deformed bar with mass loss of 7.16%, while were completely dissolved on deformed bar with mass loss of 20.30%. There was severe pitting corrosion on both stirrups and main reinforcements. Corrosion at corners of stirrups was severer than that at other parts. Mass losses of stirrups were more than double those of main reinforcements. This is because stirrups corrode more easily than main reinforcements owing to thinner concrete cover of stirrups. Intact main reinforcements and corroded stirrups formed a corrosion cell which exacerbated corrosion of stirrups acting as the anode of the cell (Otsuki et al. 2000). After cleaned by hydrochloric acid, corroded main reinforcements were subjected to tensile tests. Force-strain relationships of reinforcements under tension are given in Figure 6.5. The corroded reinforcements showed obvious yield behavior even with degree of corrosion up to 20.3%. Both yield load and ultimate load of corroded reinforcements declined with increasing degrees of corrosion (Table 6.5). Corroded reinforcements suffered from severer loss in yield force and ultimate load than that in mass, which reflects adverse effect of pitting corrosion on mechanical performance of reinforcements. Using mass loss of reinforcements as an indicator to evaluate degree of corrosion may overestimate tensile strength of corroded reinforcements.

a. Specimen with objective degree of corrosion of 10%

b. Specimens with objective degree of corrosion of 20%

Figure 6.3 Specimens after accelerated corrosion

Table 6.4 Mass loss of reinforcements of specimens A10M and A20M

Specimen	Reinforcement	Mass loss ratio	Average
A10M	Main reinforcement	9.54%	8.91%
		7.16%	
		9.47%	
		9.46%	
	Stirrup	23.36%	20.98%
		20.92%	
		18.66%	
A20M	Main reinforcement	20.30%	18.28%
		18.05%	
		17.13%	
		17.64%	
	Stirrup	39.33%	43.22%
		42.50%	
		47.82%	

a. Main reinforcement with mass loss of 7.16%

b. Main reinforcement with mass loss of 20.30%

c. Stirrup with mass loss of 20.92%

d. Stirrup with mass loss of 40.45%

Figure 6.4 Corroded reinforcements

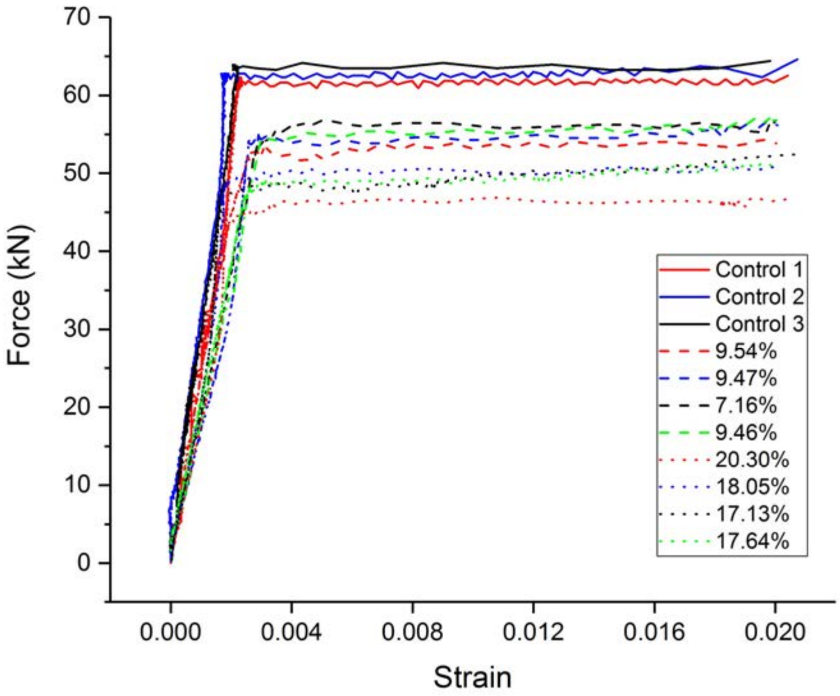

Figure 6.5 Force-strain relationships of corroded reinforcements

Table 6.5 Yield load and ultimate load of corroded reinforcements

Specimen	Mass loss ratio	Yield load (kN)	Loss in yield load	Ultimate load (kN)	Loss in ultimate load
Control 1	-	61.40	-	77.73	-
Control 2		62.32		78.65	
Control 3		62.09		77.97	
A10M-1	9.54%	53.36	13.85%	63.47	18.75%
A10M-2	7.16%	55.75	9.99%	66.32	15.10%
A10M-3	9.47%	54.50	12.01%	64.62	17.28%
A10M-4	9.46%	55.14	10.97%	65.48	16.18%
A20M-1	20.30%	46.22	25.38%	58.64	24.93%
A20M-2	18.05%	49.90	19.43%	55.19	29.35%
A20M-3	17.13%	48.07	22.39%	58.87	24.64%
A20M-4	17.64%	48.52	21.66%	60.02	23.17%

6.2.4 Strengthening schemes

As shown in Table 6.3, there are four different strengthening schemes, named “S0N”, “S2”, “S2N” and “S4”. S0, S2 and S4 represent AAS mortar jacket, AAS ferrocement jacket with two and four layers of SSWM, respectively. N represents replacement of corroded stirrups by new ones.

Strengthening work was consisted of three steps as follows: 1. Concrete cover was removed to expose reinforcements. Concrete in contact with corroded reinforcements was also chiseled (as shown in red boxes in Figure 6.6 (a)). Rust on the surface of reinforcements was cleaned by steel wire brush. 2. Corroded stirrups were replaced by welded “C” type stirrups in schemes “S0N” and “S2N” (Figure 6.6 (b)). 3. Core concrete was wrapped by SSWM in schemes “S2”, “S2N” and “S4”. The SSWM overlapped at length of 120mm at its end (Figure 6.6 (c)). 4. Core concrete was damped. AAS mortar was cast over core concrete using wooden formwork (Figure 6.6 (d)). 5. The formwork was dismantled 24 hours after casting. AAS jacket was moistened and wrapped by polyethylene film for 14 days. The specimens retained their original size after strengthening (Figure 6.7(a)). Specially, foamed polystyrene caps were placed on both ends of strengthened specimens to prevent ferrocement jacket from subjected to loading under axial compression (Figure 6.7(b)).

a. Removing concrete cover

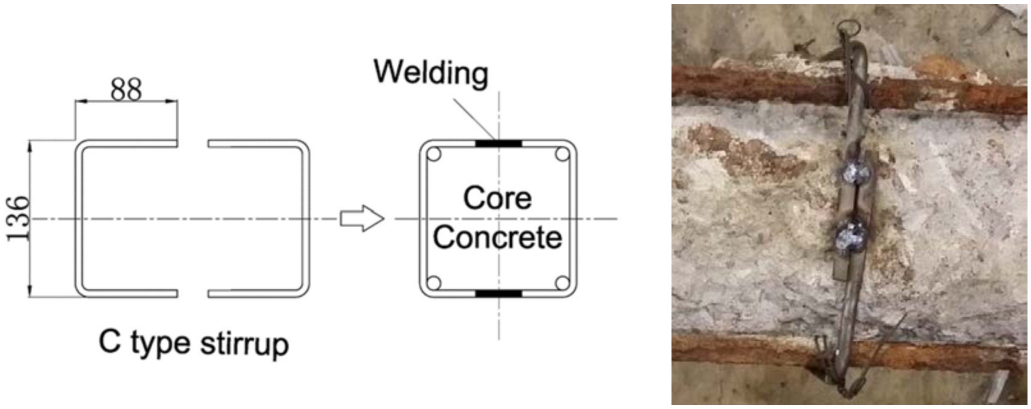

b. “C” type stirrup (unit: mm)

c. Wrapping core concrete with SSWM

d. Casting mortar using wooden formwork

Figure 6.6 Strengthening procedure

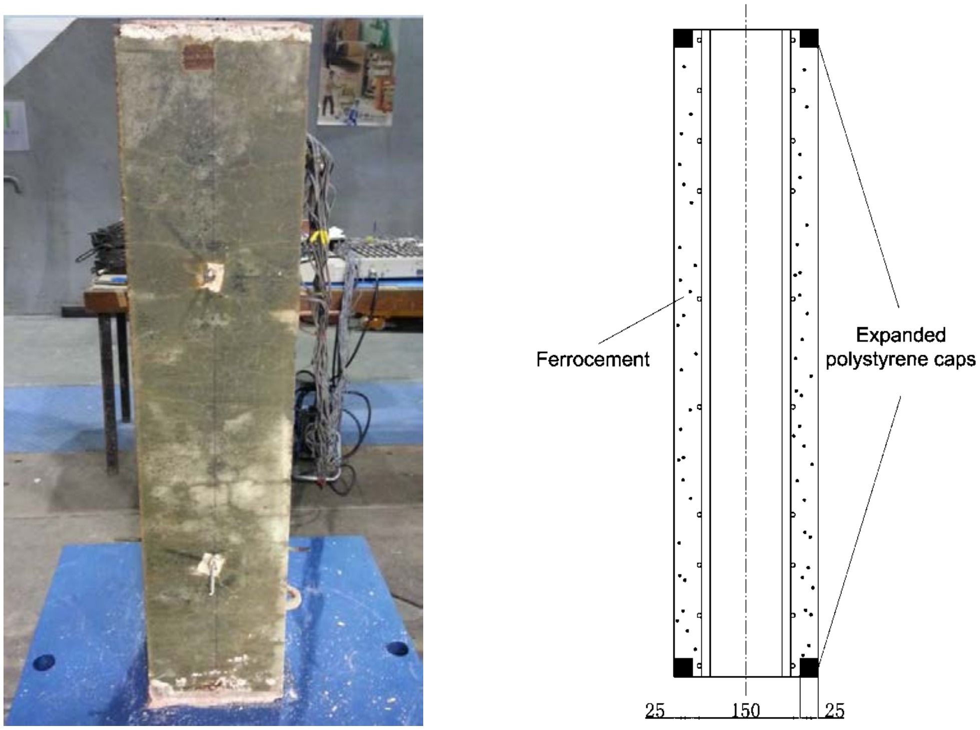

a. Specimen after strengthening b. Polystyrene caps (unit: mm)

Figure 6.7 Details of strengthened specimen

6.2.5 Experimental setup

Strain gauges were installed on main reinforcements, stirrups and surface of concrete at mid-height of specimens. They were protected by waterproof adhesive and butyl tape from damage during casting and artificially accelerated corrosion. Two pairs of LVDTs were connected to stainless steel rods pre-embedded in concrete to measure axial deformation of specimens. Locations of LVDTs and strain gauges are given in Figure 6.8.

Axial compressive tests were conducted on specimens A0, A10, A20, A10S2, A20S0N, A20S2, A20S2N and A20S4. Both end surfaces of specimens were capped by gypsum. Specimens were preloaded to 5 kN to eliminate the gap between testing machine and specimens. Axial load was applied with loading rate of 0.1 mm/min and 0.05 mm/min in pre-peak and post-peak stage, respectively. Compressive tests were terminated when loading capacity declined to 85% of its maximum.

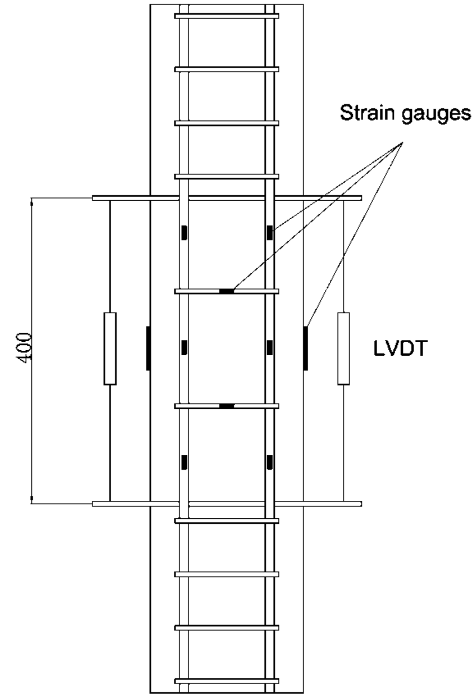

Figure 6.8 Locations of the LVDTs and strain gauges (unit: mm)

6.3 Results and discussion

6.3.1 Failure modes

Figure 6.9 shows failure mode of control specimen A0. Crack did not appear in the specimen until axial load reached its peak of 1117 kN. When axial load declined to 1085 kN, the first crack appeared and developed parallel to main reinforcements. With increasing displacement, the crack propagated and new cracks appeared. When axial load was reduced to 85% of its maximum, cracks intersected with each other (Figure 6.9(a)). Concrete cover spalled off locally as shown in Figure 6.9(b). After concrete cover was removed after test, stirrups were found to remain intact and main reinforcements between stirrups buckled. Specimen A0 failed owing to compressive failure of concrete and buckling of main reinforcements.

a. Cracks pattern b. Spalled concrete c. Buckled reinforcement

Figure 6.9 Failure mode of specimen A0

Failure mode of specimen A10 is shown in Figure 6.10. Under increasing axial loading, corrosion-induced longitudinal cracks widened and propagated rapidly (Figure 6.10(a)). When axial load reached its peak, the longitudinal cracks expanded to its maximum width of 5 mm. Concrete cover at mid-height spalled off (Figure 6.10(b)). Specimen A10 experienced a sudden deterioration in loading capacity. This phenomenon can be explained by an observation of reinforcements of specimen after test (Figure 6.10(c)). A corroded stirrup at mid-height fractured, which lost confinement to core concrete and resulted in buckling of main reinforcements. Longitudinal cracks were fully developed in core concrete.

a. Cracks pattern b. Spalled concrete c. Fractured stirrup

Figure 6.10 Failure mode of specimen A10

Compared to specimen A10, specimen A20 experienced similar failure mode, lower loading capacity and severer damage in concrete (Figure 6.11(a)). Concrete cover of specimen A20 spalled off and exposed main reinforcements. Stirrups fractured at their corners and lost confinement to core concrete and main reinforcements (Figure 6.11(b)). Specimen A20 failed due to buckling of main reinforcement and compressive failure of concrete. Stirrups in both specimens A10 and A20 were found to have fractured at corners, which is attributed to serious pitting corrosion (Figure 6.4(c),(d)).


a. Severe damage in concrete b. Buckled reinforcement

Figure 6.11 Failure mode of specimen A20

Failure mode of specimen A10S2 is shown in Figure 6.12. No crack was found until compressive load reached it maximum of 1104 kN. Specimen A10S2 first cracked at a corner of ferrocement jacket (Figure 6.12(a)). The crack originated from the top of jacket and developed downward. With increasing axial displacement, a growing number of cracks formed in the jacket. Specimen A10S2 lost its loading capacity due to tensile failure of ferrocement jacket (Figure 6.12(b)). AAS mortar was found crushed inside SSWM (Figure 6.12(c)). This failure mode is similar to that reported by Kaish et al. (2012). However, specimen A10S2 exhibited a ductile response in post-peak stage because of confinement action provided by SSWM on core concrete.

a. Initial crack in ferrocement jacket

b. Longitudinal cracks in ferrocement jacket

c. Crushed mortar inside SSWM

Figure 6.12 Failure mode of specimen A10S2

Similar to specimen A10S2, specimen A20S0N first cracked at a corner of mortar jacket (Figure 6.13(a)). With progressive increase in axial displacement, more longitudinal cracks appeared in the mortar jacket. Width of the cracks of specimen A20S0N were larger than that of specimen A10S2 owing to lack of SSWM. The corner of jacket spalled in post-peak stage accompanied with prompt deterioration in loading capacity (Figure 6.13(b)).

a. The first crack in mortar jacket b. Spalled mortar jacket

Figure 6.13 Failure mode of specimen A20S0N

Failure of both specimens A20S2 and A20S2N was initiated by longitudinal cracks in ferrocement jacket, and followed by tensile failure of ferrocement and spalling of corners of jacket (Figure 6.14 and Figure 6.15). Specimen A20S2 achieved close peak load to specimen A20S2N. Owing to confinement of SSWM, loading capacities of specimens A20S2 and A20S2N deteriorated more slowly than that of specimen A20S0N in post-peak stage.

Figure 6.16 shows failure mode of specimen A20S4. When the specimen achieved its peak strength, the first longitudinal crack formed in the middle of ferrocement jacket. Benefited by four layers of SSWM, the jacket of specimen A20S4 exhibited the best ductility. In post-peak stage, more longitudinal cracks appeared. Cracks in specimen A20S4 were finer and more intensive than those in specimen A20S2 (Figure 6.16(a)). Under increasing axial displacement, corner of ferrocement spalled in succession. SSWM buckled at end of test (Figure 6.16(b)).

Figure 6.14 Tensile failure of ferrocement jacket

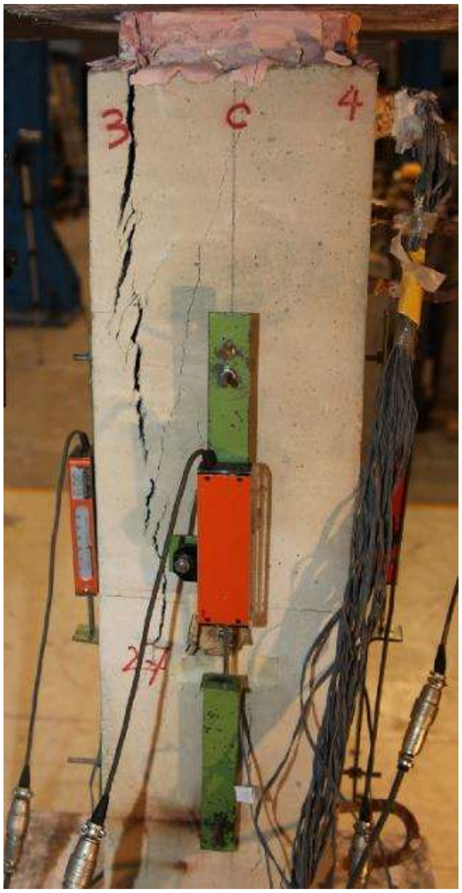

Figure 6.15 Spalled corner of ferrocement jacket

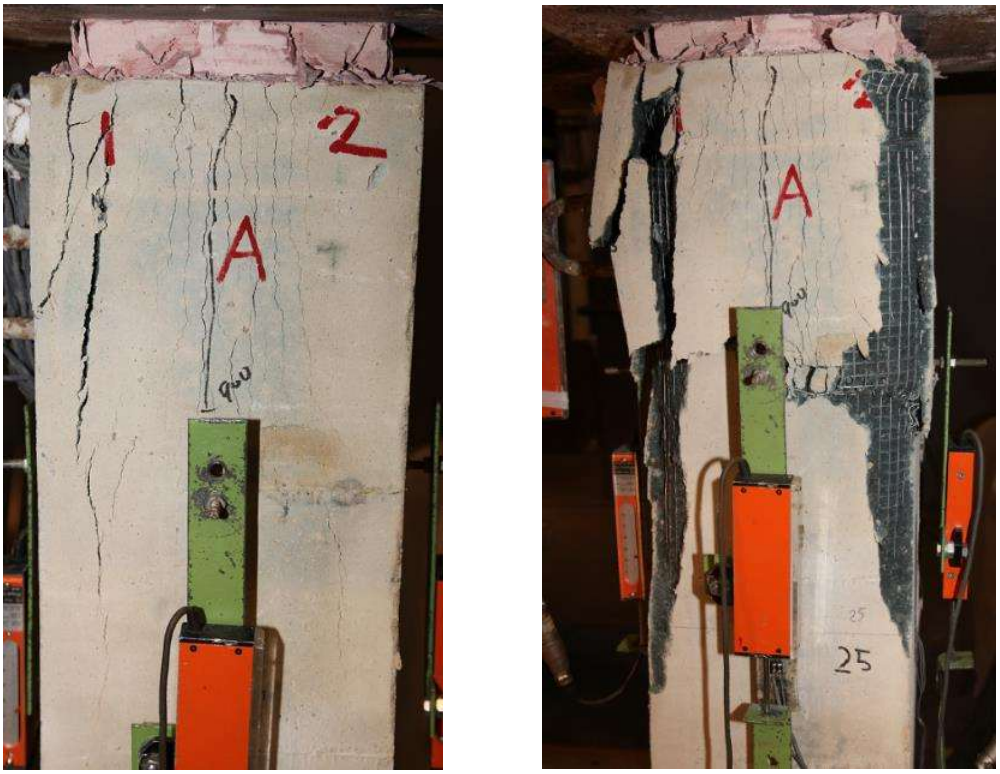

a. Intensive cracks in jacket

b. Spalled ferrocement jacket and buckled SSWM

Figure 6.16 Failure mode of specimen A20S4

6.3.2 Load-deformation relationships

Load-deformation relationships of specimens under axial compression are given in Figure 6.17. Control specimen A0 exhibited the highest loading capacity of 1117 kN. Corrosion of reinforcements exerted significant negative effect on mechanical performance of column specimens. Corroded specimens A10 and A20 experienced severe reduction of 28% and 46% in peak load as compared with control specimen, respectively. The higher degree of corrosion was, the more severely the specimen deteriorated. The corroded specimens sharply declined in their loading capacity in post-peak stage, which is related to reducing cross-sectional area caused by spalled concrete. Benefited from ferrocement jackets, strengthened specimens achieved varying degrees of rehabilitation in loading capacity. Specimen A10S2 reached peak strength close to the control one, which demonstrated effectiveness of ferrocement in improvement of loading capacity. Among specimens with degree of corrosion of 20%, specimen A20S4 showed the highest loading capacity of 984.4 kN, followed by specimens A20S2N and A20S2. Specimen A20S0N ranked the fourth while corroded specimen A20 performed the lowest strength of 603.7 kN. All the strengthening schemes improved axial compressive strength of corroded specimens. Moreover, new stirrups and ferrocement jackets are beneficial to postpone the degradation of loading capacity of specimens in post-peak stage. Compared to corroded specimens, strengthened ones especially specimen A20S4 had better ductility and slower decline in compressive strength, which was attributed to improved confinement to core concrete.

Strengthened specimens showed larger axial deformation than control specimen A0. It is because the ferrocement jacket did not carry axial compression directly, but provided lateral confinement to core concrete only. Compared with control specimen, strengthened specimens had smaller compressive area and thus exhibited less stiffness under axial compression. In addition, corrosion-induced cracks in concrete deteriorated stiffness of specimens. Axial deformation of corroded specimens increased rapidly as the cracks propagated and connected with each other. At initial stage, load-deformation curves of strengthened specimens were close to those of corroded specimen under same degree of corrosion. With increasing loading, corrosion-induced cracks developed rapidly and weakened stiffness of corroded specimen, while strengthened specimens were able to retain their stiffness. Ferrocement jackets stiffened the column specimens.

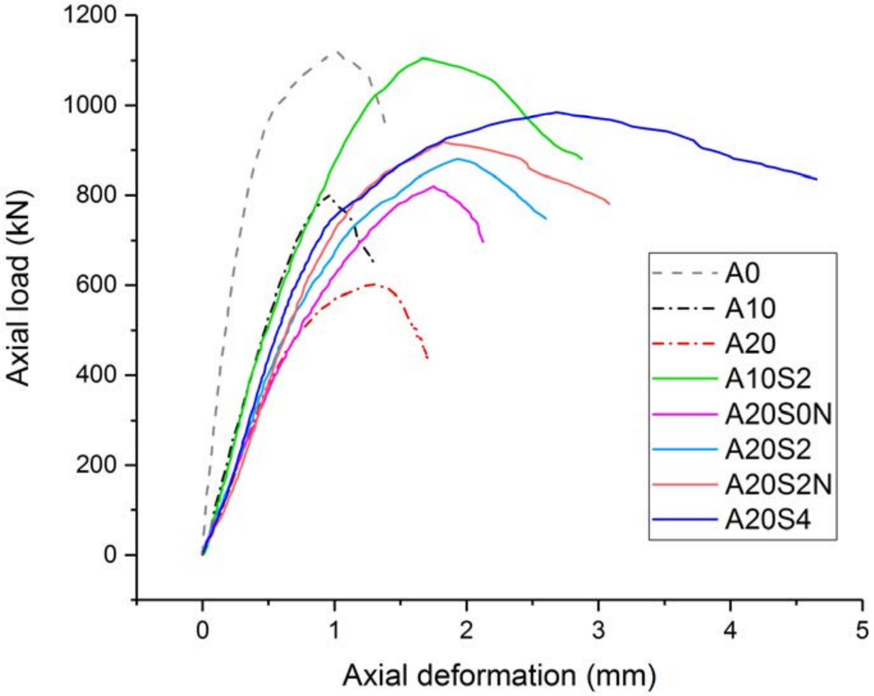

Figure 6.17 Load- deformation relationships of specimens under axial compression

Strain of main reinforcements of all specimens is given in Figure 6.18. Corrosion weakened cross section of reinforcements, which resulted in larger compressive strain of main reinforcements in corroded specimens than in control one. Specimen A20 showed the maximum strain of reinforcements under same axial load. As ferrocement jackets provided lateral confinement to main reinforcements, buckling of main reinforcements was suppressed. All main reinforcements in strengthened specimens can carry load after reached their yield strain of 0.0026. Compared to control specimen, strengthened ones achieved greater strain in main reinforcements because their ferrocement jackets did not carry compression directly.

Strain of stirrups of all specimens is given in Figure 6.19. In initial stage of test, strain of stirrups was small. With progressive increase in axial loading, transverse expansion of core concrete increased the tension in stirrups. Stirrups of specimen A20 displayed maximum strain, which is attributed to its impaired cross section caused by corrosion. After specimens reached their peak load, significant lateral restraint was provided to core concrete by ferrocement jacket and stirrups. Strain of stirrups rapidly increased in post-peak stage. Stirrups of control and strengthened specimens achieved their yield strain of 0.0022 when the specimens failed. Strain of stirrups of specimen A20S0N was larger than that of other strengthened specimens. This is because SSWM in the latter shares tensile stress and reduce tensile strain of stirrups.

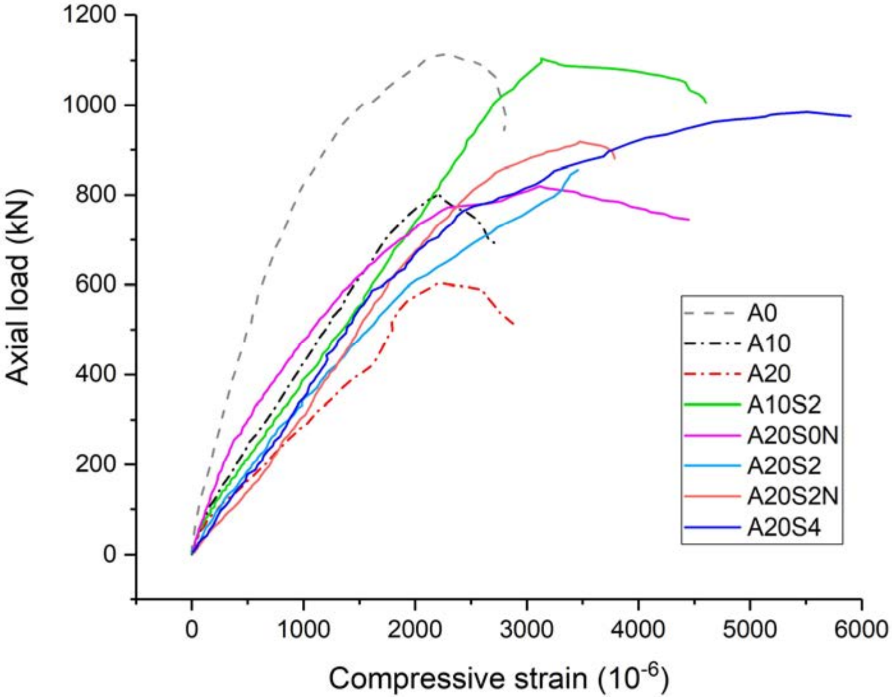

Figure 6.18 Strain of main reinforcements

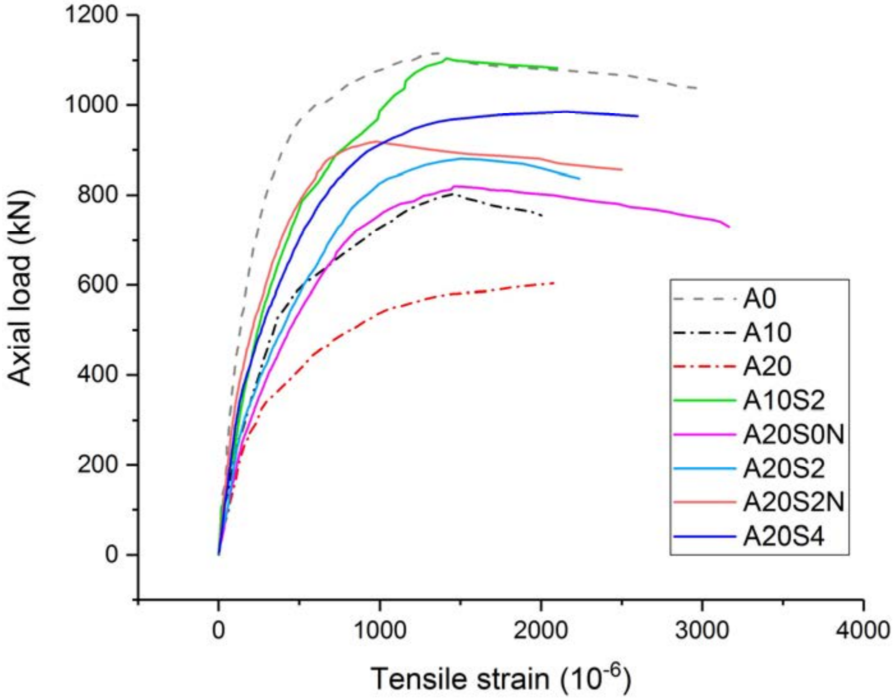

Figure 6.19 Strain of stirrups

6.3.3 Loading capacity and ductility

Yield load "P_y", peak load "P_p", yield deformation "Δ_y", ultimate deformation "Δ_u", ductility, and ratios of peak load of the specimens to that of control specimen ($P_p/P_{p,con}$) are given in Table 6.6. Paulay and Priestley (1992) recommended the yield deformation can be obtained from the following equation

$$\Delta_y = \frac{P_p}{P_y'}\Delta_y' \qquad (6.1)$$

where P_y' is first yield load, taken as 0.75 P_p. Δ_y' is the deformation corresponding to P_y'. Ultimate deformation is defined as the deformation when the load declines to 85% of its maximum (Figure 6.20). Deformation ductility is obtained by ultimate deformation divided by yield deformation.

As shown in Table 6.6, loading capacities of specimens decline with increasing degrees of corrosion. Corroded specimens A10 and A20 suffered reduction of 28% and 46% in compressive strength as compared with control specimen, respectively. All the proposed strengthening schemes "S0N", "S2", "S2N" and "S4" achieved obvious improvement in both yield load and peak load. After strengthened by ferrocement with two layers of SSWM, specimen A10S2 reached compressive capacity comparable to that of control specimen A0. Compared to corroded specimen A20, strengthened specimens A20S0N, A20S2, A20S2N and A20S4 enhanced loading capacities by 36%, 46%, 52% and 63%, respectively. Peak load of specimens A20S2 and A20S4 were higher than that of specimens A20S0N and A20S2N by 7.4% and 7.2%, respectively, which demonstrates applying two layers of SSWM to corroded columns is more effective than using new stirrups for confinement.

In addition to loading capacity, both ultimate deformation and ductility of specimens were efficiently improved by ferrocement jackets. Ferrocement with two layers of SSWM increased ductility of corroded specimen A10 by 32%. When SSWM was increased to four layers, strengthened specimen A20S4 achieved double ductility than specimen A20. SSWM was proved to be more effective than new stirrups in enhancement of ultimate deformation and postponement of deterioration of loading capacity, which is attributed to excellent elongation and intensive distribution of stainless steel wires in ferrocement.

Table 6.6 Loading capacity, deformation and ductility

Specimen	P_y (kN)	P_p (kN)	$P_p/P_{p,con}$	Δ_y (mm)	Δ_u (mm)	Ductility
A0	959.7	1117.3	100.0%	0.49	1.39	2.84
A10	735.7	804.0	72.0%	0.78	1.22	1.56
A20	530.9	603.7	54.0%	0.85	1.59	1.87
A10S2	1000.3	1104.5	98.9%	1.25	2.57	2.06
A20S0N	728.4	819.5	73.3%	1.30	2.13	1.64
A20S2	773.0	879.9	78.8%	1.31	2.60	1.98
A20S2N	815.1	918.4	82.2%	1.25	3.08	2.46
A20S4	816.1	984.4	88.1%	1.28	4.65	3.63

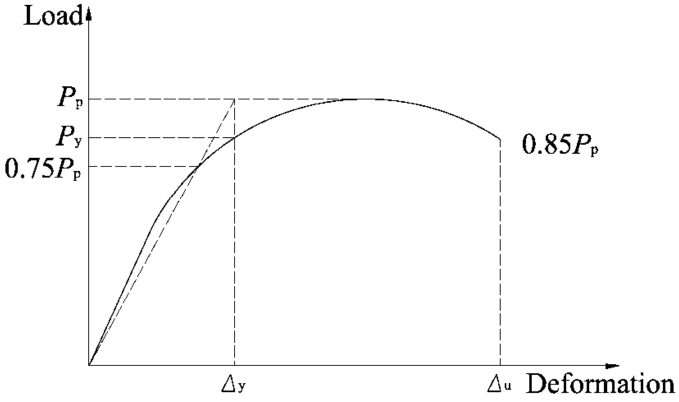

Figure 6.20 Definition of yield load and yield deformation

6.4 Prediction of loading capacity of columns under axial compression

The mathematic model verified in Chapter 5 is used to predict compressive strength of confined concrete as follows

$$f'_{cc} = f'_c + k_1 f_{le} \tag{6.2}$$

$$f_c' = 0.79 f_{cu} \tag{6.3}$$

$$k_1 = 6.7(f_{le})^{-0.17} \tag{6.4}$$

where f_{cc}' and f_c' are compressive strength of confined and unconfined concrete estimated by cylinder. f_{le} is equivalent lateral confinement to core concrete which comprises lateral pressure of AAS ferrocement ($f_{l,f}$) and stirrups ($f_{l,s}$) (Figure 6.21). According to Saatcioglu and Razvi (1992), lateral confinement of AAS ferrocement and stirrups can be combined. Therefore, f_{le} is given as follows.

$$f_{le} = k_f f_{l,f} + k_s f_{l,s} \tag{6.5}$$

$$f_{l,f} = \frac{2P_{cr,f}}{b_c s_s} \tag{6.6}$$

$$f_{l,s} = \frac{2A_{st}\sigma_{st}}{b_c s_s} \tag{6.7}$$

where $P_{cr,f}$ is cracking load of AAS mortar or AAS ferrocement, which can be obtained from Equation (5.4). b_c is width of core concrete. s_s is spacing of stirrups. A_{st} and σ_{st} are effective cross-sectional area and stress of corroded stirrup. k_f and k_s reflect influence of intervals of SSWM and stirrups. k_f is 1.0 for mortar and ferrocement jackets. k_s is given in following equation.

$$k_s = 0.26\sqrt{\left(\frac{b_c}{s_s}\right)\left(\frac{b_c}{s_l}\right)\left(\frac{1}{f_{l,s}}\right)} \leq 1.0 \tag{6.8}$$

where s_l is spacing of main reinforcements.

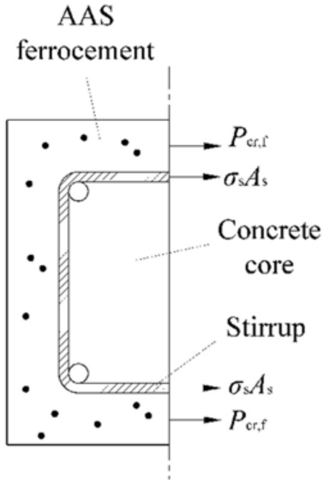

Figure 6.21 Lateral pressure on core concrete

Loading capacity "P", peak strain "ε_p" and ultimate strain "ε_u" of strengthened specimens under axial compression can be predicted by the following equations.

$$P = 0.85 f'_{cc} A_c \tag{6.9}$$

$$\varepsilon_p = \varepsilon_{p0}\left(1+\frac{5k_1 f_{le}}{f'_c}\right) \tag{6.10}$$

$$\varepsilon_u = 260\frac{\sum(A_{st}+A_{ss})}{2s_s b_c}\varepsilon_p+\varepsilon_{u0} \tag{6.11}$$

where f'_{cc} and A_c are confined strength and cross-sectional area of core concrete, respectively. ε_p and ε_{p0} are the strain of confined and unconfined specimens corresponding to peak load, respectively. ε_u and ε_{u0} are the strain of confined and unconfined specimens when axial load declines to 85% of its peak value. Values of 0.002 and 0.0038 are recommended for ε_{p0} and ε_{u0} based on Saatcioglu and Razvi (1992)'s model. Prediction of loading capacity, peak strain and ultimate strain of strengthened specimens is given in Table 6.7. Predicted ultimate strain is in good agreement with that obtained from the tests. Predicted peak load and peak strain are slighly less than the test values. This is because axial compressive stress of ferrocement jackets was not considered in the prediction.

Table 6.7 Prediction of peak load, peak strain and ultimate strain

Specimen	Peak load (kN)		Peak strain		Ultimate strain	
	Prediction	Test value	Prediction	Test value	Prediction	Test value
A10S2	944.5	1104.5	0.00551	0.00417	0.00685	0.00643
A20S0N	827.8	819.5	0.00459	0.00437	0.00530	0.00533
A20S2	881.7	879.9	0.00568	0.00481	0.00653	0.00650
A20S2N	883.7	918.4	0.00572	0.00457	0.00736	0.00770
A20S4	944.2	984.4	0.00694	0.00671	0.00918	0.01163

6.5 Assessment of strengthening schemes

Four different strengthening schemes, “S0N”, “S2”, “S2N” and “S4”, were used to strengthen corroded column specimens. All the schemes were able to improve axial compressive capacity of specimens. Both ferrocement jackets and new stirrups provide lateral pressure to core concrete and thus increase compressive strength of confined concrete. Lateral pressure of ferrocment jackets is regarded as uniform confinement due to closely spaced SSWM (Saatcioglu and Razvi 1992). However, confinement of stirrups to core concrete depends on spacing of stirrups. The larger spacing of stirrups is, the less lateral pressure is. Concrete between stirrups is ineffectively confined (Figure 6.22). Equivalent lateral confinement of stirrups ($k_s f_{l,s}$) and ferrocement jacket ($k_f f_{l,f}$) which consider effect of spacing of transverse reinforcements are calculated using Equations (6.6) - (6.8) and is given in Table 6.8.

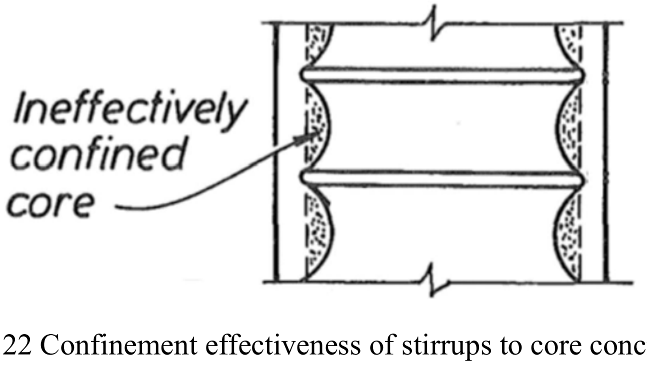

Figure 6.22 Confinement effectiveness of stirrups to core concrete (Mander et al. 1988)

Table 6.8 Equivalent lateral confinement of varying strengthening schemes

Strengthening schemes	Volume fraction of transverse reinforcements	$k_f f_{l,f}$ (MPa)	$k_s f_{l,s}$ (MPa)	$k_f f_{l,f}$ + $k_s f_{l,s}$ (MPa)
S0N	0.0056	0.645	0.262	0.907
S2	0.0045	1.233	0	1.233
S2N	0.0101	1.233	0.214	1.447
S4	0.0090	1.822	0	1.822

As shown in Table 6.8, ferrocement jacket provides remarkable confinement to core concrete than new stirrups. Equivalent lateral pressure of stirrups is averagely 19% to that of ferrocement with two layers of SSWM, even though the former has higher volume fraction. Schemes S2 and S4 show equivalent lateral confinement larger than schemes S0N and S2N by 36% and 26%, respectively. This demonstrates SSWM performs better than stirrups to confine core concrete.

Above estimation is verified by the test results in Section 6.3. Specimens A20S2 and A20S4 exhibited peak strength higher than specimens A20S0N and A20S2N by 7.4% and 7.2%, respectively. In addition to loading capacity, schemes S2 and S4 performed better than stirrups in improvement of ductility of specimens. Compared to corroded specimen A20, strengthened specimens A20S2 and A20S4 enhanced ductility by 6% and 94%, while specimen A20S0N showed a reduction of 12%.

Moreover, ferrocement with SSWM performs better than steel stirrups in chloride-rich environment owing to excellent corrosion resistance of stainless steel. In consideration of mechanical properties and durability, schemes S2 and S4 are recommended as the strengthening schemes for corroded columns with degree of corrosion of 10% and 20%, respectively.

6.6 Summary

In this chapter, ten full-scale reinforced concrete columns were prepared. Nine of them were subjected to accelerated corrosion to achieve degrees of corrosion of 8.9% and 18.3% in main reinforcements. Four different strengthening schemes were employed to strengthen the corroded specimens. Axial compressive tests were conducted on control, corroded and strengthened specimens. Influence of corrosion of reinforcement on performance of specimens was investigated. Effectiveness of the proposed strengthening schemes were experimentally evaluated. Empirical formulas based on confinement effect were proposed to predict the loading capacity, peak strain and ultimate strain of strengthened specimens. The prediction is in good agreement with the experimental results. Primary summaries are drawn as follows.

1. Chloride causes severe pitting corrosion and weakens both yield strength and ultimate strength of reinforcements. Using average mass loss to evaluate degree of corrosion of reinforcements may underestimate negative influence of pitting corrosion on tensile strength of reinforcements.

2. Degree of corrosion of stirrups is severer than that of main reinforcements. Mass loss of stirrups caused by corrosion is 2.4 times than that of main reinforcements. Corroded column specimens failed under axial compression due to fracture of stirrups at corners and buckling of main reinforcement.

3. Corrosion of reinforcement can severely weaken the loading capacity, stiffness, and ductility of reinforced concrete columns. Degree of corrosion of 8.9% and 18.3% on main reinforcements results in loading capacity losses of 28% and 46%, respectively. Compared to control specimen, corroded ones suffer significant reduction in ductility up to 45%.

4. All the proposed strengthening schemes exhibit improvement in peak load and ductility of corroded specimens. After strengthened using scheme S2, specimen with degree of corrosion of 8.9% can rehabilitate loading capacity comparable to control specimen. For specimens with degree of corrosion of 18.3%, schemes S0N, S2, S2N and S4 improve their loading capacities from 36% to 63%. Scheme S4 performs the best in enhancement of ductility. Specimen strengthened using scheme S4 achieves approximately two times the ductility than the corroded specimen without strengthening.

5. Ferrocement jackets provide better and uniform confinement to core concrete than new stirrups. Specimens strengthened using ferrocement with two layers of SSWM performs higher peak load and ductility than those using new stirrups.

6. In consideration of mechanical performance and durability, schemes S2 and S4 are recommended to strengthen corroded columns with degree of corrosion of 10% and 20%, respectively.

CHAPTER 7

USING AAS FERROCEMENT TO STRENGTHEN CORRODED CONCRETE COLUMNS WITH ECCENTRICITY

7.1 Introduction

Columns are rarely loaded axially in practice owing to axis deviation between columns and beams or moment introduced by continuous beams. Combined bending moment M and axial force P can be equivalent to a force P with an eccentricity e (Equation (7.1)).

$$e = \frac{M}{P} \tag{7.1}$$

In this chapter, corrosion-induced mechanical deterioration in columns and effectiveness of AAS ferrocement in strengthening corroded columns are examined under eccentric compression. Seven reinforced concrete columns were prepared. Five of them were subjected to accelerated corrosion. Three corroded column specimens were strengthened by AAS ferrocement jacket. Monotonic compression with small and large eccentricity was applied on the specimens to examine their mechanical performance and to assess strengthening effect. Based on experimental results, a mathematic model is proposed to predict loading capacity of columns with eccentricity.

7.2 Experiment and materials

7.2.1 Materials and specimens

Concrete based on the mix proportion used in Chapter 6 was employed to prepare the column specimens. High strength deformed bars with diameter of 12 mm (“T12”) and plain bars with diameter of 6 mm (“R6”) were used as the main reinforcements and stirrups, with measured yield strength of 550 MPa and 477 MPa, respectively.

Column specimens had height of 900 mm and a cross section of 200 mm × 200 mm. Corbels were assigned at both ends of specimens to transfer eccentric load. Concrete cover to main reinforcement was 38 mm. Reinforcements of specimen consisted of four T12 main reinforcements and six R6 stirrups with 150 mm spacing at mid-height and 100 mm spacing at the ends (Figure 7.1). 90° hooks were bent at both ends of the stirrups. The main reinforcements and stirrups were protected by epoxy at two ends of both corroded and strengthened specimens. Specimens were removed from formwork one day after casting, and were cured in water for 28 days. Compressive strength of concrete estimated using 100 mm cubes were 32.5 MPa and 33.6 MPa at 28 days and when the specimens were tested, respectively.

Seven specimens were prepared and divided into two groups according to loading types as follows: 1. Small eccentric compression with an eccentricity of 30 mm, and 2. large eccentric compression with an eccentricity of 130 mm. Each group included one control specimen (B1 or C1), one corroded specimen (B2 or C2), and one (B3) or two (C3 and C3a) strengthened specimens. Details of column specimens are given in Table 7.1.

Table 7.1 Details of specimens

ID of specimens	Details	Loading types
B1/B2/B3	Control / Corroded / Strengthened	Small eccentricity
C1/C2/C3 and C3a		Large eccentricity

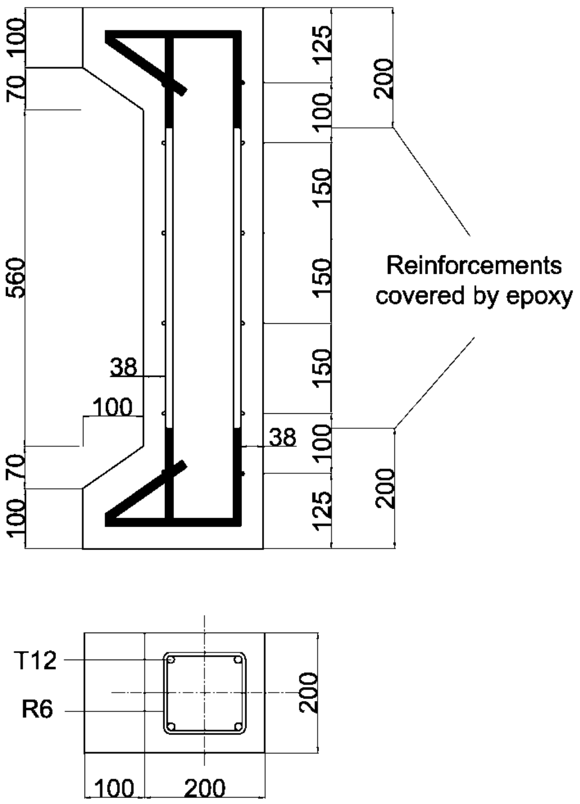

Figure 7.1 Schematic view of specimens (unit: mm)

After cured, specimens B2, B3, C2, C3 and C3a were subjected to artificially accelerated corrosion. The specimens were immersed in sodium chloride solution with concentration of 5%. Direct current of 0.68A was applied on reinforcements and kept for 21 days. Based on the magnitude of electric current and polarization time, corrosion-induced mass loss of main reinforcements and stirrups were 8.91% and 20.98% respectively, as shown in Chapter 6. As a result of accelerated corrosion, obvious longitudinal cracks and rust stain were observed on the surface of specimens (Figure 7.2).

Figure 7.2 Artificially corroded column specimen

Figure 7.3 Remove concrete cover

Figure 7.4 Wrap core concrete with two layers of SSWM

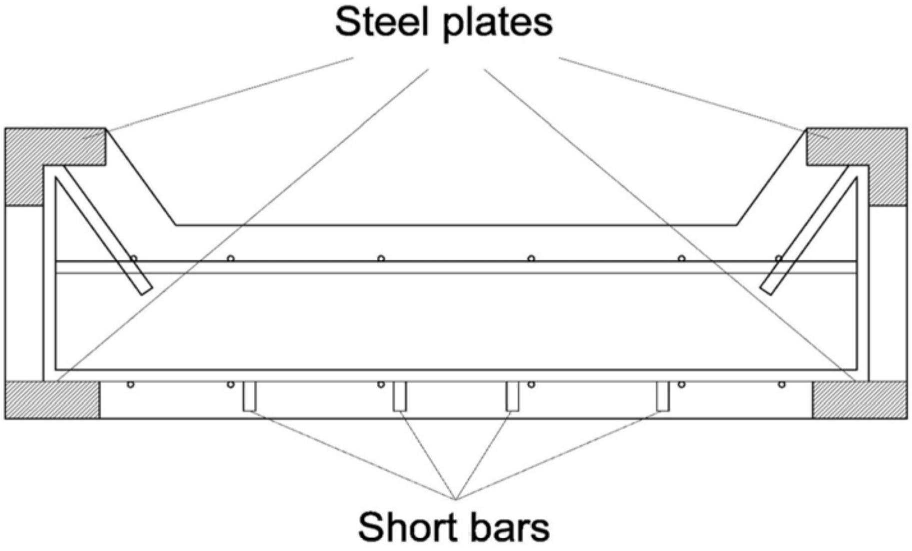

Figure 7.5 Schematic diagram to fix SSWM in specimen C3

Figure 7.6 Cast AAS mortar

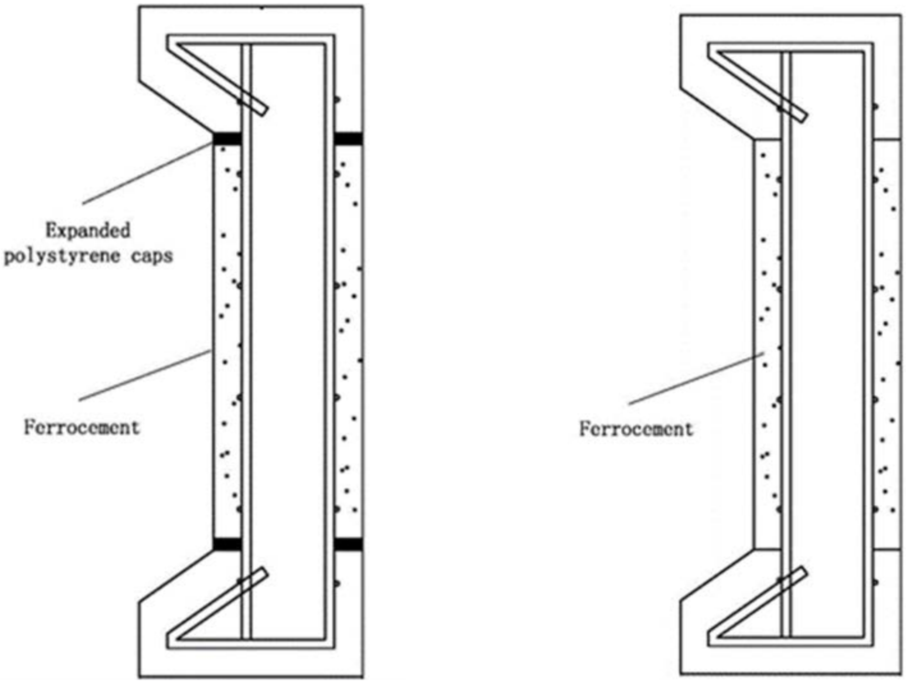

a. Specimens B3 and C3a b. Specimen C3

Figure 7.7 Schematic view of strengthened specimens

In Chapter 6 scheme S2 has demonstrated effectiveness in strengthening specimens with degree of corrosion of 8.9%. It was employed to strengthen specimens B3, C3 and C3a. Strengthening procedure consists of three steps as follows: 1. Remove concrete cover and the concrete contacting main reinforcements (Figure 7.3); 2. Clean the surface of concrete by compressed air; 3. Wrap core concrete with two layers of SSWM and overlap the SSWM at a length of 120mm (Figure 7.4). Four pairs of short bars were welded on main reinforcements at tensile side of specimen C3 to fix SSWM (Figure 7.5); and 4. Damp the core concrete and then place it into wooden formwork. Cast AAS mortar over the core concrete. The mortar was compacted using a vibrating table (Figure 7.6). The specimens retained their original size after strengthened. Specifically, foamed polystyrene caps were placed on both ends of specimens B3 and C3a to prevent ferrocement from direct loading (Figure 7.7).

7.2.2 Experimental setup

Strain gauges were installed on main reinforcements, stirrups and concrete surface at the mid-height of specimens. They were protected by waterproof adhesive and butyl tape from damage during concrete casting and accelerated corrosion. Five LVDTs were installed horizontally to measure lateral deflection of specimens. Locations of LVDTs and strain gauges are given in Figure 7.8.

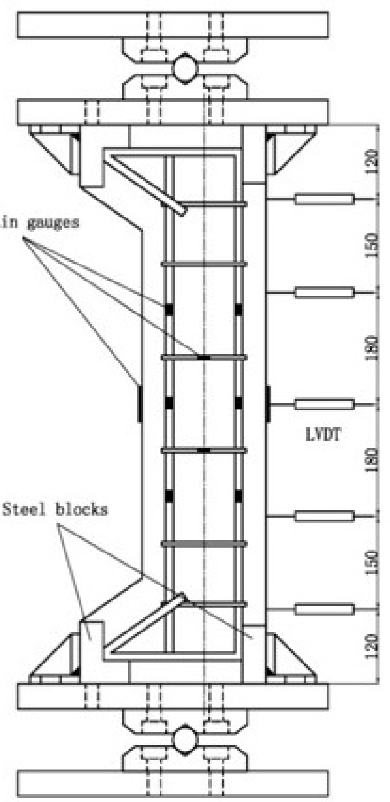

Figure 7.8 Locations of the LVDTs and strain gauges (unit: mm)

Both end surfaces of all specimens were capped. Preloading of 5 kN was applied to specimens. Monotonic compression was conducted through a universal testing machine by displacement control. Loading rate was 0.1 mm/min in pre-peak stage and 0.05 mm/min in post-peak stage for all specimens. Compressive test was terminated when the loading capacity declined by 15% from its peak.

7.3 Results and discussion

7.3.1 Failure modes

Figure 7.9 (a) shows failure mode of control specimen B1 under small eccentricity. In initial stage, cross section at mid-height of specimen suffered from uneven stress. Compressive stress of concrete was dramatically large at compressive side. With increasing loading, concrete reached its compressive capacity. Longitudinal cracks appeared and main reinforcements buckled. At the opposite side, transverse cracks appeared in concrete and main reinforcements remained elastic. Corroded specimen B2 displayed a similar failure mode but with degraded stiffness as compared with control specimen. Corrosion-induced longitudinal cracks rapidly developed under compression, which significantly damaged concrete cover of specimen. Corroded specimen lost its loading capacity owing to buckling of main reinforcements and compressive failure of concrete at the compressive side (Figure 7.9 (b)). Strengthened specimen B3 failed owing to tensile failure of ferrocement jacket. A longitudinal crack was formed in ferrocement jacket at the compressive side of column specimen, which is attributed larger transverse expansion of concrete (Figure 7.9 (c)).

Figure 7.10 shows the failure modes of specimens under large eccentricity. When compressive load reached 33 kN, the first crack appeared in concrete at tensile side of specimen. With increasing loading, transverse cracks were formed at the tensile side and strain of main reinforcements increased rapidly. When the specimen reached its loading capacity, main reinforcements yielded at the tensile side and concrete was crushed at the compressive side (Figure 7.10 (a)). Corroded specimen C2 showed failure mode similar to control specimen. Because of weak bonding between reinforcements and concrete caused by corrosion, spacing of cracks was larger in specimen C2 than that in specimen C1. As displacement increased, corrosion-induced longitudinal cracks widened and propagated, and concrete spalled at compressive side (Figure 7.10 (b)). Compared to specimen C2, specimen C3 responded with more transverse cracks at smaller spacing (Figure 7.11 (a)). SSWM provided resistance to loading at the tensile side and postponed spalling of mortar at the compressive side. Specimen C3 failed owing to tensile failure of ferrocement and yielding of main reinforcements at the tensile side, and compressive failure of ferrocement at the compressive side (Figure 7.11 (a), (b)). Strengthened specimen C3a failed due to corbel losing load transferring ability before the column reached its capacity (Figure 7.10 (d)).

a. Specimen B1 b. Specimen B2 c. Specimen B3

Figure 7.9 Failure modes of specimens under small eccentricity

a. Specimen C1 b. Specimen C2

c. Specimen C3 d. Specimen C3a

Figure 7.10 Failure modes of specimens under large eccentricity

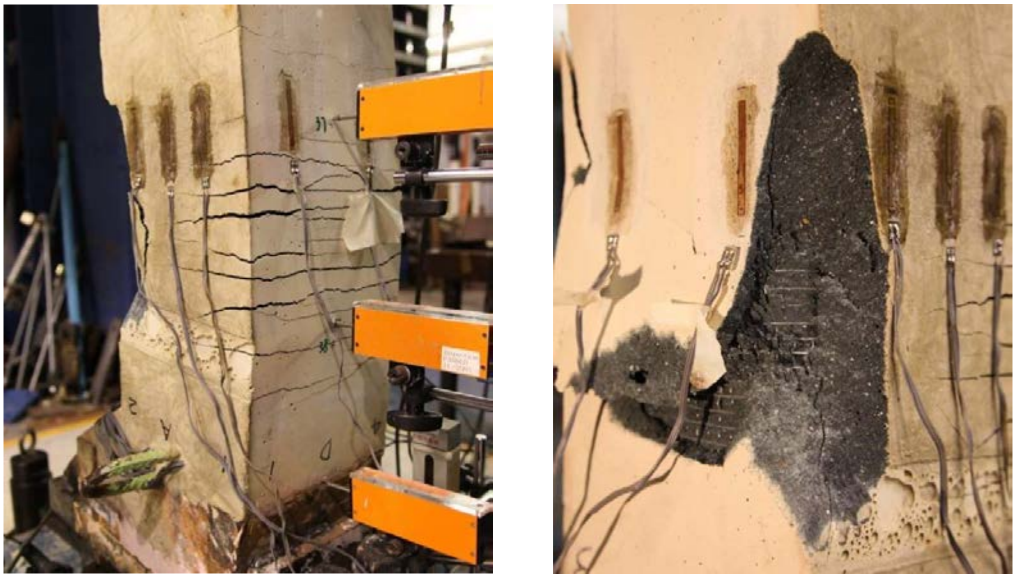

a. Tensile side b. Compressive side

Figure 7.11 Ferrocement jacket of Specimen C3

7.3.2 Load-deformation relationships

Moment-lateral deflection relationships at mid-height of specimens B1-B3 and C1-C3a are given in Figure 7.12 and Figure 7.13, respectively. Moment was estimated by multiplying the load by the eccentricity. Corroded specimens experienced substantial reduction in loading capacity. Peak loads of corroded specimens B2 and C2 decline by 30% and 21% as compared with control specimens B1 and C1, respectively Strengthened specimens displayed significant improvement in loading capacity and ultimate deformation. Peak load of specimen B3 was rehabilitated to a level close to that of control specimen B1. Specimen C3 showed remarkable larger moment capacity than control specimen C1. Strengthened specimens B3 and C3 exhibited better ductility in post-peak stage. Specimen C3a failed prematurely but exhibited loading capacity higher than specimen C2 by 17%. As specimen C3a did not display its full loading capacity, it will not be discussed further.

Corrosion of reinforcements also caused severe degradation in stiffness of specimens. When moment was less than 3 kNm, corroded specimen B2 had deflection close to control specimen B1. However, with increasing loading, lateral deflection of corroded specimen was rapidly increased. Corroded specimen C2 showed similar degradation in stiffness. Wu et al. (2010) indicated that deterioration in stiffness of corroded columns with eccentricity can be attributed to corrosion-induced longitudinal cracks in concrete, cross-sectional loss of main reinforcements and deteriorative bonding between concrete and reinforcements. The strengthening scheme effectively enhanced stiffness of corroded specimens. Strengthened specimens B3 and C3 achieved stiffness close to and higher than control specimens B1 and C1, respectively.

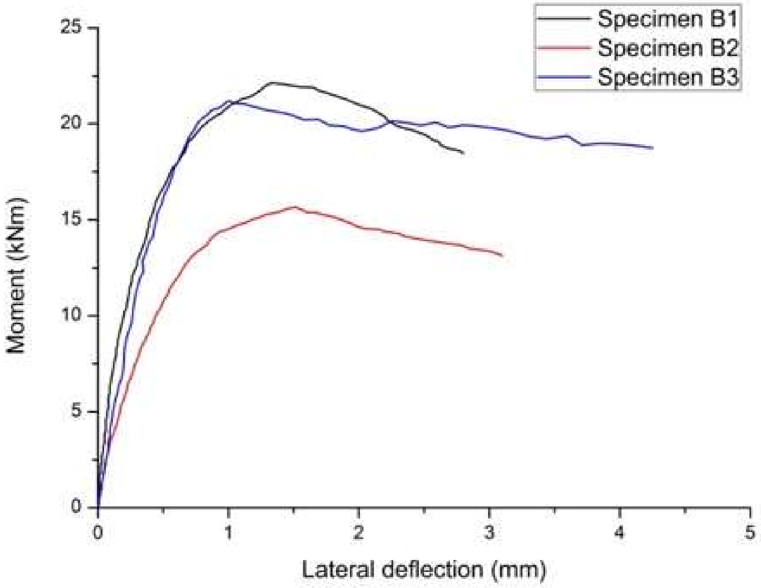

Figure 7.12 Moment-lateral deflection relationships at mid-height of specimens under small eccentricity

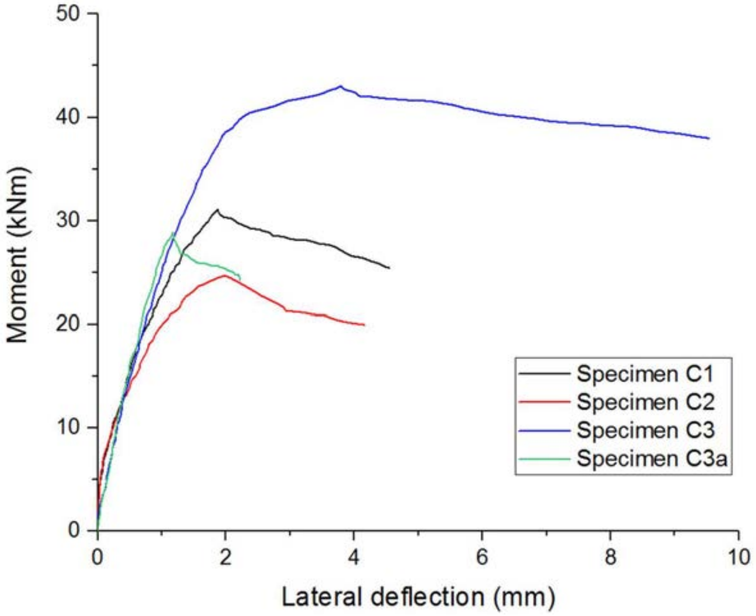

Figure 7.13 Moment-lateral deflection relationships at mid-height of specimens under large eccentricity

Strain of main reinforcements of specimens B1-B3 and C1-C3 are given in Figure 7.14 - Figure 7.15, respectively. When specimens B1-B3 reached peak load under small eccentricity, main reinforcements yielded at compressive side, while strain at tensile side was less than 0.0006. By contrast, main reinforcements yielded at tensile side in specimens C1-C3 under large eccentricity. As corrosion weakened stiffness of specimens and reduced cross-sectional area of reinforcements, it resulted in large strain of main reinforcements in corroded specimens B2 and C2. Compared to specimen B2, specimen B3 showed less strain of main reinforcements owing to confinement by ferrocement jacket. When subjected to large eccentricity, strengthened specimen C3 achieved remarkably lower strain of main reinforcements than corroded specimen C2, which is attributed to resistance of ferrocement jacket in both compressive and tensile side.

Strain of stirrups of specimens B1-B3 and C1-C3 are given in Figure 7.16 - Figure 7.17, respectively. Degree of corrosion of 21% seriously reduced cross-sectional area and led to large strain in stirrups of specimens B2 and C2. Benefited from confinement of ferrocement jackets, strain of stirrups was reduced in specimens B3 and C3. Strain of stirrups responding to peak moment ranged from 0.0008 to 0.0012 in specimens under small eccentricity, while was less than 0.00035 in specimens under large eccentricity. It is because area of compressive concrete is larger in specimens under small eccentricity, which results in higher expansive pressure to stirrups. Test results have indicated that stirrups are more effective in specimens under small eccentricity as compared with that of specimens under large eccentricity.

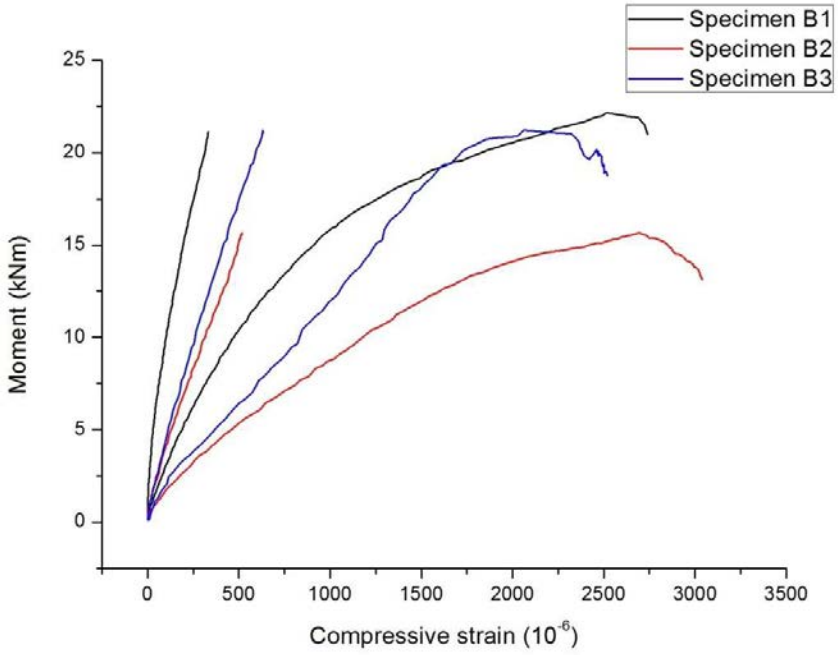

Figure 7.14 Strain of main reinforcements of specimens under small eccentricity

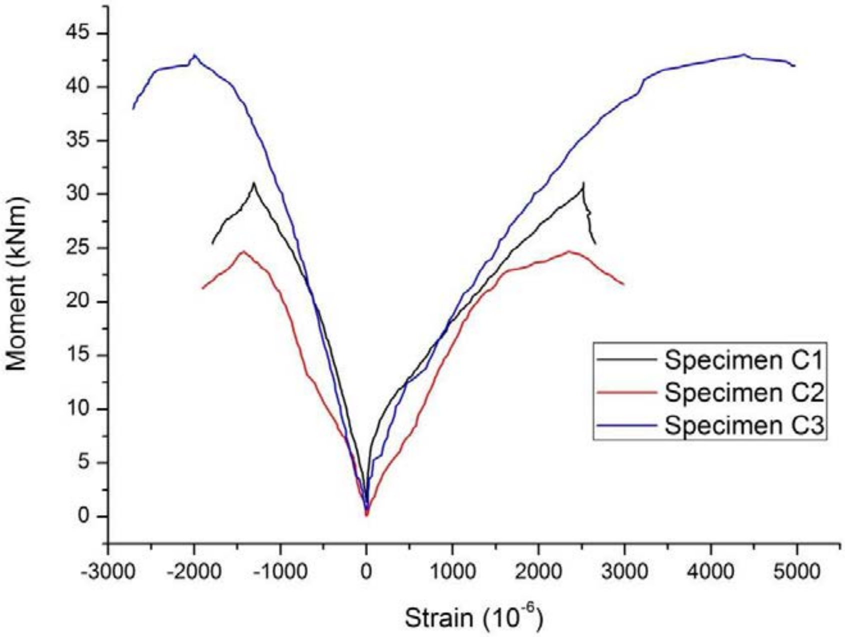

Figure 7.15 Strain of main reinforcements of specimens under large eccentricity

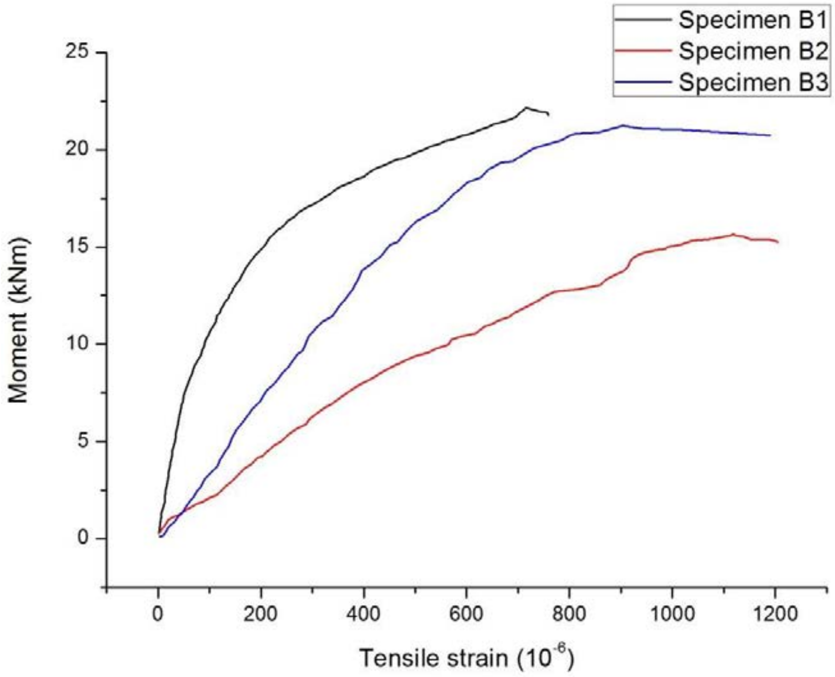

Figure 7.16 Strain of stirrups of specimens under small eccentricity

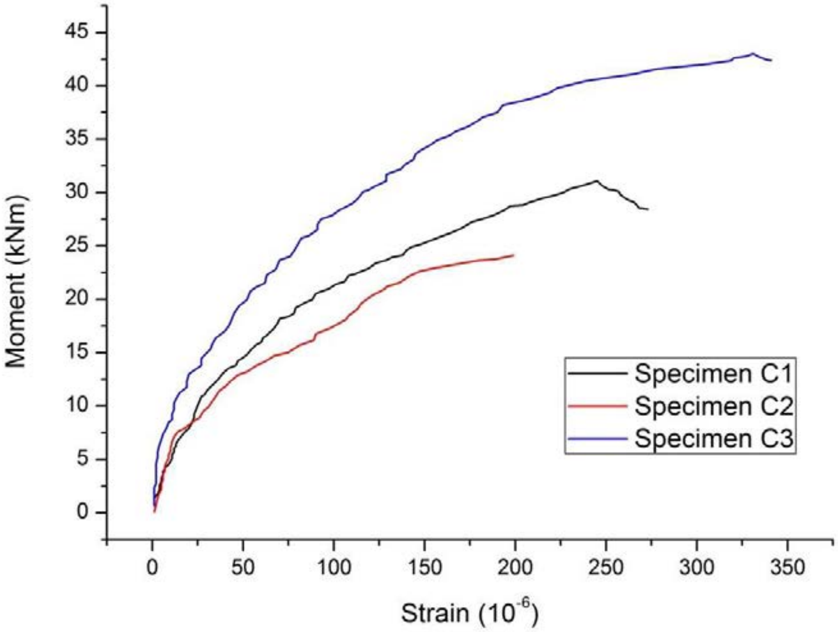

Figure 7.17 Strain of stirrups of specimens under large eccentricity

7.3.3 Loading capacity and ductility

Yield load “P_y”, peak load “P_p”, yield deformation “Δ_y”, ultimate deformation “Δ_u”, ductility, and ratios of peak load of the specimens to that of control specimen ($P_p/P_{p,con}$) are given in Table 7.2. Peak load is the maximum compressive force applied to specimens. Yield load and yield deformation are defined in Section 6.3. Ultimate deformation is defined as the deformation when the load declines to 85% of its peak. Deformation ductility is defined as the ratio of maximum deformation to yield deformation.

As shown in Table 7.2, corrosion of reinforcements caused significant deterioration in both yield load and peak load. Compared to control specimens B1 and C1, corroded specimens B2 and C2 suffer losses of 27% and 23% in yield load, and losses of 30% and 21% in peak load, respectively. Strengthened specimens B3 and C3 achieve 38% and 72% increase in peak load as compared with corroded specimens under small and large eccentricity, respectively. Loading capacities of strengthened specimen are comparable to or higher than those of control specimens. Moreover, ductility of enhanced by ferrocement jackets. Strengthened specimens B3 and C3 display ductility higher than that of corroded specimens by 44% and 79%, respectively. Ferrocement jackets demonstrate effectiveness in improvement of loading capacity and ductility of specimens under eccentricity.

Table 7.2 Loading capacity, deformation and ductility of specimens

Specimen	P_y (kN)	P_p (kN)	$P_p/P_{p,con}$	Δ_y (mm)	Δ_u (mm)	Ductility
B1	588.2	706.6	1.00	0.61	2.48	4.07
B2	429.0	497.0	0.70	0.73	2.66	3.64
B3	597.0	684.2	0.97	0.63	3.30	5.24
C1	207.9	235.7	1.00	1.36	3.89	2.86
C2	159.1	187.0	0.79	1.12	3.16	2.82
C3	284.3	321.6	1.36	1.89	9.53	5.04

7.4 Prediction of loading capacity of columns under small and large eccentricity

Loading capacity of columns under small eccentricity is related to section of confined core concrete (Figure 7.18). However, confinement of stirrups to core concrete is negligible when columns were loaded under large eccentricity (Figure 7.17). Load is thus deemed to be carried by the gross section regardless of confinement effect for the specimens under large eccentricity (Figure 7.19).

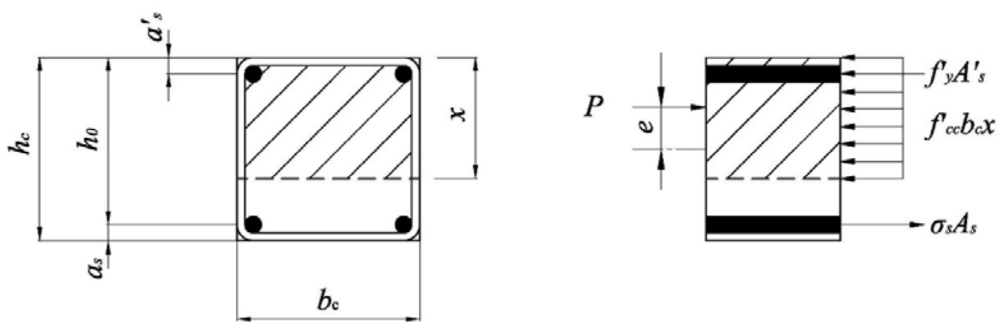

Figure 7.18 Prediction of loading capacity of a specimen under small eccentricity

Loading capacity of a specimen under small eccentricity can be predicted by the following equations:

$$\begin{cases} P = f_{\mathrm{y}}^{'} A_{\mathrm{s}}^{'} + f_{\mathrm{cc}}^{'} b_{\mathrm{c}} x - \sigma_{\mathrm{s}} A_{\mathrm{s}} \\ P\left(e + \dfrac{h_{\mathrm{c}}}{2} - a_{\mathrm{s}}\right) = f_{\mathrm{y}}^{'} \mathrm{A}_{\mathrm{s}}^{'} (h_0 - a_{\mathrm{s}}^{'}) + f_{\mathrm{cc}}^{'} b_{\mathrm{c}} x \left(h_0 - \dfrac{x}{2}\right) \\ \sigma_{\mathrm{s}} = E_{\mathrm{s}} \varepsilon_{\mathrm{cu}} \left(\dfrac{\beta_1 h_0}{x} - 1\right) \end{cases} \tag{7.2}$$

where $f_{\mathrm{y}}^{'}$ and $A_{\mathrm{s}}^{'}$ are yield strength and effective cross-sectional area of main reinforcements at compressive side; x is depth of the equivalent rectangular stress block; σ_{s} and A_{s} are stress and effective cross-sectional area of reinforcements at tensile side, respectively; e is eccentricity of load measured in test; h_0 is the effective depth, the distance from the extreme compression fiber to the centroid of tensile reinforcements; a_{s} and $a_{\mathrm{s}}^{'}$ are the distance from the centroid of reinforcements to the surface of concrete, respectively; $f_{\mathrm{cc}}^{'}$ is compressive strength of confined concrete, which can be obtained from equations (6.2) - (6.8). E_{s} is elastic modulus of steel; $\varepsilon_{\mathrm{cu}}$ is ultimate compressive strain of concrete; β_1 is the ratio of x to actual depth of compressive area.

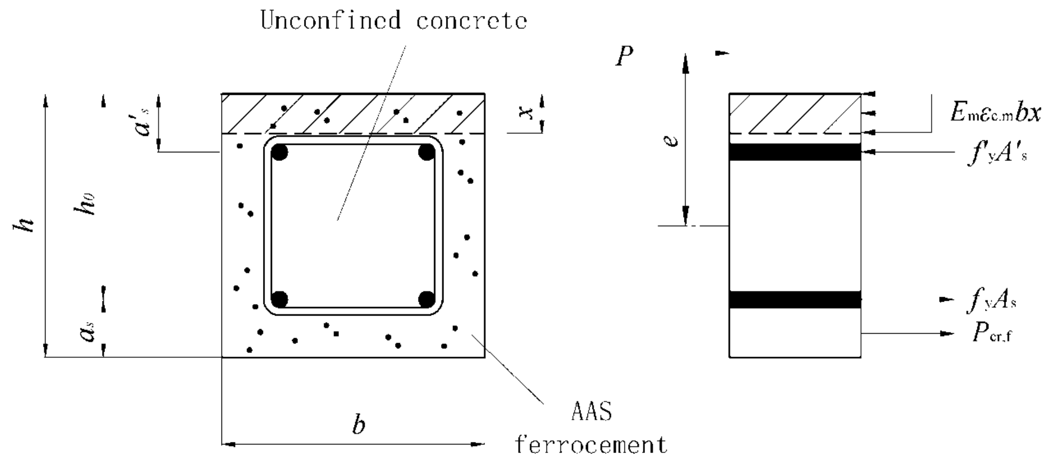

Figure 7.19 Prediction of loading capacity of a specimen under large eccentric compression

Loading capacity of control specimen, corroded specimen, and strengthened specimen under large eccentricity can be predicted by equations (7.3) - (7.5), respectively.

$$\begin{cases} P = f'_y A'_s + E_c \varepsilon_c b x - f_y A_s \\ P\left(e + \frac{h}{2} - a_s\right) = f'_y A'_s (h_0 - a'_s) + E_c \varepsilon_c x \left(h_0 - \frac{x}{2}\right) \end{cases} \tag{7.3}$$

$$\begin{cases} P = f'_y A'_s + f'_c b x - f_y A_s \\ P\left(e + \frac{h}{2} - a_s\right) = f'_y A'_s (h_0 - a'_s) + f'_c b x \left(h_0 - \frac{x}{2}\right) \end{cases} \tag{7.4}$$

$$\begin{cases} P = f'_y A'_s + E_m \varepsilon_{cm} b x - f_y A_s - P_f \\ P\left(e + \frac{h}{2} - a_s\right) = f'_y A'_s (h_0 - a'_s) + E_m \varepsilon_{cm} x \left(h_0 - \frac{x}{2}\right) + P_{cr,f}\left(a_s - \frac{t_m}{2}\right) \end{cases} \tag{7.5}$$

where f_y and f'_y are yield strength of main reinforcements at tensile side and compressive side, respectively; A_s and A'_s are effective cross-sectional area of main reinforcements at tensile side and compressive side, respectively; e is eccentricity of load measured in test; h_0 is effective depth, i.e. the distance from the extreme compression fiber to the centroid of tensile reinforcements; a_s and a'_s are the distance from the centroid of reinforcements to the surface of concrete, respectively; E_c and E_m are elastic modulus of concrete and AAS mortar; ε_c and ε_{cm} are measured strain of concrete and AAS mortar at compressive side, respectively. $P_{cr,f}$ is tensile capacity of ferrocement, which can be obtained by equation (5.4). t_m is thickness of ferrocement. For corroded specimen, contribution of concrete cover to loading capacity should be ignored as spalling was observed under compression.

Predictions of loading capacity of specimens are given in Table 7.3. Predicted results correlate well with the experimental results, with error less than 12%. Predicted loading capacity of control specimen B1 is lower than the experimental results. This is attributed to the resistance of intact concrete cover in specimen B1 to compressive loading.

Table 7.3 Prediction of loading capacity of specimens

Specimen	Prediction (kN)	Test values (kN)	Error
B1	621.7	706.6	-12.0%
B2	541.1	497.0	+8.9%
B3	650.3	684.2	-5.0%
C1	244.9	235.7	+3.9%
C2	199.6	187.0	+6.7%
C3	310.5	321.6	-3.5%

7.5 Summary

In this chapter, seven full-scale reinforced concrete columns were prepared and tested to failure under small and large eccentricity. Effect of corrosion of reinforcement on performance of specimens was investigated. AAS ferrocement was used to strengthen the corroded specimens. Based on the experimental results, the following summaries can be drawn:

1. Corrosion of reinforcement can severely weaken the loading capacity, stiffness, and ductility of reinforced concrete columns. A degree of corrosion of 8.9% on main reinforcements results in losses of 30% and 21% in loading capacity of columns under small and large eccentricity, respectively.

2. Columns strengthened by AAS ferrocement obtained rehabilitation of 38% and 72% in loading capacity, and 44% and 79% in ductility under small and large eccentricity,

respectively. The strengthening method recovered the loading capacity of corroded specimens to 97% or above the original level.

3. AAS ferrocement offers confinement to core concrete under small eccentricity, while directly resist the bending moment in columns under large eccentricity.

Empirical formulas were proposed to predict loading capacity of control, corroded and strengthened specimens. The predictions are in good agreement with the experimental results.

CHAPTER 8

CONCLUSIONS AND RECOMMENDATIONS

8.1 Conclusions

In this study, research was conducted to optimize mix proportion of AAS to strengthen corroded concrete columns. A complete factorial experiment was carried out to explore the effect of alkali content and modulus of sodium silicate on mechanical performance and chloride permeability of AAS. Mix proportion of AAS mortar was optimized based on comprehensive evaluation on strength, drying shrinkage, setting time and chloride resistance. Protection of optimal AAS with corrosion inhibitor on steel reinforcements was evaluated. Full-scale column specimens were subjected to accelerated corrosion and strengthened using varying strengthening schemes. Influence of corrosion of reinforcement on performance of specimens was investigated through axial compression, small eccentricity and large eccentricity. Effectiveness of four strengthening schemes for corroded columns was assessed. Based on the experimental results, the following conclusions can be drawn.

1. Alkali content of sodium silicate solution of AAS contributes to rapid setting and development of compressive strength with the adverse effect on large drying shrinkage, deterioration in flexural strength, and reduction on resistance to chloride penetration. Optimal alkali content is between 3% and 4% with flexural strength and compressive strength comparable to OPC.

2. Increasing moduli in sodium silicate solution of AAS accelerates setting, improves compressive strength and lowers chloride penetrability, but increases drying shrinkage and reduces flexural strength.

3. AAS can postpone formation of cracks induced by corrosion of reinforcements. $NaNO_2$ with dosage of 3% by mass of GGBFS exerts little negative effect on strength of AAS.

4. The optimized AAS for strengthening corroded members comprises GGBFS activated by sodium silicate solution with alkali content of 3%, modulus of 0.95 and $NaNO_2$ dosage of 3%.

5. SSWM strengthens AAS mortar more effectively than steel fibers, aramid fibers and GSWM. Stress of ferrocement at the first crack depends on tensile strength of both AAS mortar and SSWM, while peak load of ferrocement is only related to ultimate strength of SSWM.

6. Ferrocement jacket can improve peak load of plain concrete columns under axial compression. The improvement increases from 6% to 25% with increasing layers of SSWM in ferrocement jackets. Ferrocement jacket also sustains loading capacity in post-peak stage, increases peak deformation and increases ultimate deformation of column specimens.

7. Chloride causes severe pitting corrosion and weakens tensile performance of reinforcement. Corrosion-induced mass loss of stirrups is more than twice that of main reinforcements.

8. Corrosion of reinforcement severely reduces loading capacity, stiffness, and ductility of reinforced concrete columns. When degree of corrosion of main reinforcements is 8.9%, it leads to losses of 28%, 30% and 21% in loading capacity of columns under axial compression, small eccentricity and large eccentricity, respectively. Corroded specimens suffer reduction of 45% and 11% in ductility under axial compression and small eccentricity, respectively. When degree of corrosion is increased to 18.3%, axial compressive capacity of column specimen is declined by 46%.

9. All proposed strengthening schemes can effectively enhance peak load and ductility of corroded specimens. Loading capacities of strengthened specimens are comparable to or higher than control specimens under axial compression, small eccentricity and large eccentricity. Schemes S0N, S2, S2N and S4 achieve improvement from 36% to 63% in loading capacity with degree of corrosion of 18.3%. Specimen strengthened by scheme

S4 has 100% increase in ductility.

10. Specimens strengthened by ferrocement jackets perform better than applying new stirrups owing to higher and uniform confinement to core concrete. Ferrocement reinforced by SSWM is more suitable for strengthening chloride-contaminated structures. Strengthening schemes using ferrocement jackets with two and four layers of SSWM are therefore recommended to strengthen corroded columns with degree of corrosion of 10% and 20%, respectively.

In addition, analytical models are proposed to predict tensile strength of AAS ferrocement and confined compressive strength and corresponding strain of square concrete columns under compression. Predicted compressive strength of confined concrete is used to estimate loading capacity of strengthened specimens under axial compression, small eccentricity and large eccentricity, respectively. Prediction of peak load of specimens achieves good agreement with the test results.

8.2 Recommendations for further study

To further improve performance of AAS, the following research studies are recommended.

1. Owing to dehydration of silicate gels during hardening, AAS is prone to shrink when exposed to air. Shrinkage may cause tensile stress and micro cracks in the paste, which weakens tensile strength and resistance to chloride penetration. Shrinkage reducer may be used to diminish shrinkage of AAS.

2. Wrapping concrete members by SSWM is time-consuming. In this study, it took approximate half an hour to apply 1 m^2 of SSWM to wrap a column. As an alternative, AAS-based engineered cementitious composite (“ECC”) with excellent mechanical properties and workability can be applied. In ECC, fibers are added into mortar as reinforcements, which can dramatically improve efficiency of construction and achieve mechanical performance comparable to ferrocement. Further investigation is needed to

develop AAS-based ECC for strengthening corroded concrete structures.

REFERENCES

Abdullah, and Mansur, M. A. (2001). “Effect of mesh orientation on tensile response of ferrocement.” *Journal of Ferrocement*, 31(4), 289–298.

ACI 440.2R-02. (2002). “Guide for the design and construction of externally bonded FRP systems for strengthening concrete structures.” American Concrete Institute, Farmington Hills, Michigan.

ACI 549R-97. (1997). “State-of-the-art report on ferrocement.” American Concrete Institute, Farmington Hills, Michigan.

Ahn, W., and Reddy, D. V. (2001). “Galvanostatic testing for the durability of marine concrete under fatigue loading.” *Cement and Concrete Research*, 31(3), 343–349.

Al-Dulaijan, S. U., Al-Zahrani, M. M., Saricimen, H., Maslehuddin, M., Shameem, M., and Abbasi, T. A. (2002). “Effect of rebar cleanliness and repair materials on reinforcement corrosion and flexural strength of repaired concrete beams.” *Cement and Concrete Composites*, 24(1), 139–149.

Al-Otaibi, S. (2008) “Durability of concrete incorporating GGBS activated by water-glass”. *Construction and Building Materials*, 22(10), 2059-2067.

Al-Saidy, A. H., Al-Harthy, A. S., Al-Jabri, K. S., Abdul-Halim, M., and Al-Shidi, N. M. (2010). “Structural performance of corroded RC beams repaired with CFRP sheets.” *Composite Structures*, 92(8), 1931–1938.

Al-Sulaimani, G. J., Kaleemullah, M., Basunbul, I. A., and Rasheeduzzafar. (1990). “Influence of corrosion and cracking on bond behavior and strength of reinforced concrete members.” *ACI Structural Journal*, 87(2), 220–231.

Almusallam, A. A. (2001). “Effect of degree of corrosion on the properties of reinforcing steel bars.” *Construction and Building Materials*, 15(8), 361–368.

Almusallam, A. A., Al-Gahtani, A. S., and Aziz, A. R. (1996). “Effect of reinforcement corrosion on bond strength.” *Construction and Building Materials*, 10(2), 123–129.

Alonso, C., Andrade, C., Castellote, M., and Castro, P. (2000). “Chloride threshold values to depassivate reinforcing bars embedded in a standardized OPC mortar.” *Cement and Concrete Research*, 30(7), 1047–1055.

Alonso, C., Castellote, M., and Andrade, C. (2002). “Chloride threshold dependence of pitting potential of reinforcements.” *Electrochimica Acta*, 47(21), 3469–3481.

Altan, E., and Erdoğan, S. T. (2012). “Alkali activation of a slag at ambient and elevated temperatures.” *Cement and Concrete Composites*, 34(2), 131–139.

Amleh, L. (2000). “Bond deterioration of reinforcing steel in concrete due to corrosion.” *Repair, Rejuvenation and Enhancement of Concrete: Proceedings of the International Seminar*, University of Dundee, Scotland, UK, 5-6 September 2002.

Apostolopoulos, C. A., and Papadakis, V. G. (2008). “Consequences of steel corrosion on the ductility properties of reinforcement bar.” *Construction and Building Materials*, 22(12), 2316–2324.

Apple Daily. (2015). “The indonesian maid died from hitting by collapsed concrete canopy.” *http://hkm.appledaily.com/detail.php?guid=19079413&category_guid=4104&category=&issue=20150317*.

Apple Daily. (2016). “Spalling concrete in a subdivided unit hit a gire.” *http://hk.apple.nextmedia.com/news/art/20160109/19*.

Apple Daily. (2017). “A balcony of tenement building collapsed in Hung Hom.” *http://hk.apple.nextmedia.com/realtime/breaking/20170621/56855493*.

Araya-Letelier, G., Antico, F. C., Carrasco, M., Rojas, P., and García-Herrera, C. M. (2017). “Effectiveness of new natural fibers on damage-mechanical performance of mortar." *Construction and Building Materials*, 152, 672–682.

Arya, C., Buenfeld, N. R., and Newman, J. B. (1990). "Factors influencing chloride-binding in concrete." *Cement and Concrete Research*, 20(2), 291–300.

ASTM C1202-12. (2012). "Standard Test Method for Electrical Indication of Concrete's Ability to Resist Chloride Ion Penetration." American Society for Testing and Materials.

ASTM C595-17. (2017). "Standard Specification for Blended Hydraulic Cements." American Society for Testing and Materials.

ASTM C1148-92a. (2014). "Standard Test Method for Measuring the Drying Shrinkage of Masonry Mortar." American Society for Testing and Materials.

ASTM G1-03. (2003). "Standard Practice for Preparing, Cleaning, and Evaluating Corrosion Test Specimens. American Society for Testing and Materials.

Aydin, S. (2013). "A ternary optimisation of mineral additives of alkali activated cement mortars." *Construction and Building Materials*, 43, 131–138.

Bakharev, T., Sanjayan, J. G., and Cheng, Y. B. (1999). "Alkali activation of Australian slag cements." *Cement and Concrete Research*, 29(1), 113–120.

Batis, G., Routoulas, A., and Rakanta, E. (2003). "Effects of migrating inhibitors on corrosion of reinforcing steel covered with repair mortar." *Cement and Concrete Composites*, 25(1), 109–115.

Belal, M. F., Mohamed, H. M., and Morad, S. A. (2015). "Behavior of reinforced concrete columns strengthened by steel jacket." *HBRC Journal*, 11(2), 201–212.

Bencardino, F., and Condello, A. (2016). "Innovative solution to retrofit RC members: Inhibiting-Repairing-Strengthening (IRS)." *Construction and Building Materials*, 117, 171–181.

Ben Haha, M., Le Saout, G., Winnefeld, F., and Lothenbach, B. (2011). “Influence of activator type on hydration kinetics, hydrate assemblage and microstructural development of alkali activated blast-furnace slags.” *Cement and Concrete Research*, 41(3), 301–310.

Bernal, S., De Gutierrez, R., Delvasto, S., and Rodriguez, E. (2010). “Performance of an alkali-activated slag concrete reinforced with steel fibers.” *Construction and Building Materials*, 24(2), 208–214.

Bertolini, L., Elsener, B., Pedeferri, P., and Polder, R. (2004). “Corrosion of steel in concrete: prevention, diagnosis, repair. ” Wiley-VCH.

Bilim, C., and Ati, C. D. (2012). “Alkali activation of mortars containing different replacement levels of ground granulated blast furnace slag.” *Construction and Building Materials*, 28(1), 708–712.

Böhni, H. (2005). “Corrosion in reinforced concrete structures.” Woodhead Publishing Limited.

Broomfield, J. P. (2007). “Corrosion of steel in concrete.” Taylor and Francis.

BS EN 13892-2. (2002). “Methods of test for screed materials. Part 2: Determination of flexural and compressive strength.” British Standards Institute.

BS EN 196-3. (2005). “Methods of testing cement -— Part 3: determination of setting times and soundness.” British Standards Institute.

BS EN 206. (2013). “BSI Standards Publication Concrete — Specification , performance , production and conformity.” British Standards Institute.

Buenfeld, N. R., and Broomfield, J. P. (2000). “Influence of electrochemical chloride extraction on the bond between steel and concrete.” *Magazine of Concrete Research*, 52(2), 79–91.

Buildings Department. (2010). “Report on the inspection of buildings aged 50 or above.”

Buildings Department of Hong Kong Special Administrative Region.

Buildings Department. (2013). “Code of practice for structural use of concrete.” Buildings Department of Hong Kong Special Administrative Region.

Castellote, M., Andrade, C., and Alonso, C. (2002). “Accelerated simultaneous determination of the chloride depassivation threshold and of the non-stationary diffusion coefficient values.” *Corrosion Science*, 44(11), 2409–2424.

Castro, P. A., Vago, E. R., and Calvo, E. J. (1996). “Surface electrochemical transformations on spinel iron oxide electrodes in aqueous solutions.” *Journal of the Chemical Society, Faraday Transactions*, 92(18), 3371.

CCPA. (2017). “Annual report on industrial development of slag in 2016.” *Ccement*.

Chang, J. J. (2003). “A study on the setting characteristics of sodium silicate-activated slag pastes.” *Cement and Concrete Research*, 33(7), 1005–1011.

Chang, J. J., Yeih, W., and Hung, C. C. (2005). “Effects of gypsum and phosphoric acid on the properties of sodium silicate-based alkali-activated slag pastes.” *Cement and Concrete Composites*, 27(1), 85–91.

Chen, H., Jiang, F., Zhou, G., Xue, J., and Fu, J. (2011). “Experimental research on load-carrying capacity of corroded reinforced concrete columns strengthened with CFRP.” *Architecture Technology*, 42(12), 1134–1138.

Chen, Y., Zhang, P., Yang, M., and Leng, L. (2013). “Research on seismic performance of CFRP strengthening corroded reinforced concrete columns.” *China Civil Engineering Journal*, 46(2), 196–200.

Chi, M. (2012). “Effects of dosage of alkali-activated solution and curing conditions on the properties and durability of alkali-activated slag concrete.” *Construction and Building Materials*, 35, 240–245.

China Cement Research Institute. (2015). “Analysis on concrete industry in 2014 and prospect to 2015." *Guangdong Building Materials*, 4, 71–75.

Chung, L., Najm, H., and Balaguru, P. (2008). "Flexural behavior of concrete slabs with corroded bars." *Cement and Concrete Composites*, 30(3), 184–193.

Collins, F., and Sanjayan, J. . (2000). "Effect of pore size distribution on drying shrinking of alkali-activated slag concrete." *Cement and Concrete Research*, 30(9), 1401–1406.

Collins, F., and Sanjayan, J. G. (2001). "Microcracking and strength development of alkali activated slag concrete." *Cement and Concrete Composites*, 23(4–5), 345–352.

Collins, W. D., Weyers, R. E., and Al-Qadi, I. L. (1993). "Chemical treatment of corroding steel reinforcement after removal of chloride-contaminated concrete." *Corrosion*, 49(1), 74–88.

Dai, K., and Yuan, Y. (2005). "Experimental study on seismic performance of corroded exterior joints in RC frame." *Journal of China University of Mining & Technology*, 34(1), 51–56.

Deng, Z., Li, P., and Shi, Y. (2010). "Corrosion resistance and bond behavior research of corrosion-damaged reinforced concrete wrapped with CFRP." *Journal of Beijing University of Technology*, 36(10), 1357–1362.

Dhir, R. K., and Jones, M. R. (1999). "Development of chloride-resisting concrete using fly ash." *Fuel*, 78(2), 137–142.

Ding, W., and Cui, G. (2000). "Test and research of influences of reinforcing bar rust on the cracking of concrete protection layer and mechanics performances of reinforcing bar in concrete under the condition of atmosphere." *Concrete*, (1), 38–41.

Douglas, E., Bilodeau, A., and Malhotra, V. M. (1992). "Properties and Durability of

Alkali-Activated Slag Concrete", *ACI Materials Journal*, 89(5), 509-516.

Du, Y. G., Clark, L. A., and Chan, A. H. C. (2005). "Residual capacity of corroded reinforcing bars." *Magazine of Concrete Research*, 57(3), 135–147.

Duran Atiş, C., Bilim, C., Çelik, Ö., and Karahan, O. (2009). "Influence of activator on the strength and drying shrinkage of alkali-activated slag mortar." *Construction and Building Materials*, 23(1), 548–555.

Erdoğdu, S.¸, Bremner, T. W., and Kondratova, I. L. (2001). "Accelerated testing of plain and epoxy-coated reinforcement in simulated seawater and chloride solutions." *Cement and Concrete Research*, 31(6), 861–867.

Fan, W., and Wu, S. (1997). "Investigation of corrosion failure in reinforced concrete superstructure of the terminal of Beilun Port." *Proceeding of 8th Coastal Engineering Symposium and Development of Cross-Strait Port and Coast Symposium*, Xi'an.

Fang, C., Lundgren, K., Chen, L., and Zhu, C. (2004). "Corrosion influence on bond in reinforced concrete." *Cement and Concrete Research*, 34(11), 2159–2167.

Fernández-Jiménez, A., Palomo, J. G., and Puertas, F. (1999). "Alkali-activated slag mortars Mechanical strength behaviour A." *Cement and Concrete Research*, 29(8), 1313–1321.

Gan, W., Jin, W., and Gao, M. (2011). "Applicability study on accelerated corrosion methods of steel bars in concrete structure". *Journal of Building Structures*, 32(2), 41-47.

GB/T 18046-2008. (2008). "Ground granulated blast furnace slag used for cement and concrete." General Administration of Quality Supervision, Inspection and Quarantine of the People's Republic of China and Standardization Administration of the People's Republic of China.

Glass, G. K., and Buenfeld, N. R. (1997a). “Chloride threshold levels for corrosion induced deterioration of steel in concrete.” *RILEM International Workshop on Chloride Penetration into Concrete*, RILEM Publications SARL, 429–440.

Glass, G. K., and Buenfeld, N. R. (1997b). “The presentation of the chloride threshold level for corrosion of steel in concrete.” *Corrosion Science*, 39(5), 1001–1013.

Glukhovskij, V., Zaitsev, Y., and Pakhomov, V. (1983). “Slag-alkaline cements and concretes-structure, properties, technological and economical aspects of the use.” *Silicate Industries*, 10, 197–200.

Goto, S., and Roy, D. M. (1981). “The effect of w/c ratio and curing temperature on the permeability of hardened cement paste.” *Cement and Concrete Research*, 11(4), 575–579.

Haddad, R. H. (2016). “Hybrid repair configurations with CFRP composites for recovering structural performance of steel-corroded beams.” *Construction and Building Materials*, 124, 508–518.

Han, L. H., Zheng, Y. Q., and Teng, J. G. (2006). “Fire resistance of RC and FRP-confined RC columns.” *Magazine of Concrete Research*, 58(8), 533–546.

Hansson, C. M. (1984). “Comments on electrochemical measurements of the rate of corrosion of steel in concrete.” *Cement and Concrete Research*, 14(4), 574–584.

Hays, G. F. (2010). “World Corrosion Organization.” *http://events.nace.org/euro/corrodia/Fall_2010/wco.asp*.

He, J., Yang, C., and Kang, S. (2010). “Research progress on problem of retarding of alkali-activated slag cement.” *Bulletin of the Chinese Ceramic Society*, 29(5), 1093–1097.

Hong, N. (2005). “Development and use of steel bar inhibitor.” *Industrial Construction*, 35(6), 68–70.

Hui, Y., Li, R., Lin, Z., and Quan, M. (1997a). "Experimental studies on the property before and after corrosion of rebars in basic concrete members." *Industrial Construction*, 27(6), 14–18.

Hui, Y., Lin, Z., and Li, R. (1997b). "Experimental study and analysis on the property of corroded rebar." *Industrial Construction*, 27(6), 10–13.

Hussain, S. E., Rasheeduzzafar, Al-Musallam, A., and Al-Gahtani, A. S. (1995). "Factors affecting threshold chloride for reinforcement corrosion in concrete." *Cement and Concrete Research*, 25(7), 1543–1555.

Hwang, C. L., and Yoon, K. (1981). *Multiple attribute decision making: methods and applications: a state-of-the-art survey*. Springer-Verlag.

Jaegermann, C. (1990). "Effect of water-cement ratio and curing on chloride penetration into concrete exposed to mediterranean sea climate." *ACI Materials Journal*, 87(4), 333–339.

Jayasree, S., Ganesan, N., and Abraham, R. (2016). "Effect of ferrocement jacketing on the flexural behaviour of beams with corroded reinforcements." *Construction and Building Materials*, 121, 92–99.

Joshi, J., Arora, H. C., and Sharma, U. K. (2015). "Structural performance of differently confined and strengthened corroding reinforced concrete columns." *Construction and Building Materials*, 82, 287–295.

Justnes, H. (1997). "A Review of Chloride Binding in Cementitious Systems." *Nordic Concrete Research*, 21, 48–63.

Kaish, A. B. M. A., Alam, M. R., Jamil, M., Zain, M. F. M., and Wahed, M. A. (2012). "Improved ferrocement jacketing for restrengthening of square RC short column." *Construction and Building Materials*, Elsevier Ltd, 36, 228–237.

Kameswara Rao, C. B., and Kamasundara Rao, A. (1994). *Stress-strain relation for* *ferrocement in tension*.

Kashi, A., Ramezanianpour, A. A., and Moodi, F. (2017). “Durability evaluation of retrofitted corroded reinforced concrete columns with FRP sheets in marine environmental conditions.” *Construction and Building Materials*, 151, 520–533.

Kaushik, S. K., Singh, K. K., Kumar, R., and Sharma, T. P. (1996). “Performance of ferrocement encased concrete columns under fire exposure.” *Journal of ferrocement*, 26(3), 191–196.

Kawamura, M., Kayyali, O. A., and Haque, M. N. (1988). “Effects of a flyash on pore solution composition in calcium and sodium chloride-bearing mortars.” *Cement and Concrete Research*, 18(5), 763–773.

Kayyali, O. A., and Haque, M. N. (1995). “The Cl^- /OH^- ratio in chloride-contaminated concrete — a most important criterion.” *Magazine of Concrete Research*, 47(172), 235–242.

Ke, W. (2003). “Investigation report on corrosion in China. ” Science Press.

Kobayashi, K., and Rokugo, K. (2013). “Mechanical performance of corroded RC member repaired by HPFRCC patching.” *Construction and Building Materials*, 39, 139–147.

Kobayashi, K., and Shuttoh, K. (1991). “Oxygen diffusivity of various cementitious materials.” *Cement and Concrete Research*, 21(2–3), 273–284.

Kondraivendhan, B., and Pradhan, B. (2009). “Effect of ferrocement confinement on behavior of concrete.” *Construction and Building Materials*, 23(3), 1218–1222.

Krizan, D., and Zivanovic, B. (2002). “Effects of dosage and modulus of water glass on early hydration of alkali-slag cements.” *Cement and Concrete Research*, 32(8), 1181–1188.

Kukko, H., and Mannonen, R. (1982). “Chemical and mechanical properties of alkali-activated blast furnace slag (F-concrete).” *Nordic Concrete Research*, (1), 1–16.

Lam, L., and Teng, J. G. (2002). “Strength Models for Fiber-Reinforced Plastic-Confined Concrete.” *Journal of Structural Engineering*, 128(5), 612–623.

Lambert, P., Page, C. L., and Vassie, P. R. W. (1991). “Investigations of reinforcement corrosion. 2. Electrochemical monitoring of steel in chloride-contaminated concrete.” *Materials and Structures*, 24(5), 351–358.

Lan, Z., Zhang, Z., and Ding, D. (1991). “Experimental study of effectof cover thickness on crack width.” *Journal of Yunnan Polytechnic University*, (1), 1–8.

Lashiari, A. N. (1996). “Protection of reinforced concrete using corrosion inhibitors and coatings.” King Fahd University of Petroleum and Minerals.

Lee, H. S., Noguchi, T., and Tomosawa, F. (2002). “Evaluation of the bond properties between concrete and reinforcement as a function of the degree of reinforcement corrosion.” *Cement and Concrete Research*, 32(8), 1313–1318.

Li, F., Zhang, J., Hou, P., and Qu, F. (2013). “Experimental study on strengthening effect of bonded steel plate on corroded reinforced concrete beams.” *Concrete*, (6), 9–12.

Li, G., Yuan, Y., Du, J., Wang, Q., and Wang, H. (2004). “Strengthening and rehabilitation of a coalmine shaft tower damaged by the rebar’s corrosion.” *Building Structure*, 34(9), 18–20.

Li, J., Gong, J., and Wang, L. (2009). “Experimental study on seismic behavior of corroded reinforced concrete columns strengthened with concrete jacket and CFRP.” *China Civil Engineering Journal*, 42(4), 17–26.

Li, L., and Sagüés, A. A. (2001). “Chloride Corrosion Threshold of Reinforcing Steel in Alkaline Solutions—Open-Circuit Immersion Tests.” *Corrosion*, 57(1), 19–28.

Li, Q. C. (2001). "Initiation of chloride-induced reinforcement corrosion in concrete structural members - Experimentation." *ACI Structural Journal*, 98(4), 502–510.

Li, Q., Niu, D. T., and Liu, L. (2012). "The experimental study on reinforced concrete short-columns restrained by corroded stirrups." *Advanced Materials Research*, 446–449, 1376–1379.

Lide, D. R. (1999). "CRC Handbook of Chemistry and Physics". CRC Press, New York.

Lin, H., and Zhao, Y. (2016). "Effects of confinements on the bond strength between concrete and corroded steel bars." *Construction and Building Materials*, 118, 127–138.

Liu, C. (2014). "Roof collapses on Shenzhen residents seeking refuge during rainstorm." *https://thenanfang.com/roof-collapses-on-shenzhen-residents-seeking-refuge-during-rainstorm*.

Liu, F. (2009). "The durable reinforcement and comprehensive anti-corrosion technology of column in Changsha Gulf Bridge." *Journal of Guangdong Communications Polytechnic*, 8(1), 24–28.

Liu, Y., and Weyers, R. E. (1998). "Modeling the time-to-corrosion cracking in chloride contaminated reinforced concrete structures." *ACI Materials Journal*, 95(6), 675–680.

Locke, C., and Siman, A. (1980). "Electrochemistry of Reinforcing Steel in Salt-Contaminated Concrete." *Corrosion of Reinforcing Steel in Concrete*, ASTM International, 3–16.

Lu, Y., Zhu, X., and Qian, T. (2002). "Influence of electrochemical desalination on AAR of concrete." *Journal of Nanjing University of Technology*, 24(6), 35–39.

Ma, Y., Che, Y., and Gong, J. (2012). "Behavior of corrosion damaged circular reinforced concrete columns under cyclic loading." *Construction and Building Materials*, 29, 548–556.

Mainline Waterproofing Ltd. (2017). "Concrete 'spalling' remedial repairs." *http://www.mainlinewaterproofing.com.au/services/concrete-spalling-remedial-repairs*.

Mander, J. B., Priestley, M. J. N., and Park, R. (1988). "Theoretical Stress-Strain Model for Confined Concrete." *Journal of Structural Engineering*, 114(8), 1804–1826.

Manera, M., Vennesland, Ø., and Bertolini, L. (2008). "Chloride threshold for rebar corrosion in concrete with addition of silica fume." *Corrosion Science*, 50(2), 554–560.

Manning, D. G. (1996). "Corrosion performance of epoxy-coated reinforcing steel: North American experience." *Construction and Building Materials*, 10(5), 349–365.

Melo Neto, A. A., Cincotto, M. A., and Repette, W. (2008). "Drying and autogenous shrinkage of pastes and mortars with activated slag cement." *Cement and Concrete Research*, 38(4), 565–574.

Mietz, J., and Isecke, B. (1996). "Monitoring of concrete structures with respect to rebar corrosion." *Construction and Building Materials*, 10(5), 367–373.

Miranda, J. M., Cobo, A., Otero, E., and González, J. A. (2007). "Limitations and advantages of electrochemical chloride removal in corroded reinforced concrete structures." *Cement and Concrete Research*, 37(4), 596–603.

Miyauchi, K., Inoue, S., Kuroda, T., and Kobayashi, A. (1999). *Strengthening effects of concrete column with carbon fiber sheet. Transactions of the Japan Concrete Institute*.

Mohammed, T., and Hamada, H. (2001). "A discussion of the paper 'Chloride threshold values to depassivate reinforcing bars embedded in a standardized OPC mortar' by C. Alonso, C. Andrade, M. Castellote, and P. Castro." *Cement and Concrete Research*, 31(5), 835–838.

Montemor, M. F., Simões, A. M. P., and Ferreira, M. G. S. (1998). "Analytical Characterization of the Passive Film Formed on Steel in Solutions Simulating the Concrete Interstitial Electrolyte." *Corrosion*, 54(5), 347–353.

Morgan, D. R. (1996). "Compatibility of concrete repair materials and systems." *Construction and Building Materials*, 10(1), 57–67.

Mourad, S. M., and Shannag, M. J. (2012). "Repair and strengthening of reinforced concrete square columns using ferrocement jackets." *Cement and Concrete Composites*, 34(2), 288–294.

Mustea, A., and Manea, D. L. (2017). "Influence of Polypropylene Fibers upon the Mechanical Characteristics of Reinforced Composite Mortars." *Procedia Engineering*, 181, 338–345.

Naaman, A. E. (2000). *Ferrocement and laminated cementitious composites*. Techno Press 3000.

Otsuki, N., Miyazato, S., Diola, N. B., and Suzuki, H. (2000). "Influences of bending crack and water-cement ratio on chloride-induced corrosion of main reinforcing bars and stirrups." *ACI Materials Journal*, 97(4), 454–464.

Page, C. L., and Havdahl, J. (1985). "Electrochemical monitoring of corrosion of steel in microsilica cement pastes." *Materials and Structures*, 18(1), 41–47.

Page, C. L., Lambert, P., and Vassie, P. R. W. (1991). "Investigations of reinforcement corrosion. 1. The pore electrolyte phase in chloride-contaminated concrete." *Materials and Structures*, 24(4), 243–252.

Page, C. L., Short, N. R., and El Tarras, A. (1981). "Diffusion of chloride ions in hardened cement pastes." *Cement and Concrete Research*, 11(3), 395–406.

Page, C. L., and Vennesland, Ø. (1983). "Pore solution composition and chloride binding capacity of silica-fume cement pastes." *Materials and Structures*, 16(1), 19–25.

Palacios, M., and Puertas, F. (2005). "Effect of superplasticizer and shrinkage-reducing admixtures on alkali-activated slag pastes and mortars." *Cement and Concrete Research*, 35(7), 1358–1367.

Palsson, R., and Mirza, S. M. (2002). "Mechanical response of corroded steel reinforcement of abandoned concrete bridge." *ACI Structural Journal*, 99(2), 157–162.

Park, R., and Paulay, T. (1975). "Reinforced concrete structures." Wiley, New York.

Paulay, T., and Priestley, M. J. N. (1992). "Seismic design of reinforced concrete and masonry buildings." Wiley Interscience Publication.

Pavlík, V. (1994). "Corrosion of hardened cement paste by acetic and nitric acids part II: Formation and chemical composition of the corrosion products layer." *Cement and Concrete Research*, 24(8), 1495–1508.

Pedeferri, P. (1996). "Cathodic protection and cathodic prevention." *Construction and Building Materials*, 10(5), 391–402.

Peng, J., Li, J., Tang, H., and Zhang, J. (2015). "Experimental analysis of strengthening effect of corroded reinforced concrete beams stregnthened with bolted steel plates." *Journal of Civil, Architectural and Environmental Engineering*, 37(1), 88–95.

Pettersson, K. (1992). "Corrosion threshold value and corrosion rate in reinforced concrete." *CBI Report*, 2, 92.

Popov, B. N. (2015). "Pitting and Crevice Corrosion." *Corrosion Engineering*, 707-717.

Pu, X. (2010). “Alkali slag cement and concrete.” Science Press, Beijing.

Puertas, F., Palacios, M., Gil-Maroto, A., and Vázquez, T. (2009). “Alkali-aggregate behaviour of alkali-activated slag mortars: Effect of aggregate type.” *Cement and Concrete Composites*, Elsevier Ltd, 31(5), 277–284.

QuakeWrap. (2016). “Silos.” *http://www.quakewrap.com/silos.php*

Raphael J.M. (1984). “Tensile strength of concrete”. *Journal Proceedings*, 81(2), 158-165.

Rasheeduzzafar, Dakhil, F. H., and Al-Gahtani, A. S. (1985). “Corrosion of reinforcement in concrete structures in the Middle East.” *ACI Concrete International*, 7(9), 48–55.

Riversong, H. (2015). “From Rome to Portland - the story of concrete.” *https://riversonghousewright.wordpress.com/about/19-from-rome-to-portland-the-story-of-concrete*.

Roberge, P. R. (1999). “Handbook of corrosion engineering.” McGraw-Hill, New York.

Rodriguez, J., Ortega, L., and Casal, J. (1997). “Load carrying capacity of concrete structures with corroded reinforcement.” *Construction and Building Materials*, 11(4), 239–248.

Roy, D. M. (1999). “Alkali-activated cements: Opportunities and challenges.” *Cement and Concrete Research*, 29(2), 249–254.

Roy, D. M., Jiang, W., and Silsbee, M. R. (2000). “Chloride diffusion in ordinary, blended, and alkali-activated cement pastes and its relation to other properties.” *Cement and Concrete Research*, 30(12), 1879–1884.

Saatcioglu, M., and Razvi, S. R. (1992). “Strength and Ductility of Confined Concrete.” *Journal of Structural Engineering*, 118(6), 1590–1607.

Sahamitmongkol, R., Suwathanangkul, S., Phoothong, P., and Kato, Y. (2008). "Flexural behavior of corroded RC members with patch repair - experiments & simulation." *Journal of Advanced Concrete Technology*, 6(2), 317–336.

Sandberg, P. (1998). "Chloride initiated reinforcement corrosion in marine concrete." Lund University.

Schiessl, P., and Breit, W. (1996). "Local repair measures at concrete structures damaged by reinforcement corrosion - aspects of durability." *Proc. 4th Int. Symp. "Corrosion of Reinforcement in Concrete Construction,"* Cambridge, 525–534.

Shah, S. P., and Naaman, A. E. (1976). "Mechanical properties of glass and steel fiber reinforced mortar." *ACI Journal Proceedings*, 73(1), 50–53.

Shi, C. (1996). "Strength, pore structure and permeability of alkali-activated slag mortars." *Cement and Concrete Research*, 26(12), 1789–1799.

Shi, C. (2003). "Corrosion resistance of alkali-activated slag cement." *Advances in Cement Research*, 15(2), 77-81.

Shi, C., Day, R. L., Wu, X., and Tang, M. (1992). "Microstructure and performances of alkali-slag cement pastes." *Proceedings of the Ninth International Congress on the Chemistry of Cements*.

Shi, C. J., and Day, R. L. (1996). "Some factors affecting early hydration of alkali-slag cements." *Cement and Concrete Research*, 26(3), 439–447.

Shi, C., Krivenko, P. V., and Roy, D. (2006). "Alkali-activated cements and concretes." Taylor and Francis, Oxon.

Shi, C., and Qian, J. (2000). "High performance cementing materials from industrial slags - A review." *Resources, Conservation and Recycling*, 29(3), 195–207.

Shi, Q., Li, X., and Niu, D. (1999). "Tentative study on the bearing capacity of R.C. eccentric compressive members before and after reinfocement corrosion." *Journal* *of Xi'an University of Architecture and Technology*, 31(3), 218–221.

Shi, Q., Niu, D., and Yan, G. (2000). "Experimental research on hysteretic characteristics of corroded R. C. members with flexural and compressive axial loads under repeated horizontal loading." *Earthquake Engineering and Engineering Vibration*, 20(4), 44–50.

Söylev, T. A., and Richardson, M. G. (2008). "Corrosion inhibitors for steel in concrete: State-of-the-art report." *Construction and Building Materials*, 22(4), 609–622.

Strategic High Research Program. (1989). "Concrete and structures: progress and product update."

Sykes, J. M., and Balkwill, P. H. (1988). "Simulation the pitting corrosion of steel reinforcement in concrete." *The use of synthetic environments for corrosion testing,ASTM STP970*, 255–263.

Takiguchi, K., and Abdullah. (2001). "Shear strengthening of reinforced concrete columns using ferrocement jacket." *ACI Structural Journal*, 98(5), 696–704.

Tapan, M., and Aboutaha, R. S. (2011). "Effect of steel corrosion and loss of concrete cover on strength of deteriorated RC columns." *Construction and Building Materials*, 25(5), 2596–2603.

Tastani, S. P., and Pantazopoulou, S. J. (2004). "Experimental evaluation of FRP jackets in upgrading RC corroded columns with substandard detailing." *Engineering Structures*, 26(6), 817–829.

The Constructor. (2017). "Ferrocement in construction - application & advantages." *https://theconstructor.org/concrete/ferrocement-in*

Thomas, M. (1996). "Chloride thresholds in marine concrete." *Cement and Concrete Research*, 26(4), 513–519.

Trabanelli, G. (1987). "Corrosion inhibitors." *Corrosion Mechanism*, F. Mansfeld, ed., Marcel Dekker, New York, 119–163.

Triantafyllou, G. G., Rousakis, T. C., and Karabinis, A. I. (2017). "Corroded RC beams patch repaired and strengthened in flexure with fiber-reinforced polymer laminates." *Composites Part B: Engineering*, 112, 125–136.

Tuutti, K. (1982). "Corrosion of Steel in Concrete." Lund University.

Walliuidin, A. M., and Rafeeqi, S. F. A. (1994). "Study of behavior of plain concrete confined with ferrocement." *Journal of Ferrocement*, 24(2), 139–151.

Wang, B., Yuan, Y., Li, F., and Du, J. (2011). "Deterioration analysis of yield strength and its probabilistic model of steel bar corroded by chloride." *Journal of Building Materials*, 14(5), 597–603.

Wang, S. (1991). "Review of recent research on alkali-activated concrete in China." *Magazine of Concrete Research*, 43(154), 29–35.

Wang, S.-D., Pu, X.-C., Scrivener, K. L., and Pratt, P. L. (1995). "Alkali-activated slag cement and concrete: a review of properties and problems." *Advances in Cement Research*, 7(27), 93–102.

Wang, S.-D., Scrivener, K. L., and Pratt, P. L. (1994). "Factors affecting the strength of alkali-activated slag." *Cement and Concrete Research*, 24(6), 1033–1043.

Wang, S. D., and Scrivener, K. L. (1995). "Hydration products of alkali activated slag cements." *Cement and Concrete Research*, 25(3), 561–571.

Wang, X. G., Zhang, W. P., Gu, X. L., and Dai, H. C. (2013). "Determination of residual cross-sectional areas of corroded bars in reinforced concrete structures using easy-to-measure variables." *Construction and Building Materials*, 38, 846–853.

Wang, X. H., and Liang, F. Y. (2008). "Performance of RC columns with partial length corrosion." *Nuclear Engineering and Design*, 238(12), 3194–3202.

Wig, R. J., and Ferguson, L. R. (1917). “Reinforced concrete in sea water fails from corroded steel.” *Engineering News Record*, 79(15), 689–693.

Williamson, R. B., and Fisher, F. L. (1983). “Fire resistance of a load bearing ferrocement wall.” Berkeley.

Wong, W. Y. (2014). “Strengthening of Corroded Reinforced Concrete Columns by Alkali Activated Slag Mortar.” Final Year Report, The Hong Kong Polytechnic University.

Woodward, R. J., and Williams, F. W. (1988). “Collapse of YNS-Y-GWAS bridge, glamorgan.” *Proceedings of the Institution of Civil Engineers*, 84(4), 635–669.

Wu, Q., Yuan, Y., Zhu, J., and Wang, J. (2010). “Experimental study of the mechanical behavior of corroded reinforced concrete members.” *Journal of China University of Mining and Technology*, 39(6), 843-848.

Xu, S., and Niu, D. (2004). “The shear behavior of corroded simply supported reinforced concrete beam.” *Journal of Building Structures*, 25(5), 98–104.

Ye, H., Cartwright, C., Rajabipour, F., and Radli?ska, A. (2017). “Understanding the drying shrinkage performance of alkali-activated slag mortars.” *Cement and Concrete Composites*, 76, 13–24.

Yeomans, S. R. (1994). “Performance of black, galvanized, and epoxy-coated reinforcing steels in chloride-contaminated concrete.” *Corrosion*, 50(1), 72–81.

Yu, X., Jiang, L., Gao, H., Yu, X., and Zhang, X. (2015). “Deactivation and corrosion resistance of rebar in simulated pore solutions of alkali activated slag.” *Journal of Sichuan University (Engineering Science Edition)*, 47(5), 203–210.

Yuan, Y., Ji, Y., and Shah, S. P. (2007). “Comparison of two accelerated corrosion techniques for concrete structures.” *ACI Structural Journal*, 104(3), 344–347.

Yuan, Y., Jia, F., and Cai, Y. (2000). “Deterioration of mechanical behavior of corroded steel bar." *Industrial Construction*, 30(1), 43–46.

Zeng, Z., and Song, X. (2011). "Experimental investigation on static mechanical behavior of concrete beams with corroded reinforcement." *Journal of Huaqiao University (Natural Science)*, 32(1), 92–95.

Zhang, P., Lu, M., and Li, X. (1995). "The mechanical behaviour of corroded bar." *Journal of Industrial Buildings*, 25(257), 41–44.

Zhang, S., and Pan, Z. (2010). "Effect of chemical substances on setting time and strength development of alkali-activated slag cement." *Concrete*, (9), 68–73.

Zhang, W., Shang, D., and Gu, X. (2006). "Stress-Strain Relationship of Corroded Steel Bars." *Journal of Tongji University(Natural Science)*, 34(5), 586–592.

Zhang, W., Wang, X., and Gu, X. (2010). "Flexural behavior of corroded reinforced concrete beams strengthened with carbon fiber composite sheets." *China Civil Engineering Journal*, 43(6), 34–41.

Zhang, Y., and Chen, S. (2007). "Strengthening example for reinforced concrete derrick in a coal mine." *Building Structure*, 37(7), 90–92.

Zheng, W. Z., Chen, W. H., and Wang, Y. (2009). "High-temperature resistance performance of alkali-activated slag cementitious materials." *Journal of Huazhong University of Science and Technology (Nature Science Edition)*, 37(10), 96–99.

Zhu, Y., Zhu, X., and Luo, D. (2002). "Influences of electrochemical desalination on the behavior of reinforced concrete." *Port and Waterway Engineering*, 5, 8–12.

Živica, V. (2007). "Effects of type and dosage of alkaline activator and temperature on the properties of alkali-activated slag mixtures." *Construction and Building Materials*, 21(7), 1463–1469.